Copyright

by

Emily Jane Cooperdock

2017

The Dissertation Committee for Emily Jane Cooperdock certifies that this is the approved version of the following dissertation:

Novel (U-Th)/He thermochronometric constraints on serpentinized ultramafic rocks

Committee:

Daniel Stockli, Supervisor

Jaime Barnes

Richard Ketcham

Frieder Klein

Luc Lavier

Othmar Müntener

Novel (U-Th)/He thermochronometric constraints on serpentinized ultramafic rocks

by

Emily Jane Cooperdock

Dissertation

Presented to the Faculty of the Graduate School of

The University of Texas at Austin

in Partial Fulfillment

of the Requirements

for the Degree of

Doctor of Philosophy

The University of Texas at Austin

August 2017

Acknowledgements

First and foremost, I would like to give sincerest thanks to my PhD committee members. First to my advisor, Daniel Stockli, for conceiving of this "high-risk, high-reward" project and allowing me the freedom to explore its boundaries. I am very proud of what we accomplished together. Thanks for pushing me along when I felt doubt, and providing me the opportunity to explore the world in the process. Special thanks to Richard Ketcham and Jaime Barnes, as well. You both treated me in many ways as your own student, and for that I am grateful. Also, thanks to Rich for his natural skepticism, which kept me on my toes. And finally, thanks to Luc Lavier, Othmar Müntener, and Frieder Klein for expanding my scientific breadth and providing insightful and encouraging feedback throughout the years.

Funding for this project was achieved through a combination of grants and fellowships from the Jackson School of Geosciences, Geological Society of America, National Science Foundation and ExxonMobil. Many thanks to the ExxonMobil CEIBA group – Gianreto Manatschal, Pauline Chenin, Suzon Jammes, Garry Karner, Chris Johnson, and especially Suzanne Picazo who became a good friend and field partner.

This research would not have been possible without the aid of many experts in the many labs I frequented at the Jackson School. Enormous thanks to Jessie Maisano, Des Patterson, Lisa Stockli, Staci Loewy, Nate Miller and Donggao Zhao – many of whom also became good friends in the process. I have tremendous respect for you all.

My overall educational experience was enhanced by field trips, discussions and classes with Mark Cloos, Whitney Behr, Peter Kelemen and their students. I want to especially acknowledge (in no particular order) Spencer Seman, Edgardo Pujols, Mike

Prior, Adam Goldsmith, Nicole Hart, Steffi Wafforn, Margo Odlum, Tomas Capaldi, Dan Arnost, Romy Hanna, Miguel Cisneros, Ed Marshall, Michelle Gevedon, Natalie Raia, Rachel Bernard, Alissa Kotowski and Juan Carlos de Obeso for discussing science, giving advice, sharing samples and so much more.

I was lucky to enjoy a close relationship with great staff and administrators at the Jackson School. At the top of the list is the incredible Philip Guerrero, who has an astonishing and well deserved 100% approval rating from every graduate student in the program. Also thanks to Erin Negron, Teresita Gonzalez and Elsa Jimenez for their friendship and acquaintance over the years. It was a pleasure to work with you.

Finally, I extend a major thanks to my family. To my best friend for life, Sol Cooperdock. You have done too much to list, but one of the little unexpected experiences I enjoyed most was working out deceptively simple (yet complicated) math problems with you to make sure equations were properly balanced, units converted and results sound. Thanks to my mom, Joanne, for treating the PhD process as something normal, as if you always knew I could do it and would. Thanks for raising me to believe there are no boundaries on what I can achieve. Thanks to my dad and stepmom, Steve and Kerstin, for being phenomenal role models in the geoscience community and providing me with many opportunities. You both also instilled a no-boundaries mentality that helped me get here. Lastly, thanks to my in-laws and siblings, Connie, Peter, Sandra and Sydra, for their interest in spite of the (somewhat abstract) topic and unwavering support.

Novel (U-Th)/He thermochronometric constraints on serpentinized ultramafic rocks

Emily Jane Cooperdock, Ph.D.

The University of Texas at Austin, 2017

Supervisor: Daniel F. Stockli

Serpentinization, the hydration of peridotite, is a widespread process that impacts rheological properties along plate boundaries, fluid-mobile element cycling and biogeochemical processes. While numerous studies exist on the petrology, structure and geochemistry of serpentinites, geochronological analysis has been elusive due to the lack minerals with well-established dating techniques. With technological advances in radiogenic isotope analysis in the past decade, it is now possible to address the timing of serpentinization by dating the growth of magnetite that forms as a direct result of the breakdown of primary peridotite phases in the presence of water. This study develops and applies a (U-Th)/He-based method that is tailored to analyze magnetite that grow during the alteration of ultramafic rocks. The technique includes procedures to screen for grain quality in opaque phases with X-Ray Computed Tomography, physical air abrasion to remove the alpha implantation/ejection zone in the outer grain boundary, and analytical procedures to measure low parent nuclide concentrations typical of these lithologies. The method is then modified to test the applicability to date magmatic spinel, a primary mineral phase in peridotite, to date peridotite exhumation by tectonic and volcanic processes.

The magnetite (U-Th)/He technique is applied to serpentinites within an exhumed subduction complex in Syros, Greece, uplifted serpentinites within the Malenco Ultramafic

Unit, Italian Alps, and to carbonated serpentinite in Wadi Fins, Oman. The results of these studies provide evidence for episodic or continuous magnetite growth over millions of years, which implies that magnetite formation can continue to occur in serpentinites under changing metamorphic conditions. These studies also show that multiple generations of magnetite growth can be distinguished based on magnetite grain size and trace element chemistry, and that hydrothermal magnetite can record changing chemical conditions and act as an important host phase of U and Th in serpentinites. Overall, the magnetite (U-Th)/He chronometer can be used to distinguish between multiple episodes of fluid-rock alteration, which has implications for the cooling history and geochemical exchanges in serpentinized peridotite. This technique, coupled with spinel (U-Th)/He, has broad applicability to investigate the timescales of mantle exhumation and alteration of ultramafic rocks in a variety of tectonic settings.

Table of Contents

List of Tables

List of Figures

Chapter 1: Unraveling alteration histories in serpentinites and associated ultramafic rocks with magnetite (U-Th)/He geochronology[1]

Abstract

Serpentinization is a widespread process that impacts large-scale geodynamic processes along plate boundaries including continental breakup, seafloor spreading, and subduction. Documenting the timing of serpentinization is critical for our understanding of these processes, but direct dating of serpentinites has been challenging or impossible. We present the first application of magnetite (U-Th)/He chronometry to date stages of alteration and cooling in ultramafic rocks. In order to demonstrate the viability of magnetite He dating in these lithologies, magnetite ages were obtained from two ultramafic lithologies of the Kampos mélange belt, a high-pressure low-temperature (HPLT) subduction complex on the island of Syros, Greece. Magnetite (U-Th)/He measurements of internal fragments from large grains within a chlorite schist and a serpentinite record Mid-Miocene exhumation-related cooling ages, whereas smaller grains from the serpentinite record mineral growth associated with hydrothermal fluid-flow along Pliocene normal faults. These age results, in addition to magnetite trace element geochemistry, reveal evidence for multiple episodes of fluid-rock alteration, which has implications for the cooling history and local geochemical exchanges of this HPLT terrane. This method provides a new tool that may be expanded to investigate the processes and timescales of serpentinization from a variety of tectonic settings.

[1] Cooperdock, Emily HG, and Daniel F. Stockli. "Unraveling alteration histories in serpentinites and associated ultramafic rocks with magnetite (U-Th)/He geochronology." *Geology* 44.11 (2016): 967-970. I am the first author.

Introduction

Serpentinization, the hydration of peridotite, has a profound effect on fundamental geological processes such as deformation of the lithosphere, geochemical cycling, and the evolution of early life (Escartin et al., 2001; Kodolanyi et al., 2012; Sleep et al., 2011). Though numerous studies have investigated the petrology (e.g., Coleman, 1971; Evans, 2008), structure (e.g., Auzende et al., 2014) and geochemistry (e.g., Deschamps et al., 2013) of serpentinites, the absolute chronology of serpentinization remains elusive due to a lack of common accessory minerals that can be dated using established techniques. Only in rare cases have absolute ages for serpentinites been obtained, e.g., via hydrothermal zircons in blackwall zones (Dubinska et al., 2004). The majority of temporal constraints on serpentinization are inferred from cross-cutting intrusions (Jagoutz et al., 2007) or overlying sediments (Bill et al., 2001). The ability to determine the timing of serpentinization and the age of serpentinites is critical to decipher progressive hydration events and the time-scales of elemental recycling in tectonic and geochemical processes.

This study presents a novel approach to constrain the timing of cooling of exhumed ultramafic rocks and the low-temperature fluid alteration of serpentinites by dating magnetite. Magnetite occurs as a common secondary mineral in serpentinites from the fluid-induced breakdown of Fe-bearing peridotite minerals (Bach et al., 2006; Burkhard, 1993). Magnetite appears to form either directly from the interaction of olivine and water to produce serpentine and magnetite (Evans, 2008) or during secondary reactions that extract Fe from early formed Fe-rich serpentine and brucite (Bach et al., 2006; Schwarzenbach et al., 2016). While debated, magnetite growth likely does not occur until $> 30\%$ of the peridotite is serpentinized and is maximized at $> 70\%$ serpentinization and at temperatures between 200-300°C (Klein et al., 2014; Oufi et al., 2002). Modal abundances of magnetite vary in seafloor serpentinites from $<<$ 1 wt.% up to 6 wt.%, and generally

decrease in antigorite-bearing subducted serpentinites at eclogite-facies conditions (Debret et al., 2014; Evans, 2010).

Blackburn et al. (2007) demonstrated the viability of magnetite (U-Th)/He (MgHe) to measure eruption ages in mafic to intermediate volcanic rocks. Very low parent nuclide concentrations (ppb-level) in ultramafic magnetite commonly require combining multiple grains or fragments for robust analytical precision. He implantation from matrix U and Th require removal of the grain's outer 20 μm, effectively limiting usable grain size to ≥ 60 μm for MgHe dating. MgHe has a nominal He closure temperature (T_c) of 250 ± 40°C, assuming a 10°C/my cooling rate based on step-heating diffusion experiments using 500 μm internal grain fragments from kimberlitic magnetite. Given these published He diffusion kinetics and the size range of datable magnetite in ultramafic rocks, the nominal closure temperature may vary from 215°C for 60 μm to 280°C for 2 mm grain sizes.

Thus, provided sufficiently large grains are available, this technique has the potential to date magnetite forming reactions in low-temperature serpentinization environments, or the cooling age of magnetite that formed, or were re-heated, at high temperatures- a distinction that the temperature sensitivity of serpentine polymorphs may help clarify (Evans, 2010). To demonstrate the feasibility of this technique we apply it to ultramafic lithologies from the Kampos mélange zone, an exhumed HPLT subduction complex on the Cycladic island of Syros, Greece. Kampos has widely been used to study chemical and mineralogical processes that occur during subduction near the slab-mantle interface (e.g., Breeding et al., 2004). However, in order to properly interpret measured geochemical trends it is critical to understand the timing of alteration event(s) and mineral growth. This study uses magnetite trace element geochemistry to distinguish between multiple episodes of magnetite growth in ultramafic rocks, and MgHe dating to determine the timing of alteration and cooling events in serpentinites.

Geologic background and sample description

For this study, magnetite was analyzed from ultramafic lithologies in the Kampos belt, a mélange zone composed of subducted Cretaceous oceanic crustal blocks encased in a serpentinized ultramafic matrix (Bröcker and Enders, 2001; Seck et al., 1996) (Fig. 1). Localized metasomatism with modeled temperatures of 400-430°C resulted in chlorite-rich blackwall alteration zones between ultramafic and mafic lithologies (Marschall et al., 2006). Euhedral magnetite grains were collected from two distinct matrix lithologies: a chlorite schist and a talc-rich, sheared serpentinite (Fig. 1.1). The chlorite schist represents a sample of blackwall-altered mélange matrix containing large (mm) euhedral magnetite, whereas the serpentinite sample comes from a shear zone and is characterized by a range in magnetite grain sizes (μm-mm) in association with sheared talc (Fig 2.1).

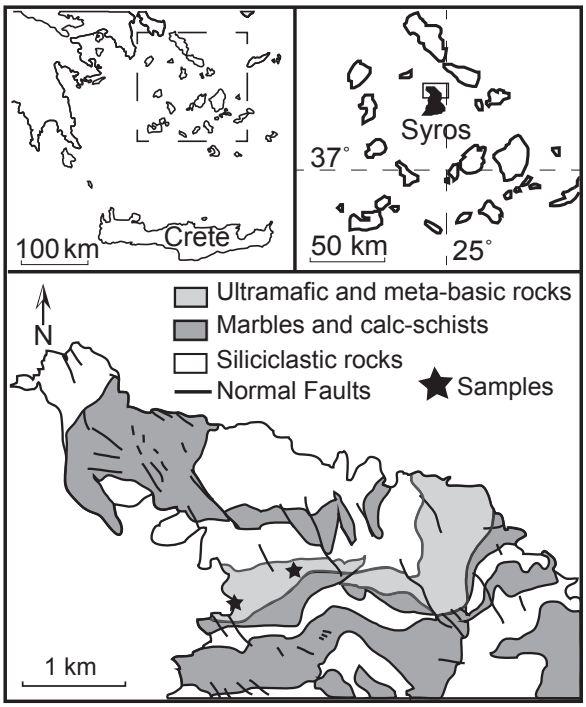

Figure 1.1: Simplified geologic map of northern Syros with sample locations marked. Sample locations are ~1 km apart: chlorite schist (37.493528°"N, 24.909838°"E); serpentinite (37.490192°N, 24.901703°"E). Modified from Keiter et al., (2004).

The thermal history of the island of Syros, Greece is well-constrained through multiple chronometers. The lithologies on the island experienced blueschist to eclogite facies metamorphism with peak conditions of 450-500°C and 15-16 kbar in the Eocene constrained by garnet Lu-Hf (~52 Ma) (Lagos et al., 2007; Ridley, 1984), followed by subduction channel exhumation in the Oligo-Miocene constrained by $^{40}Ar/^{39}Ar$ cooling ages (~40-20 Ma) (Bröcker et al., 2013; Maluski et al., 1987), and back-arc extension constrained by zircon (U-Th)/He and apatite fission track ages (~10-8 Ma) (Ring et al., 2003; Soukis and Stockli, 2013). Late-stage, NW-trending brittle normal faults postdate Miocene detachment faulting and are thought to be active since ~5 Ma (Gautier et al., 1999).

Magnetite preparation and (U-Th)/He measurement

Whole rock samples were crushed and magnetite crystals were separated from the crushed separate by hand magnet. Individual magnetite grains were picked based on size and morphology using an optical microscope. Single, euhedral magnetite grains greater than one millimeter were selected from the chlorite schist and crushed with mortar and pestle. Internal fragments without clear crystal faces were selected for CT-scanning. Since grain sizes ranged from hundreds of micrometers to over one millimeter in the serpentinite, two grain treatments were employed. Magnetite grains over a millimeter were crushed with mortar and pestle and internal fragments with no clear crystal faces were selected for CT-scanning. Magnetite grains between ~300-600 μm were hand-picked based on euhedral morphology. These sub-mm grains were physically air abraded by placing 20-40 similarly sized grains into an air abrasion vessel at once and abrading at 6 psi for about 4 hours following the procedure reported in Blackburn et al., (2007). The abrasion conditions

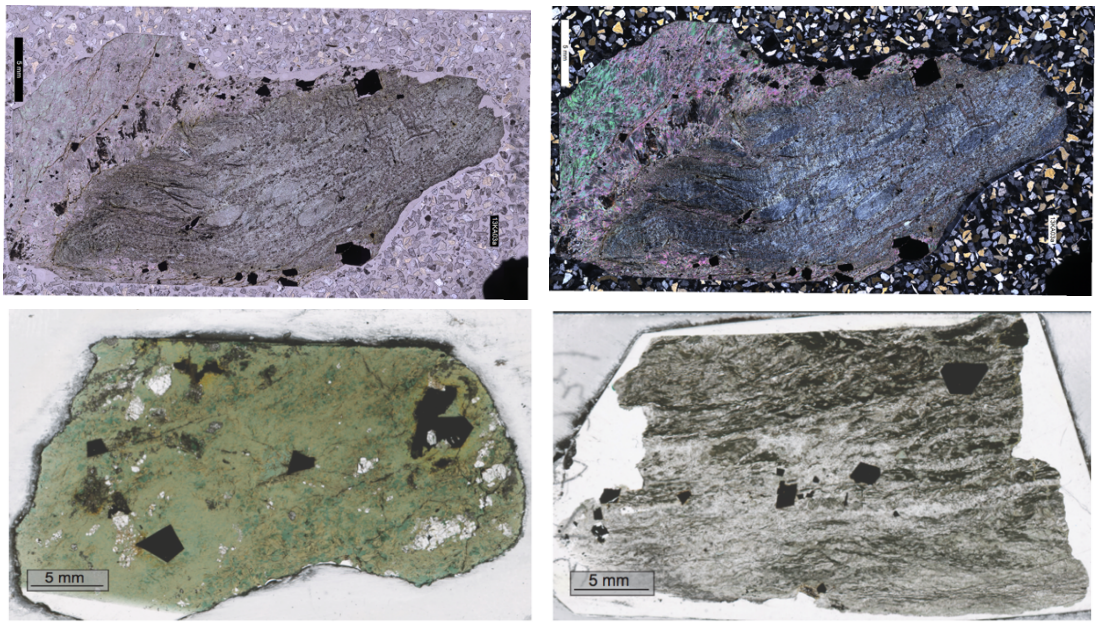

Figure 1.2: Photomicrographs of serpentinite and chlorite schist thin sections. Clockwise from top left: First three thin sections are of the serpentinite; bottom left is chlorite schist. Top left: Plane polarized light through talc-rich section of serpentinite. General mineralogy: serpentine, talc, magnetite and minor chlorite; Top right: Cross-polarized light; Bottom right: scanned thin section of serpentinite in less talc-rich section; Bottom left: Chlorite schist thin section. Large magnetite grains are euhedral. The other opaque mineral is ilmenite. General mineralogy: chlorite, epidote, rutile, ilmenite, magnetite, apatite and < 6 μm zircon.

employed in this study are based on previous experiments that calibrated the pressure and time to effectively remove ~ 20 μm from the outside of magnetite.

Internal fragments and abraded grains were scanned using the X-Radia Micro-CT scanner at the University of Texas High-Resolution Computed Tomography Facility (UTCT). In order to fit within the 5 mm^3 scanning volume, 10-50 grains or internal fragments were scanned in a single run at ~ 6 μm resolution. The X-Ray CT data were used to screen grains and fragments for attached matrix material (serpentine or chlorite), and

inclusions, which are otherwise impossible to see on a 3D scale in opaque minerals (Fig. 1.3).

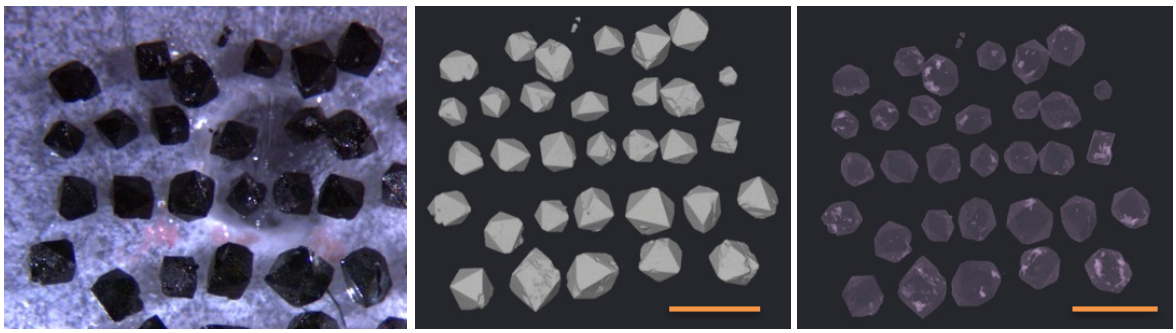

Figure 1.3: Syros magnetite CT Data: Left: Optical microscope photograph of unabraded magnetite grains mounted on double-sided sticky tape in preparation for CT scanning. Middle: 3-D isosurface rendering of magnetite grains constructed using the X-Ray CT data and Avizo software. Right: Volume rendering of magnetite grains with inclusions that have a different density from the magnetite. Inclusions are highlighted in bright pink. The grains with these inclusions were avoided for analysis. Scale bar is 1 mm.

Individual aliquots were constructed using 2-7 internal fragments (from a single large crystal when possible), or abraded grains of similar size. The fragments or abraded grains that were clear of inclusions were wrapped into platinum tubes and laser heated with a Photonmachine Diode Laser at a pre-specified pyrometer temperature for 10 min. ^{4}He amounts were measured on a Blazers Prisma QMS-200 quadrupole mass spectrometer (QMS) by "spiking" with a ^{3}He internal isotopic reference standard. Gas was purified in a Janis cryogenic trap, and a SAES NP10 getter before entering the QMS. Aliquots were reheated until the He yield became ≤ 2x blank values measured after each unknown. Final ^{4}He amounts were calculated using a calibration against a manometrically-determined ^{4}He standard. Gas blanks were measured between each aliquot to determine the background and drift during the run. Final gas amounts are all blank corrected corresponding to the blank following gas extraction of an unknown.

Samples were dissolved for U, Th, and Sm measurement using a two-step HF-HNO_3 and HCl hot plate dissolution procedure. After aliquots were unpacked from platinum tubes into Savillex beakers, a ^{238}U,^{230}Th, and ^{149}Sm spike in 5% HNO_3 was added. A 5:1 concentrated HF - 7N HNO_3 mixture was added to the beakers, which were tightly sealed and heated at ~180°C overnight. Samples were dried down to a small bead and 200 μl of concentrated HCl was added to the beaker, which was tightly sealed and heated overnight at 180°C. After chloride conversion, the solution was dried down to a small bead and 100 μl of 7N HNO_3, followed by 500 μl of MilliQ H_2O were added in preparation for analysis on the Thermo Element 2 HR-ICP-MS. Final U-Th-Sm concentrations were calculated using isotope dilution with a mixed spike calibrated against a gravimetric 1 ppb U-Th-Sm standard solution.

Magnetite trace element measurements

Trace elements (Mg, Al, Ti, V) were measured on magnetite grains from three 60 μm-thick thin sections of the serpentinite (Fig. 1.2). Laser spot analyses were measured on all visible magnetite grains of sufficient size from each thin section as either transects across the grain (7 grains on one thin section of the serpentinite) or as random points (16 grains on two thin sections of the serpentinite). Measurements were made on a single collector ThermoFisher Element II HR-ICP-MS with an attached Photonmachines Analyte G2 193 nm ArF excimer laser ablation system. The laser settings included a 70% laser energy, 6.35 J/cm^2 fluence, and 6 mJ energy. Spot sizes of 65 μm were employed, and all spots were pre-ablated. GSD, the primary standard, was run between every four unknowns, and GSC was run between every 12 unknowns as the secondary standard. Analyses for each element in GSD (n = 29) and GSC (n=11) are reproducible within < 5% over the

experiment, with the exception of V (25%) in GSC. Concentrations were calculated using Fe as an internal standard on Igor Pro Iolite software.

Results

Chlorite schist magnetite aliquots (n=7) constructed with internal fragments from ≥ 2 mm grains yield ages from 13-21 Ma with a mean age of 16.0 ± 3.3 Ma (1σ) (Fig. 1.4). Three aliquots that yielded ages > 30 Ma are not included in the mean age. While larger grains have a higher effective T_c and can result in older ages, we consider it unlikely in this sample as the analyzed grains were similarly sized. Instead, the cause is likely analytical, resulting from insufficient removal of parentless He implanted into the analyzed fragments, or incomplete dissolution of high U, Th or Sm inclusions not detected by CT scanning, (such as < 6 μm zircon, which are present in the sample).

In the serpentinite sample MgHe ages vary by grain size. Internal fragments from a ≥ 2 mm grain (n=3) yield ages that range between ~7–15 Ma, whereas multi-grain aliquots (n=9) composed of 300-600 μm grains yield reproducible ages with a mean age of 3.1 ± 0.7 Ma (1σ) (Fig. 1.4). Elemental analyses of serpentinite magnetite grains by LA-ICP-MS on thin sections show positive trends in grain size and concentrations of Mg, Al, Ti, and V (Fig. 1.5) with ≥ 2 mm grains exhibiting significantly higher concentrations of

Table 1.1 Syros magnetite (U-Th)/He age data

Aliquot name	Age (Ma)	U (ppb)	Th (ppb)	Sm (ppb)	^{4}He (nmol/g)	Th/U	Mass (µg)	# of grains or fragments
Serpentinite								
Multi-grain aliquots of individually abraded grains (300-600 µm)								
mg13KA03-1	3.3 ± 0.1	4	247	11	0.0011	56	736	3
mg13KA03-5	3.4 ± 0.1	5	488	32	0.0022	90	516	3
mg13KA03-7	2.9 ± 0.5	5	18	2	0.0001	3	946	3
mg13KA03-8	4.3 ± 0.4	3	50	3	0.0004	15	824	4
mg13KA03ab-1	2.7 ± 0.3	6	156	12	0.0006	27	825	4
mg13KA03ab-4	1.8 ± 0.7	8	17	4	0.0001	2	948	3
mg13KA03ab-7	2.4 ± 0.2	7	65	10	0.0003	9	1114	3
mg13KA03ab-11	3.6 ± 1.6	3	9	4	0.0001	3	960	2
mg13KA03ab-14	3.3 ± 0.6	6	54	7	0.0003	9	724	7
Internal fragments from single large grain (≥ mm)								
mg13KA03ab-28	8.8 ± 0.8	3	32	12	0.0005	11	2377	4
mg13KA03ab-29	15.3 ± 1.8	2	7	2	0.0003	3	1078	4
mg13KA03ab-30	6.8 ± 1.2	11	39	17	0.0007	4	2487	7
Chlorite schist								
Internal fragments from large grains (≥ mm)								
mg07SY09-1	13.0 ± 1.8	6	6	698	0.0010	0.9	315	4
mg07SY09-3	21.0 ± 1.1	26	15	1045	0.0043	0.6	826	3
mg07SY09-8	13.2 ± 0.5	27	53	1425	0.0037	2	576	3
mg07SY09-11	20.1 ± 0.7	21	16	174	0.0028	0.8	1452	3
mg07SY09-14	16.0 ± 0.2	43	217	3480	0.0106	5	705	3
mg07SY09-17	13.5 ± 0.1	84	412	6186	0.0170	5	582	3
mg07SY09-21	15.5 ± 0.6	5	15	828	0.0013	3	894	2
mg07SY09-20	43.7 ± 0.5	27	13	1479	0.0099	0.5	223	3
mg07SY09-22	45.0 ± 0.5	13	12	592	0.0051	0.9	2205	7
mg07SY09-23	30.5 ± 0.9	3	6	144	0.0009	2	1302	2

***Mass* refers to the mass of the aliquot, not individual grains. *# of grains or fragments* refers to the number combined into a single aliquot.**

Table 1.2: LA-ICP-MS spot analyses on magnetite grains from the serpentinite sample

Grain #	Grain size (µm)	# of spots	Mg (ppm)	SD*	Ti (ppm)	SD*	V (ppm)	SD*	Al (ppm)	SD*
Random Spot Analysis										
1	523	2	455	52	78	1	427	59	23	3
2	597	2	470	4	84	3	475	1	24	1
3	726	2	512	87	86	3	537	1	27	5
4	313	1	436	19	73	4	388	17	19	2
5	296	1	345	16	83	4	324	14	17	2
6	504	2	416	16	69	7	438	49	17	2
7	1039	3	575	53	183	89	543	36	35	7
8	506	1	466	68	55	1	420	5	18	1
9	768	2	490	18	54	.4	358	47	20	2
10	4202	11	755	123	178	91	591	56	60	16
11	606	2	652	136	72	5	453	55	27	1
12	949	3	643	98	190	58	582	32	37	6
13	1218	4	806	221	123	56	549	71	43	22
14	5734	11	736	199	172	81	597	59	64	18
15	619	2	551	30	85	7	497	28	27	4
16	681	3	523	44	89	18	492	41	23	5

Table 1.3: LA-ICP-MS magnetite grain transects

Grain-Spot #	Grain size (μm)	Mg (ppm)	SD*	Ti (ppm)	SD*	V (ppm)	SD*
Grain Transect Analysis							
1-1	1858	333	18	59	8	315	14
1-2		635	51	180	42	505	25
1-3		497	29	131	6	607	30
1-4		862	45	267	43	671	37
1-5		1063	52	167	19	715	34
1-6		644	26	153	24	647	23
1-7		612	61	80	11	535	36
2-1	487	365	17	52	5	309	8
2-1		589	26	48	4	384	12
3-1	1518	536	64	65	7	359	24
3-2		461	19	67	4	442	14
3-3		483	22	101	11	528	17
3-4		446	20	132	19	580	15
3-5		472	19	153	31	620	17
3-6		644	29	180	42	652	20
3-7		875	32	140	13	688	21
3-8		991	31	124	9	703	20
3-9		1339	57	122	8	707	22
3-10		1030	43	157	20	719	25
3-11		960	34	137	11	687	24
3-12		904	40	132	11	673	24
3-13		743	35	143	15	620	22
3-14		529	22	107	12	568	18
4-1	5500	679	57	197	47	641	20
4-2		554	26	110	16	663	24
4-3		752	25	114	6	70	21
4-4		1053	39	139	12	717	30
4-5		1125	40	150	21	747	26
4-6		1118	51	137	19	764	32
4-7		1151	47	107	8	773	31
4-8		1191	50	188	73	794	36
4-9		1136	34	234	78	780	23
4-10		1132	35	117	9	768	22
4-11		1092	28	236	82	749	12
4-12		961	39	140	13	735	21
4-13		956	28	298	67	716	22
4-14		869	32	188	85	723	21
4-15		904	39	179	49	715	29
4-16		829	48	116	8	700	36
4-17		658	35	140	17	645	32
4-18		1260	120	71	6	401	23
5-1	2021	432	20	73	8	473	22
5-2		573	32	152	49	557	26
5-3		484	26	118	8	610	24

Table 1.3 (continued)

Grain-Spot #	Grain size (μm)	Mg (ppm)	SD*	Ti (ppm)	SD*	V (ppm)	SD*
Grain Transect Analysis							
5-4		520	24	117	7	622	25
5-5		599	29	138	16	638	28
5-6		950	260	100	9	608	39
5-7		707	37	116	9	639	28
5-8		665	27	106	9	634	30
5-9		585	28	198	54	646	30
5-10		689	25	115	8	627	26
5-11		609	33	625	40	549	27
5-12		475	22	91	7	495	22
6-1	796	480	24	79	5	539	23
6-2		985	38	305	27	635	24
6-3		1075	38	148	10	682	22
6-4		1006	34	672	38	663	21
6-5		604	27	129	8	549	19
7-1	2003	452	24	80	6	471	21
7-2		599	30	364	83	595	30
7-3		690	29	130	10	620	29
7-4		807	37	290	150	653	24
7-5		698	25	223	24	639	21
7-6		616	30	163	14	648	26
7-7		521	28	223	73	594	29
7-8		427	25	104	6	554	23

*** Reported SD errors are the standard deviation of averaged laser spot analyses. If n=1, reported errors are standard error on the individual analyses.**

these elements than grains ≤ 600 μm. LA-ICP-MS transects across 7 large grains (> 700 μm) reveal distinct, though variable, chemical zoning in Mg, Ti and V (Al not measured) with depleted rim concentrations similar to the measured ≤ 600 μm grains (Fig. 1.6).

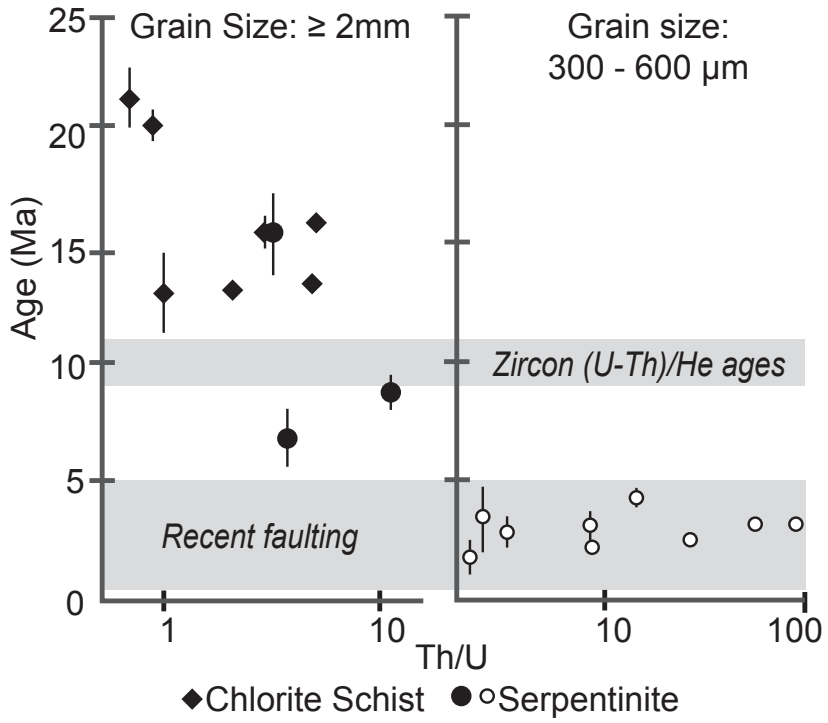

Figure 1.4: Syros magnetite (U-Th)/He age results plotted against Th/U. Propagated analytical error shown with vertical error bars. The left column shows results for internal fragments from large grains (≥ 2 mm) sourced from the chlorite schist and serpentinite. The right column shows ages for 300-600 μm grains, found exclusively in the serpentinite (open circles). Zircon (U-Th)/He ages constrain the timing of Miocene extension and cooling below 180°C (upper grey box) (Soukis and Stockli, 2013). Recent faulting (lower grey box) constrained by field relationships (Keiter et al., 2004).

Age interpretations and implications

Mineralogical and textural relationships show that magnetite formed in the chlorite schist during blackwall alteration, which occurred at elevated temperatures of 400-430°C

(Marschall et al., 2009; Miller et al., 2009). The lack of evidence for overprinting by low-temperature alteration in this rock, and the uniformity of magnetite grain size, support the notion of a single magnetite growth episode. Given that magnetite growth occurred at temperatures well in excess of the nominal magnetite He T_c, we interpret these as ~16 Ma MgHe cooling ages (Fig. 1.4). This interpretation is supported by lower temperature chronometers (apatite FT and zircon (U-Th)/He) that indicate cooling below 200°C since ~10 Ma (Ring et al., 2003; Soukis and Stockli, 2013).

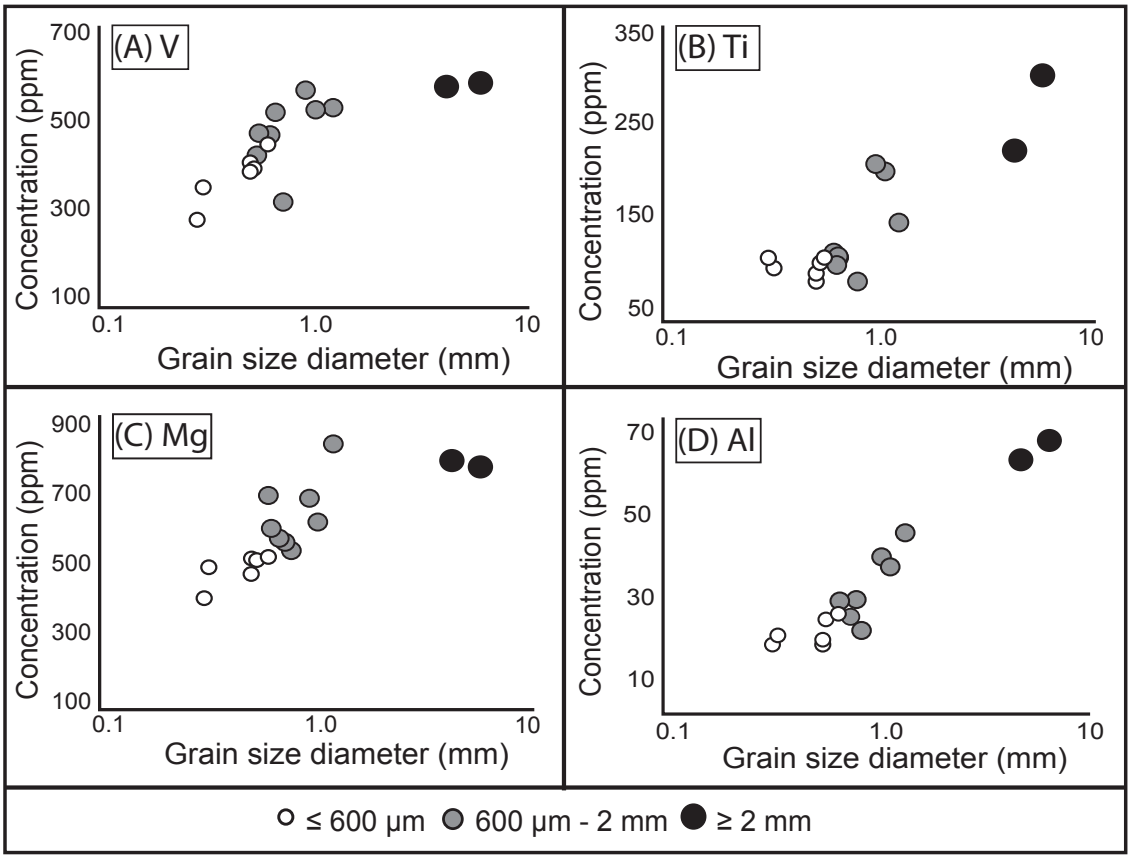

Figure 1.5: Magnetite trace element chemistry determined by LA-ICP-MS on thin sections from the serpentinite sample. (A-D): Al, Mg, V, and Ti concentrations in ppm plotted against grain size. Symbols represent the average of multiple laser spots (n =1 to 11) on a single grain (largest grain is 5.5 mm).

In contrast to the chlorite schist, the serpentinite contains two magnetite populations distinguishable by grain size, chemistry and age. Trace element concentrations of magnetite measured on thin sections reveal evidence for two magnetite growth events. Large magnetite (≥ mm) have higher concentrations of Mg, Al, Ti and V, consistent with these grains forming when such elements were mobilized, likely during the blackwall-related fluid alteration event recorded in the chlorite schist magnetite (Fig. 1.5). Despite these elements being relatively fluid-immobile, the steep concentration gradients between juxtaposed mafic and ultramafic lithologies during blackwall reactions promote elemental redistribution of Mg, Al, Ti and V (Miller et al., 2009; von Strandmann et al., 2015), which can be partitioned into hydrothermally formed magnetite (Nadoll et al., 2014).

Grain transects, however, reveal that the rims of large magnetite grains (> 700 μm) do not show the same blackwall-related elemental enrichment, and suggest secondary magnetite overgrowth. This overgrowth is chemically similar to the measured compositions of the ≤ 600 μm magnetite grains, which also do not show blackwall-related trace element signatures. Hence, both the overgrowth and the smaller size magnetite are likely the result of a secondary, younger magnetite formation event that post-dates blackwall alteration (Fig. 1.7).

MgHe ages on individual grains and internal fragments from the serpentinite confirm episodic magnetite growth revealed by the chemical and textural analyses. Magnetite trace elements in large grains support an initial magnetite growth event during blackwall alteration at > 400°C, which implies some grains grew above the MgHe T_c (Fig. 1.7). Internal fragments from a mm-sized grain in the serpentinite, however, show significant age dispersion (15-7 Ma) between the timing of cooling of magnetite in the chlorite schist at ~16 Ma and small magnetite formation at ~3 Ma, suggesting that these

aliquots represent a mixture of older cores and younger overgrowth zones, resulting in mixed ages.

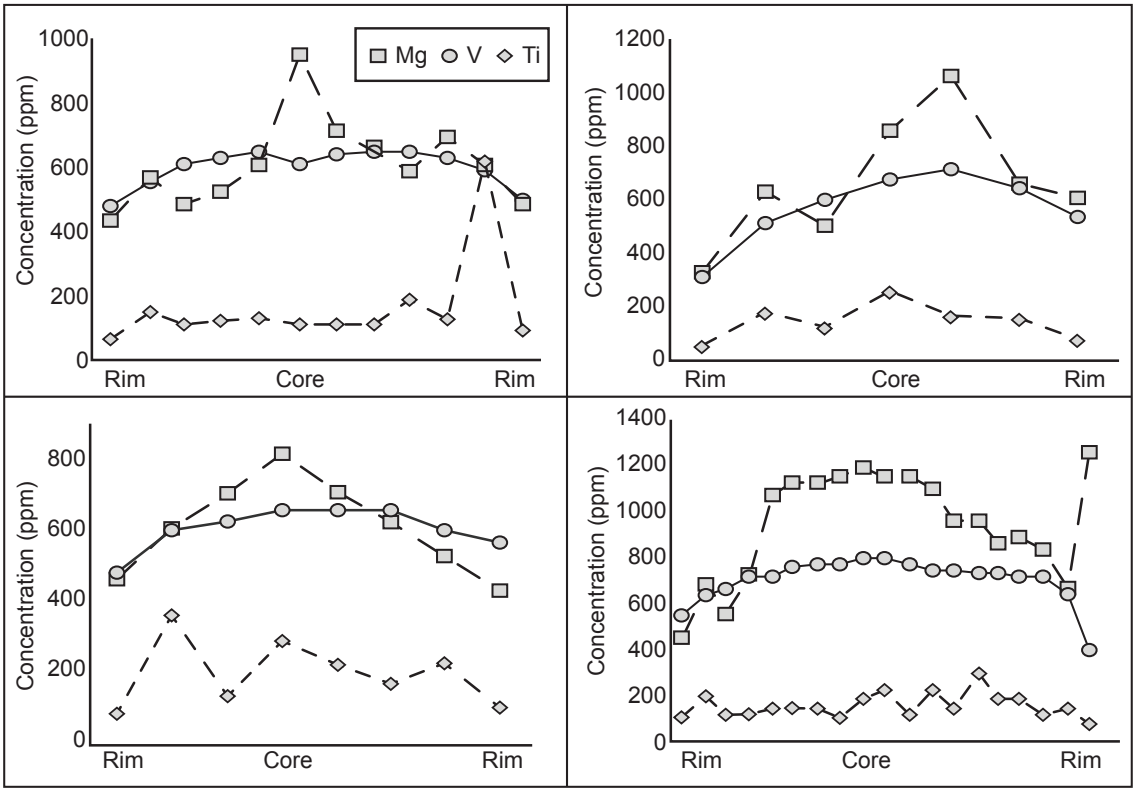

Figure 1.6: Grain transect plot of Mg, V and Ti concentrations in ppm (Al was not measured). Individual symbols represent laser spot analyses across a single magnetite grain (> 700 μm). The rims show relative depletion in these elements, which are interpreted as overgrowths associated with the formation of the smaller, younger magnetite in the sample. Additional LA-ICP-MS transects measuring Mg, V and Ti across four magnetite grains from the serpentinite. Each symbol represents a laser spot (65 μm spot size).

The Pliocene age population in the serpentinite is associated exclusively with smaller grains (300-600 μm) within the sample, which do not show pronounced trace element signatures of blackwall alteration fluids. These ages very likely represent growth, and not cooling, as they are significantly younger than Miocene He ages for zircon from

Syros, which has lower closure temperature than the analyzed magnetite (Soukis and Stockli, 2013). Furthermore, the difference in effective T_c for the two grain size populations is only ~40°C (~245-285°C), based on the published He diffusion kinetics (Blackburn et al., 2007), implying that the age is not the product of localized re-heating. In addition, the trace element geochemistry of the smaller magnetite do not show the same signatures as those that grew during blackwall formation, supporting the interpretation that they formed after these elements were no longer available.

These younger MgHe ages date an episode of serpentinization during fluid flow in brittle shear zones associated with normal faulting at temperatures insufficient to thermally reset the He age of the larger pre-existing magnetite. These ages provide the first direct constraint on the timing of normal faulting that was previously dated as Pliocene on the basis of regional tectonics (Keiter et al., 2004). This localized low-temperature alteration has the potential to overprint earlier geochemical signatures and thus must be carefully considered in studies that use the Kampos location as a proxy for geochemical cycling in subduction zone processes.

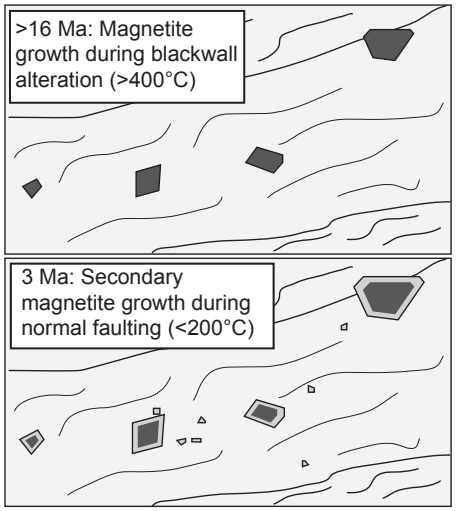

Figure 1.7: Interpreted two-stage magnetite growth based on trace element chemistry and (U-Th)/He age recorded in the serpentinite. Top: Initial magnetite formation during blackwall alteration at temperatures > magnetite T_c. Bottom: Secondary magnetite grain and overgrowth formation in the presence of low Mg, Ti, V and Al post-blackwall alteration, likely associated with Pliocene normal faulting.

Applications and limitations of magnetite dating in serpentinites

This study demonstrates the feasibility of MgHe dating as a reliable thermo- and geochronometer with the ability to differentiate distinctive cooling and alteration episodes in ultramafic rocks. Furthermore, the methodology allows direct dating of magnetite formation in response to low-temperature alteration and tectonic shearing in serpentinites. Given the fundamental impact of serpentinization on a vast array of tectonic, petrological, and geochemical processes, the ability to differentiate and date these alteration events can be used to address significant questions related to serpentinization in exhumed subduction complexes, continental margins, or obducted ophiolites.

Using the current methodology, the primary limitation of MgHe dating is the availability of pure, non-skeletal magnetite of sufficient size due to low parent nuclide concentrations (ppb level), requiring 0.5-1 mg aliquot sizes, and the necessity for abrasion to remove matrix implanted He. As a consequence, dating of small magnetite may prevent single-grain analyses and require combining multiple magnetite grains/fragments, which can lead to mixed age populations. Thus, before constructing multi-grain aliquots for He dating, careful petrologic and geochemical characterization must be done to ensure grains are related to the same formation/alteration event. Such characterization is critical as alteration of ultramafic rocks can be multi-staged and long-lived. Additionally, since the effective T_c of He dating is dependent on grain size and cooling rate, it is important to constrain the temperature of serpentinization or the thermal history of the unit. Future studies can determine whether magnetite formation occurred at temperatures above or below the MgHe T_c through multi-mineral thermochronometry, regional P-T-t constraints, serpentine phase relationships, or oxygen isotope magnetite-serpentine thermometry.

Chapter 2: Magnetite (U-Th)/He cooling history constraints on the metamorphosed Malenco Ultramafic Unit, Italy

Abstract

Serpentinized peridotite has eluded thermochronometric studies causing the timing of their alteration and cooling histories to be relatively unconstrained despite widespread occurrences in orogenic systems. Recent advances in low-temperature chronometry provide a technique to determine the age of magnetite, an alteration mineral in serpentinized peridotite, to directly investigate the timing of alteration and/or cooling events recorded in serpentinized peridotite within orogenic belts. This study uses the magnetite (U-Th)/He method coupled with petrographic analysis and trace element chemistry to investigate the episodic alteration and cooling history of the Malenco Ultramafic Unit in the Italian Alps. Malenco represents a Permian crust-mantle boundary that was exhumed and serpentinized in the Jurassic during continental breakup, and subsequently experienced greenschist to lower amphibolite facies metamorphism since the Cretaceous during the Alpine Orogeny. The timing of the pre-Alpine metamorphic history is relatively well-constrained by zircon U-Pb and amphibole $^{40}Ar/^{39}Ar$ methods, whereas the cooling history related to Alpine contractional deformation and metamorphism is poorly known. Magnetite grains from the eastern and western zones of the Malenco serpentinite were recovered from five samples for dating. Magnetite He results produce a range in ages from ~60 Ma to < 20 Ma that vary with grain size and Th/U ratio. These results reveal a complex history that may be attributed to slow cooling through the magnetite closure temperature consistent with regional thermochronometric data, and renewed magnetite growth with extended metamorphism. These results provide evidence for prolonged, episodic alteration and metamorphism of the Malenco serpentinite, which

likely began with seafloor serpentinization during Jurassic rifting and continued during metamorphism and deformation associated with the Alpine orogeny.

Introduction

Deciphering the spatial and temporal patterns of rock uplift, weathering, and erosion has been integral to understanding the evolution of orogenies and the feedbacks between climate, surface, and lithospheric processes. The tools employed to untangle the geologic history of these complex systems include detailed structural data and field mapping to understand spatial relationships, coupled with pressure-temperature-time (P-T-t) indicators to interpret the changing physical conditions through time. For the temporal component in particular, thermochronology has become an invaluable technique to investigate the exhumation and faulting history of the upper crustal portions of orogenic systems (e.g., Reiners and Brandon, 2006). These thermochronometric systems, including $^{40}Ar/^{39}Ar$, fission track, and (U-Th)/He, have distinct thermal sensitivities and the advantage of providing simultaneous time and temperature information for the same sample. To this end, a significant amount of work has focused on rock-forming and accessory K-, Th- and U-rich phases (e.g., feldspars, micas, zircon, apatite), most commonly found in felsic to intermediate crustal lithologies (e.g., Harrison et al., 1985; Zeitler et al., 1987; Stockli et al., 2000; Reiners, 2005). Ultramafic lithologies, however, have thus far not been readily accessible for dating by these methods as they are generally depleted in K, Th, and U or often lack mineral phases used for radiometric dating. This has presented a challenge for reconstructing complete thermal histories in orogens that incorporate significant components of ancient oceanic crust and mantle.

Mantle peridotite commonly manifests in orogenic belts and suture zones as dissected meter-scale to coherent kilometer-scale tectonized slivers. The origin, age, and

geologic history of these orogenic peridotite units can be difficult to decipher, as primary field relationships are often obscured by tectonic and metamorphic overprinting, and significant serpentinization. Since many peridotite exposures in the Alps are remnants of obducted oceanic lithosphere, it is likely they experienced multiple phases of fluid-rock interaction and metamorphism over million-year timespans. Initial cooling and alteration can occur during an oceanic phase via hydrothermal fluid circulation at a mid-ocean ridge or serpentinization during extreme crustal thinning and mantle exhumation associated with continental rifting (e.g., Skelton and Valley, 2000; Müntener et al., 2000; Mevel, 2003; Pinto et al., 2015). Subsequent or continued fluid-rock interactions can persist during subduction and orogeny, including new mineral crystallization, as well as serpentinization or de-serpentinization reactions (e.g., Fruh-Green et al., 1990; Burkhard, 1993; Debret et al., 2013; Scambelluri et al., 2015). Although detailed structural, petrographic, and geochemical studies can provide significant insight and aid in unravelling the history of these units, the temporal context of these events has remained largely undefined in serpentinites and meta-serpentinites.

Recent work has demonstrated the ability of magnetite to differentiate between multiple alteration episodes within serpentinites based on He age, trace element chemistry, and grain size (Cooperdock & Stockli, 2016). This study also showed that serpentinites continue to be reactive during metamorphism, faulting, and fluid circulation, leading to episodic magnetite formation that can be distinguished by (U-Th)/He age. The (U-Th)/He dating system provides two useful pieces of information for the history of serpentinites in orogenic settings. First, the technique provides an age, which can be placed into context with surrounding lithologies in order to test proposed field relationships. And second, since magnetite (U-Th)/He has an experimentally calculated closure temperature of 250 ± 40°C (Blackburn et al., 2007) that is empirically supported by results from Cooperdock and

Stockli (2016), the technique can be strategically used in concert with $^{40}Ar/^{39}Ar$ and fission track or other (U-Th)/He chronometers to constrain high-resolution thermal histories from middle to upper crustal temperatures. The Malenco Ultramafic Unit in the central eastern Alps is a classic example of a meta-serpentinite with a multi-stage metamorphic history that has few direct age constraints. Here we apply the magnetite (U-Th)/He methodology to investigate the timing and duration of metamorphism and cooling recorded by magnetite in the Malenco serpentinite.

Pre-Alpine Geologic History

The Malenco Ultramafic Unit is composed of nearly 200 km^2 of serpentinized peridotite on the border of southeastern Switzerland and northern Italy (Fig. 2.1). This unit is part of the Malenco-Forno Nappe and marks the southern extent of a series of ultramafic units, including the Totalp and Platta localities, that extend for ~60 km from Davos, Switzerland to Valmalenco, Italy. Geochemical, field, and geochronological studies indicate the serpentinites exposed in Davos, Platta, and Malenco represent remnants of a Jurassic hyper-extended passive margin that were inverted during Alpine nappe stacking beginning in the Cretaceous (e.g., Desmurs et al., 2001; Schaltegger et al., 2002; Manatschal et al., 2007; Manatschal and Müntener, 2009) (Fig. 2.2).

Specifically within the Malenco Unit, multiple phases of the regional tectonic and metamorphic history are preserved in the lithologies and present day field relationships. Lower crustal gneiss and upper subcontinental peridotite represent a Permian crust-mantle transition that persisted for an estimated 50 My at temperatures > 600 - 650°C (Müntener et al., 2000) prior to Jurassic rifting. The timing of this relationship is constrained by the Permian Bracca gabbro (270 +6/-4 Ma; Hansmann et al., 2001), which seals the contact between the (now serpentinized) peridotite and lower crustal gneisses.

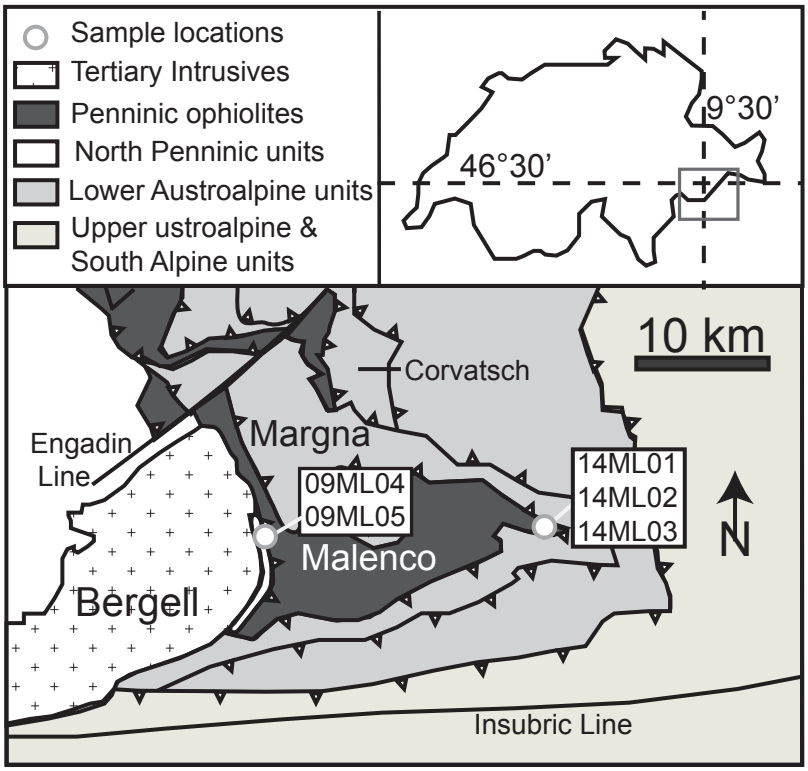

Figure 2.1: Geologic map of Malenco Ultramafic Unit with sample locations modified after Schaltegger et al., 2002.

Jurassic rifting caused extreme crustal thinning, mantle exhumation, and seafloor brecciation that resulted in extensive serpentinization (Burkhard and O'Neil, 1988; Trommsdorff et al., 1993; Froitzheim and Manatschal, 1996) (Fig. 2.2). Field evidence includes preserved rift-related contacts between serpentinized subcontinental mantle and detachment-related ophicarbonate and tectono-sedimentary breccias of mixed crustal and mantle clasts (Trommsdorff and Evans, 1977; Mellini et al., 1987; Müntener et all, 2000; Hansmann et al., 2001). Evidence for static seafloor serpentinization includes preserved serpentine mesh textures after olivine, δD (-42 to -34 ‰) and $\delta^{18}O$ (4.4 to 7.4 ‰) values that suggest moderate-temperature serpentinization dominated by seawater, as well as

rodingitized intrusions with MORB-affinity in the serpentinite (Burkard and O'Neil, 1988; Pozzorini, 1996, Müntener et al., 2000).

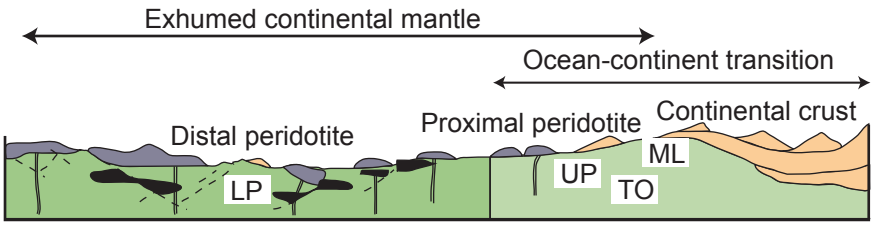

Figure 2.2: Schematic cross section of the study area during Jurassic rifting, including the ocean-continent transition zone and zone of exhumed continental mantle. Abbreviations used to label units are ML = Malenco, TO = Totalp, UP = Upper Platta, LP = Lower Platta. (Modified from Müntener et al., 2004).

Alpine Geologic History

Cretaceous Alpine deformation began with top-to-the-west thrusting (Froitzheim et al., 1994; Handy, 1996). During this period, the Malenco Unit experienced lower amphibolite-facies metamorphic conditions, with peak pressures of 0.4 to 0.7 GPa, as constrained by Na-in-amphibole barometry (Bissig and Hermann, 1999), and peak temperatures of ~ 450°C as inferred from calcite-dolomite and garnet-amphibole thermometry (Trommsdorff and Evans, 1977; Mellini et al., 1987; Hermann et al., 1997). This was followed by top-to-the-east normal faulting and cooling to greenschist-facies conditions (Froitzheim et al., 1994; Handy, 1996).

In the Oligocene (31-28 Ma), the study area underwent N-S shortening from continued convergence between Adria and Europe (Fig. 2.3) (Froitzheim et al., 1994). At this time the Bergell tonalite-granodiorite intruded the western zone and caused amphibolite- to granulite-facies contact metamorphism, with a contact aureole extending ~3 km into the Malenco Unit (Trommsdorff and Evans, 1972; Trommsdorff and Evans,

1980; Von Blanckenburg, 1991; Trommsdorff and Connolly, 1996; Oberli et al., 2002). Backthrusting along the Insubric Line caused synmagmatic deformation of the Bergell intrusion, although the exact timing is poorly constrained between 34 and 20 Ma (Fig. 2.3) (Schmid, 1996; Berger et al., 2011). A final period of deformation occurred as oblique sinistral brittle deformation along the Engadine Line in the late Oligocene to middle Miocene, which accompanied uplift in the study area (Fig. 2.3) (Schmid and Froitzheim, 1993).

The petrologic effects of these Alpine metamorphic events will be discussed in the next section. However, it is worth noting that each of these phases of metamorphism, deformation, and hydrothermal alteration can cause new mineral growth and recrystallization in the serpentinized peridotite, which remains reactive during partial to full serpentinization and de-serpentinization reactions.

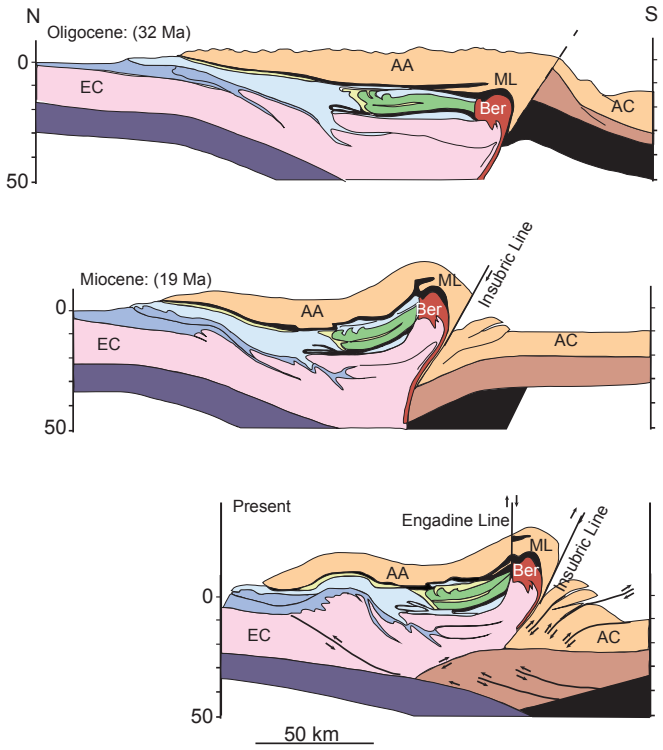

Figure 2.3: Cross section sketches of the kinematic evolution of the Central – Eastern Alps from the Oligocene to present, (modified after Schmid et al., 1996). Abbreviations used to label units are ML = Malenco, Ber = Bergell Intrusion, AA = Austroalpine units, EC = European Crust, AC = Adriatic Crust.

Petrologic Description

Malenco ultramafic rocks are composed primarily of serpentinized spinel-peridotites with minor amounts of pyroxenite and websterite (Müntener and Hermann, 1996). Alpine metamorphism replaced the original serpentine with antigorite. Although, mesh texture after olivine is present in some less deformed samples as a record of pre-Alpine low-grade hydration during Jurassic rifting (Müntener et al., 2000). Multiple generations of magnetite have been identified in the Malenco serpentinite related to low-grade pre-Alpine serpentinization, as well as during Alpine metamorphism (Fig. 2.4) (Evans and Frost, 1975; Evans, 1977; Trommsdorff and Evans, 1980; Burkhard, 1993; Müntener et al., 2000).

Magnetite forms as an alteration mineral from the breakdown of primary peridotite minerals, namely olivine, or from a secondary reaction that extracts Fe from early-formed Fe-rich serpentine and Fe-rich brucite in most serpentinites (e.g., Bach et al., 2006; Evans 2008, 2010). Magnetite growth at the expense of metamorphosed Cr-spinel is also well documented in Alpine serpentinites (Evans and Frost, 1975; Burkhard, 1993). The latter manifests in two ways. First, Cr-spinel with thin magnetite rims are observed in Alpine serpentinites that underwent low-grade metamorphism (i.e., prehnite to pumpellyite facies at Davos and Platta), which Burkhard (1993) documents and attributes to alteration during seafloor serpentinization. At Malenco, which experienced higher degrees of metamorphism (upper greenschist-facies or to lower amphibolite-facies), Cr-spinel is fully recrystallized to homogenous Cr-rich magnetite (Burkhard, 1993), distinguishable from magnetite associated with initial seafloor serpentinization by larger grain size and higher Cr-content. Finally, regional metamorphic paragenesis consists of antigorite + diopside + olivine + chlorite + magnetite (Trommsdorff and Connolly, 1996). Therefore, three

possible episodes of magnetite growth can be distinguished in the Malenco serpentinites from the Jurassic to the Oligocene (Fig. 2.4).

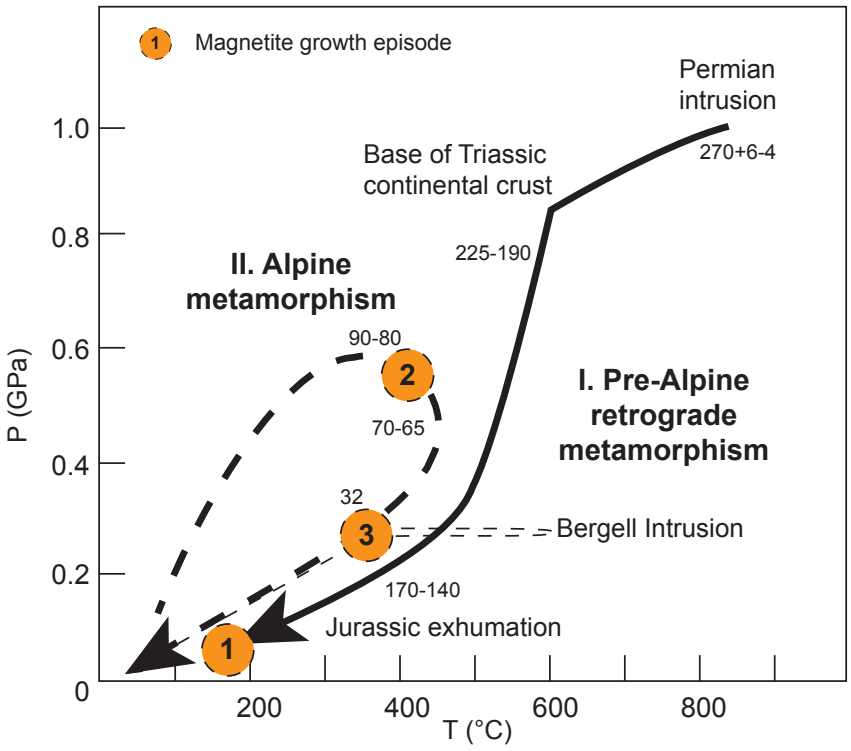

Figure 2.4: Schematic P-T diagram for the Malenco unit after Müntener et al., (2000). The P-T history can be traced to the Permian when the unit was at the crust-mantle boundary. Jurassic extension led to exhumation to the seafloor, resulting in cooling to < 200°C. Cretaceous through Miocene Alpine convergence caused metamorphism that reheated the unit up to ~450°C. Black text numbers refer to age constraints from Villa et al., (2000) and Hansmann et al. (2001). Numbers in orange circles denote possible episodes of magnetite growth based on previous work discussed in text.

Metamorphic and cooling history

Previous chronometric studies on Malenco and surrounding units provide temporal context for the episodic regional metamorphic history from the Permian through the Cenozoic. The pre-Alpine history of the Malenco Unit is constrained by field relationships with datable lithologies. As mentioned in the previous section, an early Permian crust-

mantle transition history is recorded by the Bracca gabbro ~ 270 Ma (Hansmann et al., 2001). The timing of oceanic rifting can be approximated by Jurassic sediments that cap MORB-type intrusions through the Malenco serpentinite and Forno volcanic units (Peretti and Köppel, 1986). Subsequent Upper Cretaceous Alpine-related metamorphism is loosely constrained by $^{40}Ar/^{39}Ar$ ages on multiple generations of amphibole, which span from ~90 to 65 Ma (Villa et al., 2000). More recently, from 31 to 28 Ma, the Bergell tonalite-granodiorite intruded and caused contact metamorphism on the western boundary of Malenco (Trommsdorf and Evans, 1977; Von Blanckenburg, 1991; Oberli et al., 2004).

Apatite fission track and (U-Th)/He studies on the Bergell granodiorite at the western contact of the Malenco Unit provides constraints on the local cooling history post-intrusion. Boulders derived from the Bergell are found in Late Oligocene sediments and have apatite fission track ages of 26 to 23 Ma, providing evidence for rapid uplift post intrusion coincident with brittle movement along Engadine Line (Wagner et al., 1979; Hansmann, 1996). Apatite (U-Th)/He from a vertical transect up the Bergell confirms moderate to fast exhumation through the apatite closure temperature (~ 60°C) by 20 Ma (Maheo et al., 2012).

Thermal modeling estimates pre-intrusive ambient temperatures in the Malenco serpentinite of about 350 ± 20°C, and a geothermal gradient of 28 ± 2°C (Trommsdorff and Connolly, 1996). This estimate, coupled with peak temperature estimates of 450°C at ~ 65 Ma (Trommsdorff and Connolly, 1996 and refs therein; Villa et al., 2000) implies cooling rates as slow as 3°C/My from 65 to 30 Ma. Such slow cooling is consistent with zircon (U-Th)/He results from neighboring Austroalpine nappes (Corvatsch, Grosina) that record slow cooling (~1°C/my) through the zircon He partial retention zone from ~50 to 30 Ma (Evans, 2011).

With these petrologic and chronologic studies as a basis, several predictions may be made regarding what constraints magnetite (U-Th)/He can provide for the thermal and alteration history of the Malenco Ultramafic Unit. Given the magnetite He closure temperature of 250 ± 40°C, the magnetite chronometer is expected to either record ages associated with cooling or growth below ~200-300°C. In western Malenco, one would likely predict that magnetite cooling ages should post-date the thermal overprint of the Bergell intrusion (30 Ma), and pre-date apatite (U-Th)/He cooling ages from within the Bergell (>20 Ma). In contrast, in eastern Malenco, magnetite He ages are more likely to record slow cooling since Cretaceous upper greenschist metamorphism, or possibly growth during Oligo-Miocene backthrusting and uplift (Schmid and Froitzheim, 1993; Handy et al., 2010). To test this, samples were selected for magnetite (U-Th)/He dating from the western and eastern sections of the Malenco Unit, including meta-serpentinites from within the Bergell contact aureole, and samples from > 20 km outside the aureole.

Sample Descriptions

Five samples were selected for magnetite (U-Th)/He dating based on the availability of crystalline magnetite of sufficient size for analysis. In all samples magnetite was present as clusters of grains associated with chlorite, or within serpentine as isolated grains or in veins (Fig. 2.5). Other opaque minerals include anhedral and intergrown non-magnetic sulfide minerals, which were easily distinguished by grain morphology and lack of magnetism. Two meta-serpentinite samples (09ML04, 09ML05) were collected near the western boundary of the Malenco Unit from within the contact aureole of the Bergell intrusion. 09ML04 is characterized by pyroxene, olivine and randomly oriented, coarse-grained antigorite. 09ML05 was sampled closest to the Bergell contact and contains the least amount of serpentine of all the samples due to dehydration reactions and metamorphic

olivine growth. Granular pyroxene and metamorphic olivine grains dominate, with a minor amount of antigorite needles. Bands of coarse tremolite cut across the granular background. In both samples, large opaque minerals (mm-cm) occur as amalgamated μm-sized sub-grains altered to magnetite.

Three samples (14ML01, 14ML02, 14ML03) were collected from ~20 km to the east in the vicinity of Pass d'Ur. Samples from the Pass d'Ur area consist of serpentinized peridotite with preserved high-temperature spinel foliation locally in contact with ophicarbonate and tectono-sedimentary breccias consisting of mixed ultramafic and mafic clasts. A zone of highly sheared serpentinite occurs at the contact between a body of massive serpentinite that preserves peridotite spinel foliation and overlying ophicarbonate and breccias. Samples were collected from the 'massive' serpentinite with preserved spinel-foliation (14ML01), sheared serpentinite (14ML02), and ophicarbonate (14ML03). Unlike the samples from the Bergell contact aureole, the 'massive' serpentinite (14ML01) contains no relict or metamorphic olivine or pyroxene. The sample is composed entirely of fine- to medium- grained antigorite and chlorite. Spinel grains are elongated and altered to magnetite, surrounded by fine-grained chlorite and serpentine. The sheared serpentinite sample, 14ML02, has distinct shear bands deforming serpentine and spinel. Minor pyroxene is present with antigorite needles. The ophicarbonate sample, 14ML03, is composed primarily of carbonate minerals interlayered with ultramafic minerals including serpentine, pyroxene, olivine and magnetite.

Table 2.1. Malenco sample location and descriptions

Sample	Location	Description
Eastern Malenco (Pass d'Ur)		
14ML01	46°18'21.92"N 9°59'54.43"E	Antigorite, chlorite, magnetite
14ML02	46°18'17.65"N 9°59'53.73"E	Antigorite, chlorite, pyroxene, magnetite, amphibole
14ML03	46°18'16.26"N 9°59'54.68"E	Carbonate, magnetite, olivine, pyroxene
Western Malenco (Metamorphic Aureole)		
09ML04	46°17'47.58"N 9°46'12.32"E	Olivine, pyroxene, antigorite, magnetite, chlorite
09ML05	46°17'41.50"N 9°45'43.31"E	Olivine, pyroxene, magnetite, chlorite, tremolite, antigorite

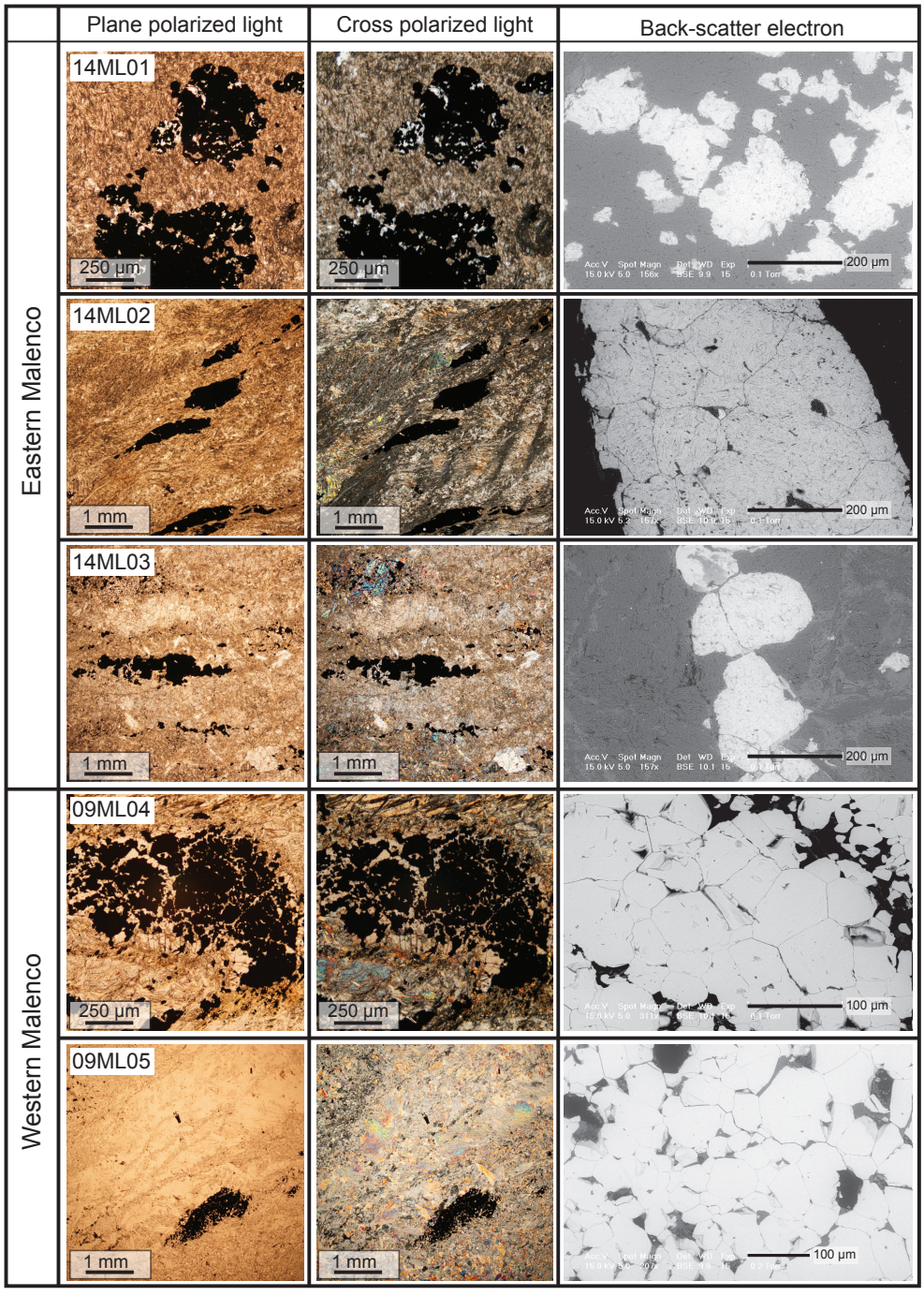

Figure 2.5: Photomicrographs and backscatter electron images of representative magnetite grains from all five samples. Large (mm-size) masses of opaque minerals are c of 100-300 μm Cr-rich magnetite sub grains.

Magnetite (U-Th)/He Chronometry

Magnetite grains were separated from each of the five samples and dated with (U-Th)/He chronometry to address the timing of magnetite cooling or growth in the Malenco unit. Groundwork for the magnetite (U-Th)/He technique established that magnetite can be used as a viable geochronometer for fast-cooled intermediate to mafic volcanic rocks (Fanale and Kulp, 1962; Blackburn et al., 2007). More recently, magnetite (U-Th)/He dating was extended to subduction-related serpentinites and chlorite schist blackwall rocks (Cooperdock and Stockli, 2016). This work demonstrated the ability for magnetite to function as a thermochronometer by measuring cooling ages associated with exhumation post-subduction, as well as a geochronometer to date magnetite associated with late-stage, low-temperature magnetite growth. The current study seeks to expand upon this recent work to date the cooling and alteration history of serpentinites in slow cooled samples that experienced a complex metamorphic and tectonic history in the Alpine Orogeny.

(U-Th)/He chronometry measures ages based on the radiogenic production of ^{4}He from the alpha decay of ^{238}U, ^{235}U, ^{232}Th and ^{147}Sm. The (U-Th)/He age of a mineral is a function of He diffusivity, grain size, and the cooling history of the sample. Therefore, to properly interpret the significance of a measured (U-Th)/He age, it is necessary to know the He diffusion kinetics for the mineral being dated and the geologic history of the sample under investigation. The He diffusion kinetics for magnetite were measured by step-heating diffusion experiments on 500 μm fragments of kimberlitic magnetite, which determined a nominal closure temperature of 250 ± 40°C for a 10°C/My cooling rate (Blackburn et al., 2007). Using these kinetics, the thermal sensitivity of He in magnetite can be modeled based on variations in grain size and cooling rate (Fig. 2.6). Thus, a magnetite He age can either represent a cooling age or the formation age, depending on the thermal history and magnetite growth history of the sample. Particularly in serpentinites, in which multiple

generations of magnetite growth at different temperature conditions is possible, it is necessary to incorporate independent geological constraints, such as other thermochronometry, P-T estimates, and mineralogy to interpret a magnetite He age. This can be aided by identification of serpentine polymorph (lizardite vs antigorite), which can be pressure and temperature dependent (e.g., Evans, 2010), or variations in trace element concentration for different generations of magnetite (e.g., Cooperdock and Stockli, 2016). In the present study, magnetite He age interpretation benefits from previous work that reports regional thermochronology, and local P-T estimates based on petrography.

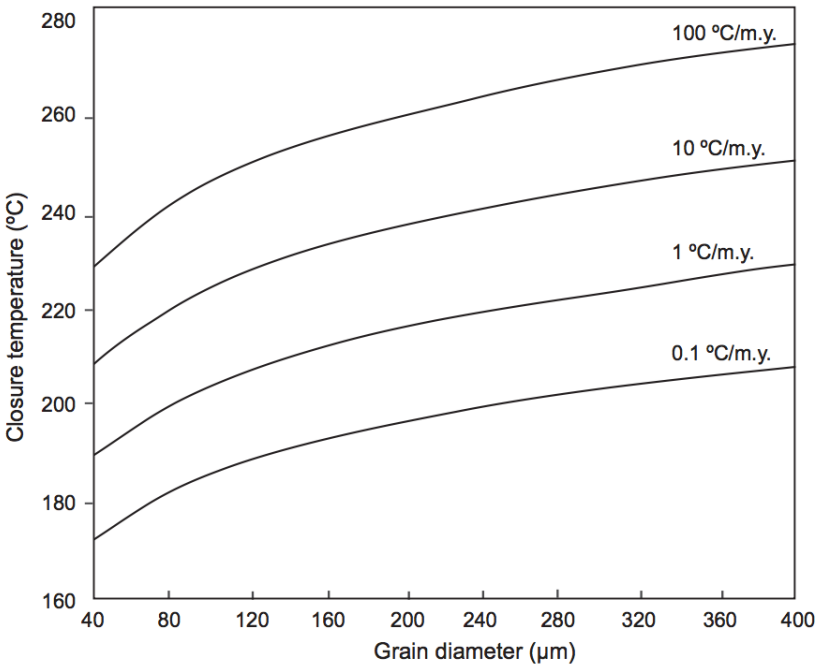

Figure 2.6: Magnetite (U-Th)/He closure temperature as a function of grain size and cooling rate. Closure temperature values are calculated with magnetite He diffusion values reported in Blackburn et al., (2007) (E_a = 54.7 kcal/mol and D_o = 34.3 cm^2s^{-1}).

Methods

Sample preparation

Samples were processed using standard mineral separations techniques at The University of Texas at Austin. Whole rock samples were crushed with jaw and cone crushers, followed by density separation on a Gemini water table. A hand magnet was used to separate the magnetite fraction from the heavy mineral separate for picking.

Thirty to fifty single grains were selected from four out of five samples using an optical microscope and mounted on double-sided sticky tape for X-Ray Computed Tomography (CT) scanning at The University of Texas High-Resolution X-Ray Computed Tomography Facility (Appendix 3). CT allows for non-destructive imaging of the entire grain volume at a 6 μm resolution. CT is used to ensure that magnetite grains are clear of inclusions, fractures or attached matrix that can affect the He systematics in the grain. All samples were CT scanned prior to dating except for magnetite grains from 09ML04. The effects of this will be discussed in the next section.

Physical air abrasion was employed to remove ~20 μm of the outer grain boundary where excess He can be present due to implantation from high U-Th neighboring phases. After CT scanning, the internally homogeneous grains were physically air abraded for 2-4 hours at 6 PSI following procedures in Blackburn et al. (2007) and Cooperdock and Stockli (2016).

Malenco magnetite parent nuclide concentrations are very low (~5 to 60 ppb), requiring aliquot masses >100 μg to ensure sufficient U, Th, Sm and He for robust mass spectrometer measurements with sufficient counting statistics. The aliquots in this study were constructed with multiple abraded grains (n = 2 to 17) that totaled ~100 to 700 μg of material for (U-Th)/He analysis.

(U-Th)/He analysis

Grains were loaded into 1 mm platinum tubes and the ^{4}He gas was extracted by laser heating with a Photonmachine Diode Laser at ~1050°C for 10 min. The released ^{4}He gas was cryogenically purified and measured by isotope dilution on a Blazers Prisma QMS-200 quadrupole mass spectrometer (QMS). Full 10-minute procedural blanks were run between each unknown measurement to determine the magnitude and reproducibility of machine background over the run. Aliquots were reheated in 10 minute increments until the He yield became ≤ 2x blank values or re-extracts became < 1% of the total He. Final ^{4}He measurements were calculated using a calibration against a manometrically-determined ^{4}He standard and blank-corrected corresponding to the procedural blank following the gas extraction step. Typical ^{4}He analytical uncertainties ranged from <1% up to 6%, with a strong correlation with ^{4}He concentration.

After degassing, grains were unpacked from the platinum tubes into 15 mL Savillex vials, spiked with 100 μl of ^{235}U, ^{230}Th and ^{149}Sm in 5% HNO_3 and dissolved using a two-step HF-HNO_3 (5:1) - HCl hot plate dissolution procedure (Appendix 1). After the initial HF-HNO_3 step, samples were dried down and brought back into solution with concentrated HCl and heated overnight to ensure complete Th recovery. After chloride conversion, the solution was dried down and brought back up with 100 μl of 7N HNO_3 and 500 μl of MilliQ H_2O for analysis on a Thermo Element 2 HR-ICP-MS. Final U-Th-Sm concentrations were determined by isotope dilution with a mixed spike calibrated against a gravimetric 1 ppb U-Th-Sm standard solution. Analytical uncertainties varied by isotope with Th uncertainties of < 1%, U < 2% and Sm < 6%. The relatively high uncertainty in some Sm measurements is a function of extremely low concentrations (< 10 ppb) in these magnetite grains.

Final (U-Th)/He ages were calculated by iteratively solving the He age equation using blank corrected He, U, Th and Sm concentrations. The errors assigned to individual age measurements are maximum analytical errors based on the analytical uncertainties in the U, Th, Sm and He measurements.

Whole rock U, Th, Sm measurements

U, Th and Sm trace element analyses for the same five samples dated for magnetite (U-Th)/He were measured at Lamont-Doherty Earth Observatory. 100 mg of whole rock powders were dissolved with Na_2O_2 sinter following the procedures outlined in Meisel et al. (2002) to ensure complete digestion of chromite and other refractory accessory minerals. Trace elements were analyzed on a VG PlasmaQuad ExCell quadrupole ICP-MS. All reported analyses are blank corrected by procedural blanks run after every four unknowns.

Quality control was monitored through rock standards (UB-N,), procedural blanks, and drift and standard solutions. Final trace element concentrations were calculated after drift correction using a standard solution curve. Values for whole rock U, Th and Sm concentrations are reported in Table 2.2, and discussed in association with Fig. 2.9.

Magnetite (U-Th)/He Results

A total of 24 (U-Th)/He ages were measured on five serpentinite samples from the western and eastern zones of Malenco.

Western Malenco

Magnetite ages from two samples (09ML04 and 09ML05) were analyzed from within the Bergell contact aureole in western Malenco. In contrast to the other samples in this study, magnetite grains from sample 09ML04 were not CT scanned prior to analysis and therefore there is no way to confirm the internal homogeneity of the analyzed grains.

This may have contributed to the scattered age results for four aliquots, ranging from 28.4 ± 1.4 Ma to 59.3 ± 1.2 Ma with no correlation with aliquot mass or chemistry. Magnetite crystals from sample 09ML05 were CT scanned prior He analysis. Due to a limited quantity of homogeneous magnetite material after the CT and air abrasion steps, only two aliquots from sample 09ML05 were analyzed producing He ages of 11.9 ± 0.7 Ma and 17.9 ± 1.5 Ma (Table 2.2).

The number of grains in each aliquot is not available for these two samples, however total aliquot masses are documented. The two aliquots from sample 09ML05 had the lowest masses analyzed (60 and 68 μg), resulting in relatively higher propagated He age analytical errors (6-8%). Sample 09ML04, on the other hand, had total aliquot masses from 448 to 1341 μg and analytical uncertainties < 5%. Although the precise grain size measurements in these aliquots are not documented, the variation in aliquot mass correlates with grain size, such that larger mass aliquots are composed of larger grain sizes (Fig. 2.7). Following this trend, 09ML05 is likely composed of smaller grains (~100 μm in diameter), whereas 09ML04 consists of larger grains (150 - 200 μm), consistent with observations for typical grain sizes in these samples from back scatter electron images (Fig 2.2).

The scattered age results that pre-date Bergell metamorphism in sample 09ML04 emphasize the importance of CT scanning prior to magnetite (U-Th)/He analysis. Without CT, it is impossible to ensure that the analyzed grains are free of inclusions or internal fractures, which can introduce greater uncertainty in the results. If inclusions were present and not fully dissolved by the magnetite dissolution procedure, then there may be a parentless ^{4}He component causing the He age to be erroneously old. This may explain the 09ML04 age results older than the Bergell intrusion, and could imply that these results are erroneously old.

Eastern Malenco

The samples from Pass d'Ur exhibit a comparable range in ages to those collected within the metamorphic aureole. Two aliquots from sample 14ML01, composed of 9 and17 grains with average grain sizes of 230 μm and 166 μm, respectively, yield He ages of 16.9 ± 0.4 Ma and 14.2 ± 0.6 Ma (Table 2.2).

Nine aliquots from 14ML02 produce magnetite ages that range from 17.3 ± 1.8 Ma to 62.2 ± 1.3 Ma. Aliquots were composed of 2 to 14 grains, with average grain sizes from 148 to 311 μm.

Six aliquots from 14ML03 composed of 4 to 12 grains, with average grain sizes of 186 to 327 μm yield magnetite He ages from 21.0 ± 1.3 Ma to 59.4 ± 2.3 Ma, with one that yielded an anomalously old age of 98.8 ± 1.9 Ma (Table 2.2). The significance of this old age is unknown, but there are multiple possibilities. First, it may represent a very old cooling age, which was not affected by 450°C high-temperature metamorphism. Alternatively, it could suffer from excess He or incomplete dissolution. As no other sample produced a similar age, it is treated as an outlier and not discussed further.

There is no clear correlation between magnetite age and distance from the Bergell intrusion; however, there are distinct age trends with average grain size and Th/U ratio. Four out of five samples have aliquots with ages younger than the Bergell intrusion (< 30 Ma) (Fig 2.8), which are on average composed of smaller grains (129 - 311 μm), and have higher Th/U (0.87 – 4.04) than aliquots with ages 30 Ma or older. Three out of five samples yield ages that coincide with the Bergell intrusion and older (≥ 30 Ma). These aliquots are composed of larger grains (206 – 327 μm), and have lower Th/U (0.20 – 1.93). As uranium concentrations are consistent between all aliquots, the increased Th/U is due to a higher concentration of Th in the < 30 My magnetite grains (Fig. 2.8).

Table 2.2: Malenco magnetite (U-Th)/He age data

Sample	Age	U (ppb)	Th (ppb)	Sm (ppb)	^{4}He (nmol/g)	Th/U	Mass (µg)	# of Grains	Avg. Grain Mass (µg)	Avg. ESD (µm)
Eastern Malenco (Pass d'Ur)										
mg14ML01-1	16.9 ± 0.4	24	70	9	0.004	3.0	294	9	33	230
mg14ML01-2	14.2 ± 0.6	21	95	7	0.003	4.6	206	17	12	166
14ML01 Whole Rock:		*7*	*35*	*205*		*5.3*				
mg14ML02ab-1	20.9 ± 3.0	12	28	25	0.002	2.4	160	2	80	311
mg14ML02ab-2	44.7 ± 4.6	21	15	11	0.006	0.7	176	6	29	222
mg14ML02ab-3	17.3 ± 1.8	29	117	325	0.006	4.0	103	12	9	148
mg14ML02ab-4	24.0 ± 1.3	21	20	4	0.003	0.9	188	8	24	206
mg14ML02ab-5	42.7 ± 2.5	10	19	3	0.003	1.9	238	10	24	207
mg14ML02ab-6	41.1 ± 1.3	20	18	3	0.005	0.9	326	14	23	206
mg14ML02ab-7	40.5 ± 1.1	15	23	3	0.005	1.5	542	6	90	323
mg14ML02ab-8	62.2 ± 1.3	17	27	4	0.008	1.6	458	8	57	278
mg14ML02ab-9	30.9 ± 0.9	18	35	6	0.004	1.9	283	11	26	213
14ML02 Whole Rock:		*14*	*27*	*131*		*2.0*				
mg14ML03-1	26.9 ± 1.4	26	23	5	0.005	0.9	155	9	17	186
mg14ML03-2	36.6 ± 1.2	36	20	4	0.008	0.6	195	4	49	263
mg14ML03ab-1	44.0 ± 1.8	17	5	2	0.004	0.3	322	9	36	238
mg14ML03ab-2	59.4 ± 2.3	12	5	2	0.004	0.4	480	6	80	311
mg14ML03ab-3	98.8 ± 1.9	14	6	3	0.009	0.4	655	7	94	327
mg14ML03ab-4	41.4 ± 0.8	16	7	2	0.004	0.4	410	12	34	234
mg14ML03ab-5	21.0 ± 1.3	18	27	5	0.003	1.5	212	12	18	188
14ML03 Whole Rock:		*33*	*9*	*481*		*0.3*				
Western Malenco (Metamorphic Aureole)										
mg09ML04-1*	28.4 ± 1.4	35	25	14	0.006	0.7	448	n/a	n/a	n/a
mg09ML04-2*	49.1 ± 0.8	28	6	10	0.008	0.2	1341	n/a	n/a	n/a
mg09ML04-3*	59.3 ± 1.2	28	47	20	0.013	1.7	626	n/a	n/a	n/a
mg09ML04-6*	35.0 ± 0.6	45	70	66	0.012	1.6	694	n/a	n/a	n/a
09ML04 Whole Rock:		*18*	*6*	*47*		*0.3*				
mg09ML05-1	11.9 ± 0.7	33	124	24	0.004	3.8	60	n/a	n/a	n/a
mg09ML05-2	17.9 ± 1.5	50	62	4	0.006	1.2	68	12	6	129
09ML05 Whole Rock:		*28*	*29*	*83*		*1.1*				
******* *Magnetite grains not CT scanned*										

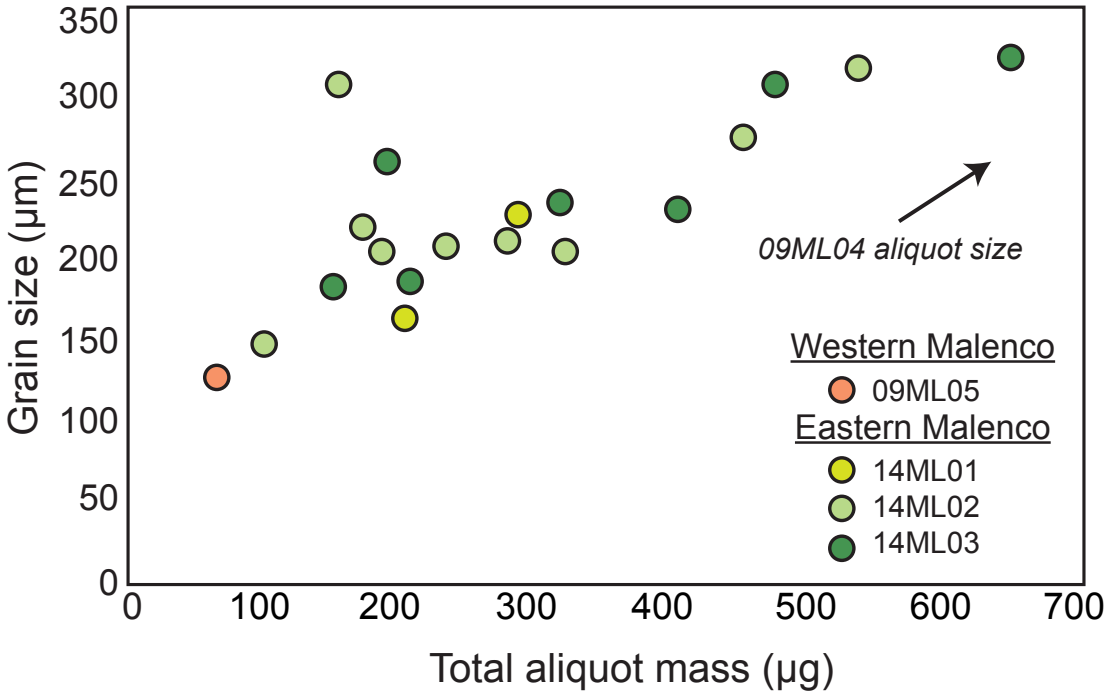

Figure 2.7: Magnetite grain size versus total aliquot mass. The correlation between larger grains and larger overall aliquot mass implies that the aliquots that do not have a recorded number of grains can be approximated by total mass.

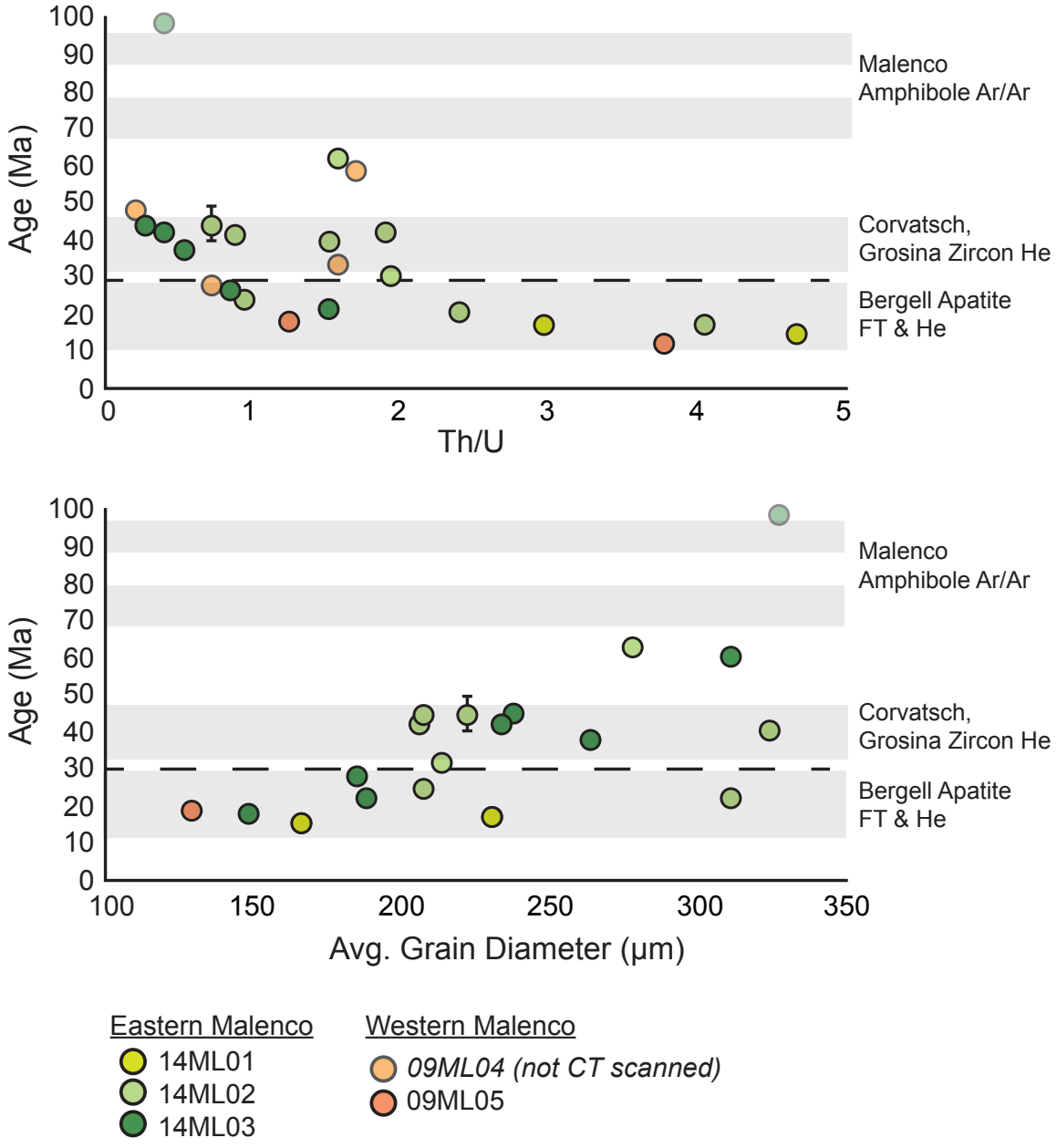

Figure 2.8: Magnetite (U-Th)/He age results plotted by Th/U and average grain size. Top: Magnetite He results have a negative trend with Th/U such that younger magnetite ages have higher Th/U. Bottom: Magnetite He results also have a positive trend with grain size.

Discussion

This study uses (U-Th)/He chronometry to explore the timing of magnetite formation and cooling in the Malenco Ultramafic Unit in response to Alpine tectonic and metamorphic events. The ~ 60 to 12 Ma magnetite He age results provide evidence for a prolonged duration of either 1) cooling, 2) growth, or a 3) combination of growth and cooling. Previous work provides context for key points in geologic history relevant to the formation of magnetite and the thermal history of the serpentinite and will be discussed together with magnetite grain size and magnetite trace element chemistry to distinguish between these three possible scenarios.

First, given the likelihood of multiple episodes of magnetite growth, it is necessary to consider which episode(s) may be captured in the analyzed magnetite. The current magnetite (U-Th)/He procedure has one major limitation in that it requires crushing whole rock samples and individual mineral grains lose their textural context. This does not pose a problem for a sample with one generation of mineral growth, or a fast-cooled sample that has a single cooling age, but it becomes a complicating factor for Malenco samples given the probability for multiple generations of magnetite formation and slow cooling through the magnetite partial retention zone (3°C/My from 65 to 30 Ma; Trommsdorff and Connolly, 1996).

Petrographic analyses on thin sections were employed to define first-order distinguishing characteristics between different magnetite generations, including reflected light microscopy, scanning electron microscope (SEM) back-scatter electron (BSE) imaging and energy dispersive spectroscopy (EDS) (Fig. 2.5). Thin sections from all samples show multiple opaque mineral phases. The most striking and abundant are mm- to cm- sized elongated grain clusters commonly surrounded by chlorite in all five samples (Fig. 2.5). Both reflected light and SEM-EDS of these grain clusters reveal homogenous

magnetite sub-grains ranging from ~ 100 to ~ 300 μm with several wt.% Cr (typically 2-5%). The grain texture, chlorite halo and Cr content strongly suggest these are magnetite grains experienced retrograde recrystallization after Cr-spinel. This interpretation is consistent with Burkhard (1993), who documents spinel fully recrystallized to magnetite at Malenco based on their greater homogeneity and lower occurrence of microscopic pores within the altered spinel grains compared to spinel from lower-grade localities (e.g., Davos).

While the magnetite grains analyzed for (U-Th)/He did not have their Cr concentration measured, the euhedral to subhedral grain morphology and the grain sizes (~130 to 330 μm) suggest that the dated grains may have derived from the Cr-rich metamorphic magnetite population observed in thin section. This would suggest that at least some of the magnetite analyzed in this study were likely altered from spinel during Alpine metamorphism. Whereas timing of spinel recrystallization to magnetite is inferred to occur during high temperature Alpine metamorphism, the duration of this recrystallization is not known.

Given the published He diffusion kinetics for magnetite, any heating over ~290°C should fully reset the He age of magnetite grains that grew during seafloor serpentinization, high-temperature Alpine metamorphism, or within the Bergell contact aureole. Therefore, magnetite samples taken from western Malenco are expected to have He ages < 30 Ma due to the Bergell thermal overprint, whereas samples from the Pass d'Ur likely are not affected by this heating event, but rather record cooling since regional greenschist facies metamorphism in the Late Cretaceous, or growth during Oligo-Miocene uplift and exhumation (Handy et al., 1996).

Despite these expectations, in western Malenco two samples yield ages significantly younger and older than the Bergell intrusion. Sample 09ML05 yields two

Miocene ages, significantly younger than apatite cooling ages for the Bergell, which constrain cooling below ~ 60°C by 20 Ma (Maheo et al. 2012). The second western Malenco sample, 09ML04, yields four dispersed ages that show no trend with grain size or chemistry, ranging from the lower age of the Bergell intrusion (28 Ma) to significantly older (59 Ma). However, since these grains were not pre-screened using CT, it is possible that the ages older than the Bergell are the result of implanted parentless He into the magnetite from inclusions. This is consistent with the notion that it is highly unlikely that magnetite formed before the Bergell intrusion would retain any He during contact metamorphism that exceeded 450°C (Trommsdorff and Connolly, 1996). Therefore, ages older than the Bergell are cautiously interpreted as 'too old' due to excess He, and ages younger than the Bergell either signify delayed cooling in the Malenco Unit relative to the intrusion itself, or new magnetite growth under the He closure temperature.

Eastern Malenco samples display a similar range in ages from < 20 Ma to about 60 Ma, which is consistent with cooling after peak metamorphic temperatures estimated by $^{40}Ar/^{39}Ar$ (70-65 Ma; Villa et al., 2000). Unlike western Malenco, the thermal effects of the Bergell intrusion are not expected to reset the He age in pre-existing magnetite at 30 Ma, so older He ages in these samples can be reasonably interpreted as cooling. However, magnetite He ages significantly younger than Bergell apatite cooling ages once again require either delayed cooling in both eastern and western Malenco, or new magnetite growth.

I. Implications of episodic magnetite growth

Petrologic evidence indicates that magnetite likely grew in the serpentinite episodically starting during Jurassic seafloor exhumation, through the late Cretaceous, to Miocene tectonism and metamorphism in the serpentinite (Fig 2.4). Episodic magnetite

growth can either lead to 1) a single cooling age, if the entirety of magnetite growth occurred above the closure temperature and then cooled quickly, 2) a range of cooling ages that vary by grain size if the magnetite grew entirely above the closure temperature, but cooled slowly through the magnetite He partial retention zone, or 3) dispersed ages due to magnetite growth above and below the closure temperature, leading to a mixture of formation and cooling ages. As none of the samples yield a single, reproducible age, the first possibility can be ruled out, leaving the second and third options to be considered.

II. Extended cooling or episodic formation?

a) Entirely Cooling

If all magnetite formed during Jurassic serpentinization or high temperature Alpine metamorphism, then the entire range of magnetite age results should represent cooling through the magnetite He closure temperature. Since closure temperature is a function of grain size, smaller grains have a lower effective closure temperature than larger grains. The grain size effect on He ages may become pronounced if samples spend a significant amount of time close to their closure temperature in what is called the "partial retention zone" (PRZ). Exhumed PRZs have been observed in age-elevation profiles (e.g., Reiners et al., 2000; Stockli et al., 2000), as well as within single samples with age-grain size correlations (e.g., Reiners and Farley, 2001). Therefore, for the entire range of magnetite He ages to represent cooling there must be evidence for an age-grain size correlation and very slow cooling from ~ 60 to 12 Ma.

He ages do vary by grain size among the samples (Fig. 2.8). Four out of five samples have aliquots with grains that are < 200 μm that produce ages younger than ~20 Ma, whereas aliquots with larger grain sizes (200-330 μm) yield older He ages. This trend is exemplified by an internal age-grain size correlation observed in sample 14ML03 where

aliquots ages are distributed based on grain size between 21 Ma for an aliquot with ~ 190 μm grains, and 60 Ma for an aliquot with 311 μm grains. There are exceptions to this trend, however, with two aliquots from 14ML01 and 14ML02 producing ages ≤ 20 Ma with average grain sizes of 230 and 311 μm.

The observed age-grain size trend is consistent with slow cooling, which has been documented by others for the Malenco Unit during Alpine metamorphism prior to the Bergell intrusion. Given estimates for temperature conditions from Trommsdorff and Connolly (1996), cooling rates from 450°C to 350°C were as low as 3°C/My from ~60 to 30 Ma. This certainly provides a basis for slow cooling over the time span that magnetite cooling ages record, although at temperatures above what is expected for the magnetite He closure temperature.

Further evidence for slow cooling is provided by zircon (U-Th)/He ages in neighboring Austroalpine nappes that preserve lithologies from the Adriatic distal margin of the Jurassic Alpine Tethys (Evans, 2011). The zircon He cooling ages for the Grosina and Corvatsch Nappes produce cooling ages from 50 to 30 Ma (Evans, 2011), which provide evidence for slow cooling (~ 1°C/My) through the zircon partial retention zone from the Eocene until about 30 Ma in these structurally higher units. This may suggest that the Malenco serpentinite experienced similarly slow cooling at deeper crustal levels through the magnetite partial retention zone during the same time period.

Thus, the data support an intrasample age-grain size relationship and slow cooling through the magnetite partial retention zone from ~ 60 Ma to 30 Ma based on estimated slow cooling rates (1-3°C/My) for Malenco and neighboring Austroalpine units. However, it remains unlikely that the entire range of magnetite He ages from 62 to 11 Ma reflects slow cooling through the magnetite He partial retention zone (i.e. > 200°C). Bergell apatite fission track ages indicate cooling below 120°C by 26 Ma in the region, and apatite He

ages from the Bergell indicate cooling below 60°C by 20 Ma (Wagner et al., 1979; Maheo et al., 2012). Therefore, another interpretation is necessary to account for the youngest magnetite He ages.

b) Cooling and Formation

An alternate interpretation is that magnetite growth continued throughout Alpine deformation and after the Bergell intrusion, which resulted in a mixture of cooling and formation ages. In this scenario, the age-grain size relationship may represent different growth phases wherein smaller grains grew later (e.g., Cooperdock and Stockli, 2016). This may better explain the ≤ 30 Ma magnetite He ages, which postdate the Bergell intrusion and overlap with apatite fission track and He data.

The hypothesis that magnetite continued to grow during metamorphism and deformation may be supported by systematic variation between age and trace element chemistry, along with grain size. Trace element concentrations of U, Th, and Sm that are measured with every (U-Th)/He analysis were used in order to assess a possible age-trace element relationships. Despite their low abundances in ultramafic lithologies in general, these elements may serve as tracers for evolving fluid chemistry or protolith chemistry. In particular, U is fluid-mobile in its oxidized U^{6+} state and may be added to the system during serpentinization by seawater or oxidizing surface fluids (e.g., Seitz and Hart, 1973; Hart and Staudigel, 1982). In contrast, Th and Sm are not fluid-mobile, so enrichments more likely reflect protolith chemistry, magmatic additions or fluids that interacted with neighboring enriched crustal lithologies.

Malenco magnetite He ages trend systematically with Th, and show no trend with U or Sm. Note, this does not mean that Th is the most abundant parent nuclide; in fact, U is the dominant contributor of He in these samples due to higher alpha production rates.

However, there is an observed variation in Th concentration with magnetite grains of differing He age, whereas no trend exists with Sm or U concentration and age. This is reflected in the age – Th/U ratio trend in Fig 2.8. Four out of five samples have aliquots with ages younger than the Bergell intrusion (< 30 Ma). On average, these aliquots are composed of smaller grains (129 -311 μm), and have higher Th/U (0.87 – 4.04) than aliquots with ages 30 Ma or older (Fig. 2.8). Three out of five samples yield ages that overlap with the Bergell intrusion, or older (≥ 30 Ma). These aliquots are composed of larger grains (206 – 327 μm), and have lower Th/U (0.20 – 1.93) (Fig. 2.7). This variation may indicate late-stage magnetite growth of smaller grains when more Th was available in the system, coincident with active deformation associated with Oligo-Miocene backthrusting and uplift (Handy, 1996; Schmid, 1996).

Whether the Th in magnetite is derived internally from the protolith or from an external source is not known. In general, bulk peridotite has low Th concentrations (<< 1 ppm) and, with the exception of rare apatite, no common minerals with Th-affinities (e.g., Hauri et al., 1994; Workman and Hart, 2005). Incompatible elements, like U and Th, can be hosted as grain boundary phases (Bedini et al., 1999), in clinopyroxene (Hauri et al., 1994) or perhaps spinel (Bodinier et al., 1996). Therefore, late-stage magnetite could have accommodated more Th as it became available during the breakdown of these minerals. The concentrations of U and Th were measured on whole rock powders and plotted in Fig. 2.9 to assess whether Th concentrations of magnetite are enriched relative to whole rock concentrations. Additional whole rock, clinopyroxene, orthopyroxene and Ti-pargasite compositional analyses for Malenco peridotites reported in Müntener et al., (2010) are plotted for comparison with individual mineral phases (Fig 2.9).

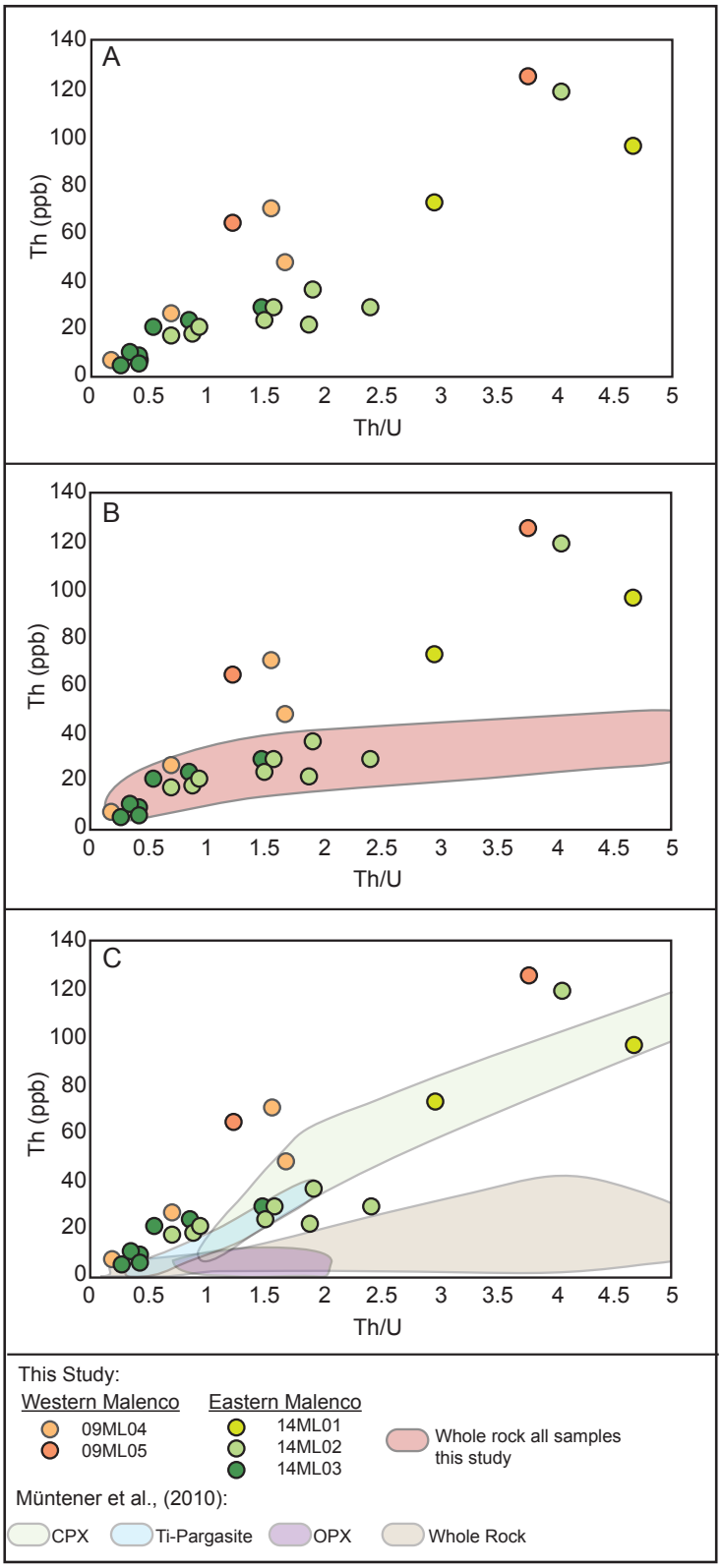

Figure 2.9: Malenco magnetite Th vs. Th/U ratio. A) Magnetite Th/U ratios vary positively from < 0.5 to 5 with Th concentrations from < 10 to 130 ppb. B) Red field shows the range in Th vs. Th/U ratio for whole rock powders from the samples in this study. Several magnetite grains have Th concentrations higher than whole rock values, suggesting magnetite can be an important carrier for Th in meta-serpentinites. C) Colored fields show the Th vs. Th/U for whole rock and minerals reported by Müntener and others, (2010). Magnetite have higher Th concentrations than all whole rock and orthopyroxene samples from this study.

Fig. 2.9 shows that whereas magnetite has a similar range in Th/U as whole rock concentrations, several aliquots are enriched in Th concentration relative to the whole rock. One option is that these enriched magnetite grains incorporated Th from an internal mineral source. Orthopyroxene has low Th concentrations and is an unlikely source for Th in magnetite. Ti-pargasite and clinopyroxene, on the other hand, have similar Th trends to magnetite and breakdown during metamorphism or metasomatism may have been an internal source for Th in newly forming magnetite. As spinel and olivine were not measured, their contributions cannot be assessed. A second, albeit less likely option, is that Th is added to the system. Unlike U, Th is not mobilized in oxidized surface fluids, rather, it may be mobilized through magmatic fluids. Aside from the Bergell intrusion in the western zone, there is no evidence for late-stage magmatism to carry Th into the system in the eastern section. Regardless of source, these data also show that metamorphic magnetite can be a Th host in meta-serpentinites relative to whole rock concentrations.

Taken together, these data indicate that the Malenco magnetite He ages trend with both grain size and Th chemistry, which may indicate different growth events (Fig. 2.10) In such a case, the magnetite He age results may represent a mixture of cooling and formation ages that record slow cooling (~1°C/my) from 60 to ~ 28 Ma, followed by continued magnetite growth below the magnetite He closure temperature (Fig. 2.10).

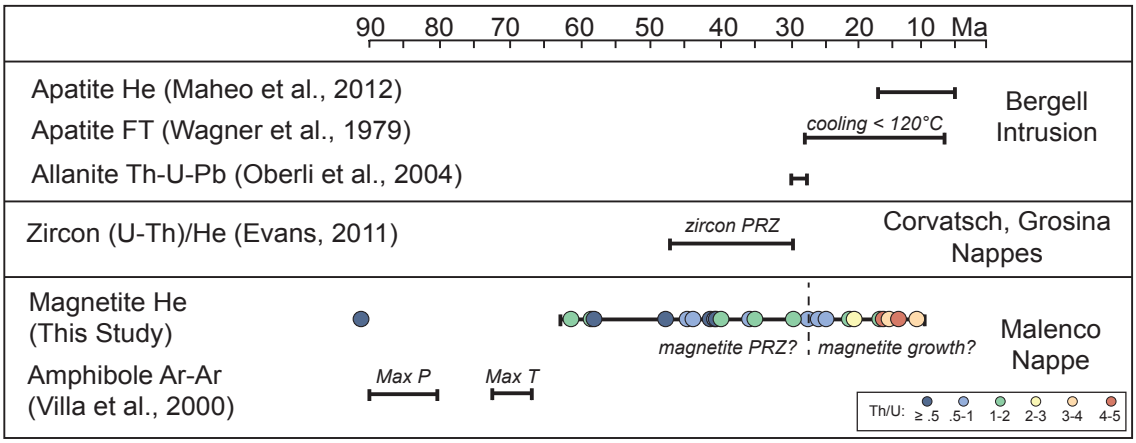

Figure 2.10: Summary of regional cooling ages with magnetite (U-Th)/He from this study. Magnetite data is presented on a color spectrum based on Th/U ratio.

III. Future studies

Several follow-up studies can be done to address open questions left by the observations of the Malenco magnetite (U-Th)/He data. First, a zircon (U-Th)/He study on crustal lithologies within tectono-sedimentary breccias at Pass d'Ur, as well as the Bergell intrusion would provide direct, local constraints for cooling that may be used to better bracket when the magnetite passed through its He closure temperature, and for use with thermal modeling. Second, to address the apparent increase in Th in younger magnetite, a systematic in-situ LA-ICP-MS study to determine host phases for Th, U and Sm may illuminate whether Th is derived internally from progressive mineral alteration, or from an external source. Other trace elements may be used to monitor for small inclusions (e.g., Ce as an indicator of monazite as a Th host). Third, a study to investigate the impact of Cr on He diffusivity in magnetite should be done to determine whether it has a significant impact on closure temperature. Initial magnetite He diffusion experiments were conducted on kimberlitic magnetite that were presumably Cr-free (Blackburn et al., 2007). A compositional effect on He diffusivity has been proposed for other He chronometers, (e.g.,

Cl-content in apatite, Warnock et al., 1997; Farley et al., 2002; Djimbi et al., 2015). If Cr-rich magnetite have different He diffusion kinetics from Cr-free magnetite, this may also contribute to unpredicted cooling ages.

Conclusions

The mid-to-upper crustal thermal histories of meta-serpentinite units in orogenic belts have long eluded study due to a lack of minerals with low-temperature thermochronology techniques. This research applies the magnetite (U-Th)/He thermochronometer to determine the cooling and alteration history (below about 250°C) of the Malenco Ultramafic Unit, Italian Alps, where no other direct low temperature thermochronometric constraints exist. Magnetite dating results on subhedral to euhedral grains, with grain sizes from 130 to 310 μm, range in age from 12 Ma to 62 Ma. We conclude that these results are best explained by a combination of grains that formed above and below the magnetite closure temperature, and therefore represent a mixture of cooling and crystallization ages dating metamorphism. This conclusion is supported by He age trends with grain size, Th chemistry and regional thermochronologic constraints that show cooling below 120°C by 26-15 Ma (Wagner et al., 1979; Maheo et al., 2012). These results provide evidence that the Malenco Ultramafic Unit experienced slow cooling from ~60 to 30 Ma, possibly below 1°C/My. Additionally, comparison of magnetite Th concentrations with whole rock data show that metamorphic magnetite can be a host for Th in meta-serpentinites, which may have implications for Th-cycling in subducted serpentinites.

Chapter 3: Timing and duration of magnetite growth associated with carbonate veining in the SE Semail Ophiolite, Wadi Fins, Oman serpentinite

Abstract

Carbonate alteration of peridotite exposures on earth's surface can occur as mineral replacement reactions and through fracturing and veining. Evidence for these processes is observed throughout Earth's geologic history in continental and oceanic settings, indicating the carbonate hosted within peridotite exposures are likely a significant aspect of the carbon-cycle and may provide an important link for CO_2 dynamics between the atmosphere, hydrosphere, and lithosphere. Central to understanding this process is knowledge of the timing, rates, and timescales for carbonate alteration and veining through geologic history. The Semail ophiolite provides a unique opportunity to explore the timescales carbonate alteration and veining in peridotite, as active and ancient mantle carbonation is evidenced by modern carbonate precipitation in ultramafic hosted springs and extensively carbonated serpentinites within the rock record, respectively. This study analyzes the growth of magnetite within carbonate veins hosted by peridotite. Magnetite likely grew in carbonate veins at the expense of Fe mobilized from serpentinized peridotite during low temperature carbonate alteration. Magnetite (U-Th)/He ages from four samples, with grain sizes ranging in size from 200 μm to 1 cm, produce ages from 27 to 4 Ma, suggesting a prolonged period of growth in the Miocene. This protracted or episodic growth is in contrast with other Oman peridotite carbonation studies, which report much shorter timescales (on the order of thousands of years) for carbonate alteration. The relatively slow reaction rate in this location may be due to a combination of factors, including low temperatures, slow fluid percolation, and slow carbonation reaction rates for serpentine minerals. Furthermore, these results find that timing of carbonate veining at

Wadi Fins is not related to ophiolite obduction in the Cretaceous, or modern incision and erosion, but rather appear to record a period of alteration coincident with Miocene regional shortening and faulting in Oman, likely related to the Zagros-Arabian collision. In sum, this study is the first to document a period of carbonate alteration in the mantle section of the Semail Ophiolite that occurred in the Miocene and lasted over 10's of millions of years.

Introduction

The Semail Ophiolite in Oman is widely recognized as one of the best localities to study the structure and chemistry of obducted oceanic crust amid the extensive exposures and remarkable preservation within the Oman Mountains. The uplift and erosion of the Oman Mountains provides a unique opportunity to study the igneous crustal section of the ophiolite, as well as exceptional access to the oceanic lithospheric mantle. Direct sampling of the mantle section has informed models for high-temperature igneous processes, such as mantle melting and crustal differentiation (e.g., Boudier and Nicolas, 1995; Kelemen et al., 1995; Godard et al., 2000; Braun and Kelemen, 2002; Hanghoj et al., 2010). However, due to the instability of peridotite minerals at Earth surface conditions, alteration effects associated with weathering and low-temperature metamorphism are common with extensive mantle exposures. As such, the Semail Ophiolite has also served as an important natural laboratory to study the chemical, physical, and biological effects of serpentinization and carbonation of mantle peridotite (e.g., Neal and Stanger, 1984; Stranger, 1985; Nasir et al., 2007; Kelemen and Matter, 2008; Kelemen et al., 2011; Streit et al., 2012; Pauckert et al., 2012; Miller et al., 2016).

Of particular interest are the mechanisms, timing, and rates of carbonation of peridotite and serpentinite minerals. Carbonate minerals can be formed directly from the breakdown of peridotite or serpentinite minerals in the presence of CO_2, which may be

sourced from seawater, magmatic vent fluids, the atmosphere or fluid percolation through carbonate rocks (e.g., Klein and Garrido, 2012 and refs therein). In addition to mineral replacement reactions, extensive veining can host a significant volume of carbonate within altered peridotite. These two styles of carbonate alteration in serpentinites are observed in a variety of tectonic settings, such as at mid-ocean ridges, along hyper-extended margins, and within continental ophiolite exposures (e.g., O'Neil and Barnes, 1971; Froitzheim and Rubatto, 1998; Schroeder et al., 2002), indicating that the process is a common reaction that has occurred throughout Earth's history. As such, the carbonation alteration of ultramafic rocks plays an important role in the global C-cycle, affecting CO_2 concentration in the atmosphere, and thereby impacting climate, ocean acidification, and C-recycling into the mantle (Kerrick and Connolly, 1998; Schuilling and de Boer, 2011; Scambelluri et al., 2016). In light of rising CO_2 concentrations in the modern atmosphere and oceans, the carbonation of peridotite has been explored as a mechanism for CO_2 sequestration, with the potential for long-term CO_2 storage in carbonate minerals and a limited risk of re-release (Lackner et al., 1995; Park et al., 2003; Kelemen and Matter, 2008; Kelemen et al., 2011; Power and Dipple, 2013).

Critical to understanding the mechanisms and reaction rates of carbonate alteration in peridotite are constraints on the timing and duration of carbonate mineralization in these systems. This can be challenging to determine on natural samples in the geologic record due to the lack of mineral phases accessible to dating by traditional geochronological techniques. In some cases carbonate minerals can be directly dated through the U-series decay system, but this technique is limited to systems younger than 100 ky (Callen et al., 1983; Edwards et al., 2003; Dorale et al., 2004). In more ancient samples U-Pb and Pb-Pb geochronology techniques have been applied to date carbonate minerals, but in some cases issues arise due to mobility of U and Pb in fluids, and carbonate recrystallization (e.g.,

Smith et al., 1991; Jahn and Cuvellier, 1994). An alternative approach to constraining the timing of carbonate mineral formation is to directly date secondary phases that form during carbonation.

In this study, magnetite (U-Th)/He is used to provide constraints on the history of carbonate altered ultramafic rocks at the Wadi Fins peridotite exposure in the Semail Ophiolite, Oman. Whereas magnetite commonly forms as an alteration mineral in serpentinites systems by secondary reactions at the expense of olivine and serpentine (e.g., Bach et al., 2006; Klein et al., 2013), at Wadi Fins magnetite grows exclusively within carbonate veins that cross cut and alter the serpentinized ultramafic rocks. The present study uses dates these magnetite crystals to determine whether carbonate vein formation occurred in the Cretaceous associated with ophiolite obduction, or more recently, and as proxy to determine the timescales of carbonation in this system.

Geologic background

The Semail Ophiolite developed in a supra-subduction zone setting between ~100-95 Ma in the Neo-Tethys Ocean and was subsequently obducted onto the Arabian margin in the Mid- to Late Cretaceous (Hacker, 1994; Searle and Cox, 1999, 2002; Jacobs et al., 2015). In the study area in SE Oman, early Maastrichtian subaerial erosion removed most of the igneous crustal sequence, as evidenced by erosional contacts and laterite deposits directly on the sub-oceanic mantle section (Nolan et al., 1990; Skelton et al., 1990). Transgression and subsidence resulted in submersion of the ophiolite and burial by ~ 2 km of shallow marine limestones during the late Maastrichtian to Miocene times (Robertson et al., 1990, Wyns et al., 1992). Continental collision of the Arabian and Eurasian plates in the Miocene caused folding and thrusting in the northern Oman Mountains and flexural uplift in the central Oman Mountains, leading to unroofing that exposed the peridotite once

again to subaerial conditions (Mann and Hanna, 1990; Robertson et al., 1990; McQuarrie and van Hinsbergen, 2013).

The mantle section at Wadi Fins is currently exposed in a water-carved canyon (*wadi*) in unconformable contact with the overlying limestone defined by a heavily altered contact zone and clastic dikes of carbonate into the peridotite (Fig 3.1). The peridotite section within the canyon is pervasively altered by carbonate veins and reaction zones between carbonate and serpentine, but the timing of carbonate alteration is not well constrained. At Wadi Fins, carbonate veining could have occurred during ophiolite

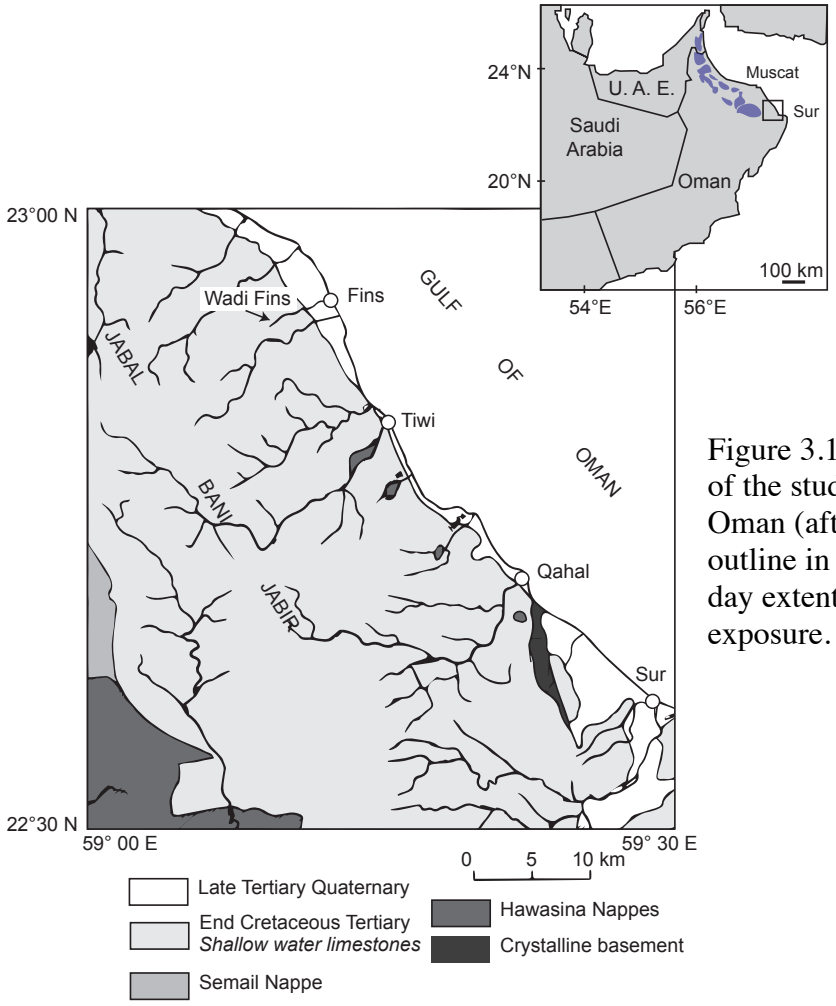

Figure 3.1: Simplified geologic map of the study area in southeastern Oman (after Wyns et al., 1992). Blue outline in upper inset shows present-day extent of ophiolite surface exposure.

obduction in the Cretaceous, during Early Maastrichtian subaerial erosion when the igneous crustal section was removed, at the onset of limestone deposition in the Late Maastrichtian, or more recently.

Sample description

The peridotite outcrops at Wadi Fins are variably serpentinized (50-100%) and cut by multiple generations of serpentine and carbonate (calcite) veins. Magnetite samples were retrieved from two sample locations within the canyon, one close to the contact with the limestone, and one ~ 1 km down canyon further away from the contact. The first sampling location, ~ 10 m below the limestone contact, displays unique dark green, light green, and red concentric zoning that reflect changing redox state, Fe-concentration, and degree of serpentinization (Fig. 3.2). The zoned blocks are 10's of cm across and bound on all sides by carbonate veins. Each block is composed of a dark green, partially serpentinized core (typically ~ 70%), surrounded by a fully serpentinized light green inner rim. These two zones are all enclosed by a red, highly oxidized outer rim (Fig. 3.2).

In contrast, at the second sample locality, 10's of meters below the limestone contact, the three-stage zonation is not visibly present. Instead, the outcrop is dominated by the dark green partially serpentinized peridotite typical of the green cores in the first outcrop, with only a narrow (< 10 cm) light green fully serpentinized reaction zone at the interface with carbonate veins (Fig. 3.2).

Observations from both outcrops indicate that carbonate veining post-dates much of the serpentinization. Extensive calcite veins are micrometers to several centimeters wide and laterally continuous from 0.5 to several meters, crosscutting the serpentinite in a "checkerboard" pattern on the canyon floor (Fig. 3.2). In some veins, angular mm- to cm-scale clasts of serpentinite are visible, providing evidence that the peridotite was at least

partially serpentinized prior to carbonate alteration. In several locations, carbonate veins are accompanied by a final, late-stage chrysotile veining.

Petrographic observations in thin section confirm a similar multi-stage alteration history observed in the outcrop. A simplified sequence of observed cross-cutting relationships common to all petrographic observations includes: 1) mesh texture serpentine after olivine (predominately lizardite), 2) very thin (< 10 μm) serpentine veins, 3-4) chrysotile veins (> 10 μm – mm) and thick carbonate veins (up to several cm). In some cases, multiple generations of carbonate veins are observed, but these always crosscut the mesh and micro-vein serpentine textures (1 and 2). The chrysotile serpentine veins are observed in the center of carbonate veins, suggesting that the formation of carbonate and chrysotile serpentine veins may be concurrent, and are the final alteration step.

Magnetite is notably absent from the serpentinites from both sampling localities. Instead, magnetite is observed as large crystals (mm – cm) in the center of carbonate veins, or as aggregates of small (μm) crystal trails near the edge of carbonate veins in contact with Fe-poor, light green altered serpentinite zones (Fig. 3.2, 3.3). These observations, as well as the presence of carbonate inclusions within magnetite crystals, support the interpretation that the magnetite grew concurrently with carbonate vein formation (Fig. 3.4).

A general reaction that can account for the carbonate, chrysotile serpentine and magnetite growth is at the expense of the Fe-rich serpentine and fluids from the overlying calcite limestone:

$$\text{Fe-serpentine} + \text{water} + CO_2 + CaO = \text{serpentine} + \text{calcite} + \text{magnetite} + H_2$$

$$3(Mg_2FeSi_2O_5(OH)_4) + 4H_2O + CO_2 + CaO = 3(Mg_2Si_2O_5(OH)_4) + CaCO_3 + Fe_3O_4 + 4H_2$$

The magnetite collected from the two sample locations are shown in Fig. 3.5. One magnetite sample (15OM21) was recovered from the zoned outcrop near the limestone contact. Magnetite is less abundant in this highly-oxidized section of the canyon, and most Fe-rich opaque minerals are hematite and goethite. Additional magnetite crystals (15OM25B, 15OM24bg, 15OM24g2) were plucked from carbonate veins down-canyon away from the contact, where the extreme red-green zonation is absent. Other samples from the same locations were screened for magnetite He dating, but could not be analyzed due to small magnetite grain size ($< 60\ \mu$m), or an abundance of carbonate inclusions (Fig. 3.4).

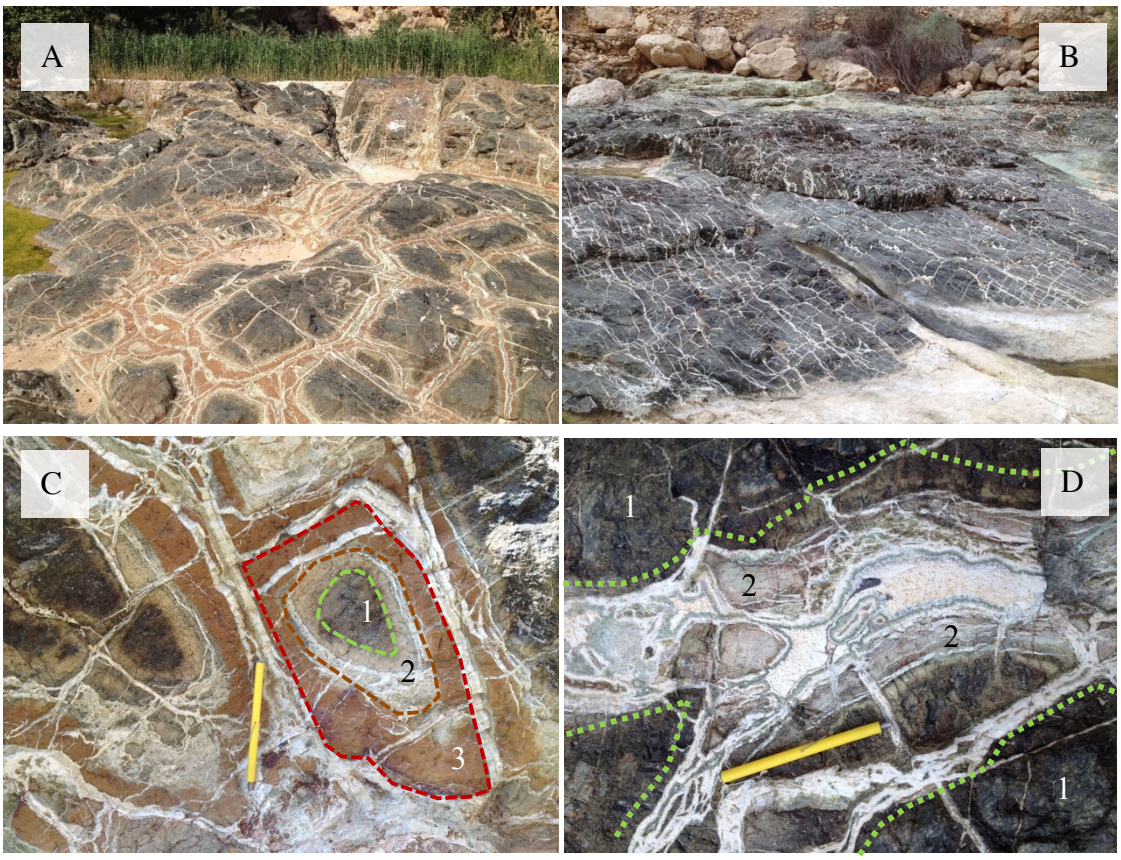

Figure 3.2: Wadi Fins outcrop photographs with reaction zones. A) Upper-canyon serpentinite outcrop with extensive concentric zoning reflects changing Fe-concentration and oxygen fugacity. B) Lower-canyon serpentinite outcrops do not display the same degree of zonation. C) Close-up on the upper outcrop, three zones are identified 1) Fe-rich cores, 2) Fe-poor inner green rim, and 3) Fe-rich outer red rim. D) Close-up on the lower outcrop, alteration equivalent to the Fe-poor green inner rims are evidence for Fe-mobility at the boundary with carbonate.

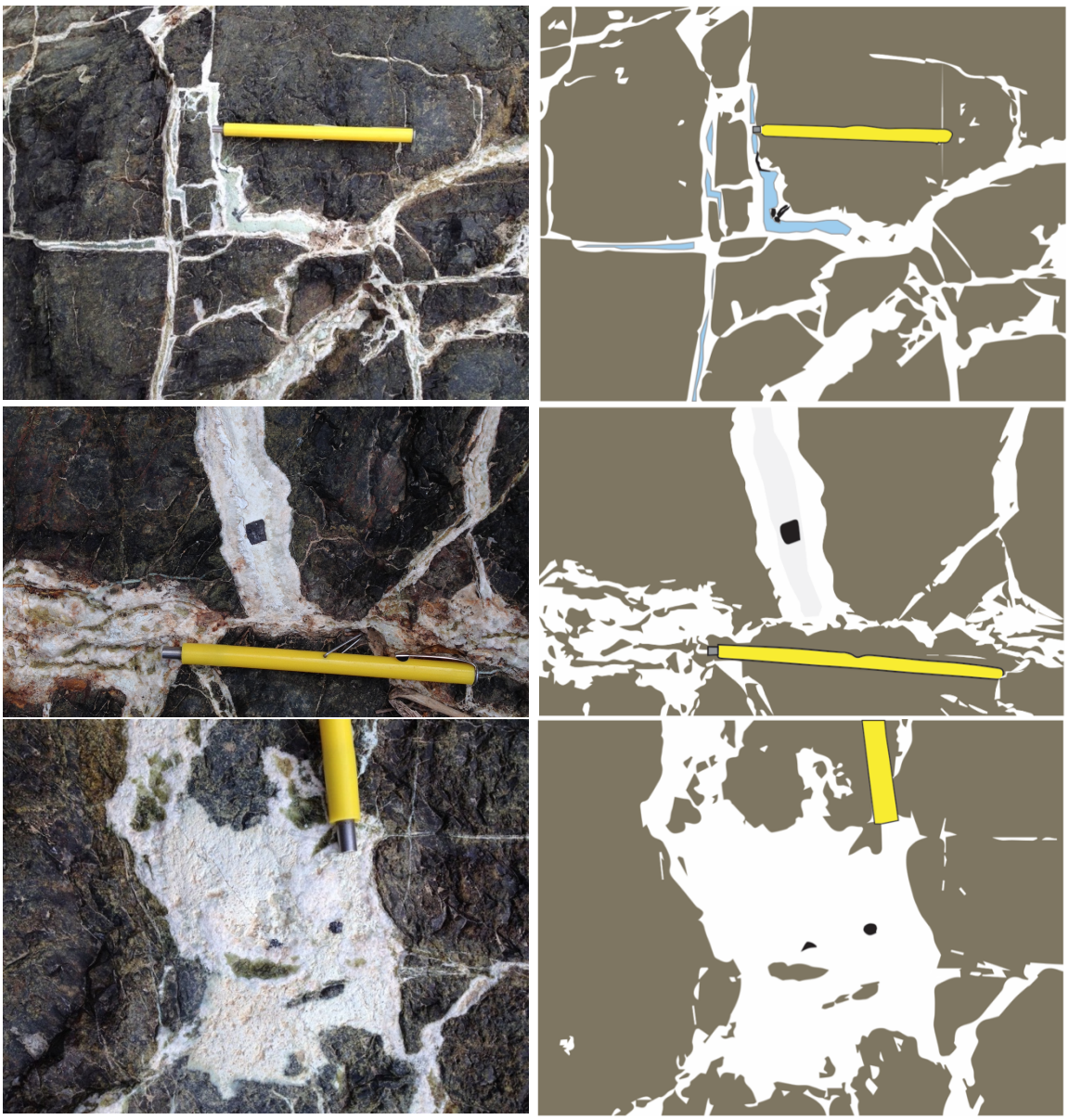

Figure 3.3: Wadi Fins outcrop photos with magnetite (black minerals). In all serpentinite outcrops on the canyon, magnetite grows exclusively in carbonate veins with grain sizes that range from $< 100\ \mu$m to > 1 cm.

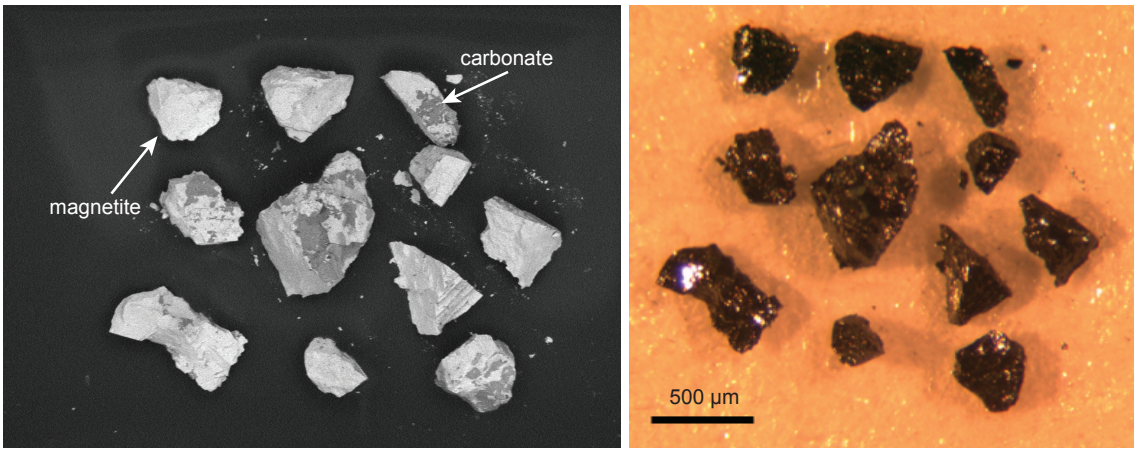

Figure 3.4: Carbonate inclusions detected in magnetite grains. (Left): Backscatter electron image of magnetite fragments. Energy dispersive spectroscopy (EDS) confirmed that the bright zones are magnetite and dark grey zones are carbonate. (Right): The same fragments photographed with overhead lighting on an optical microscope. The carbonate intergrowths are not visible by optical microscopy, but may be detected by μCT or SEM.

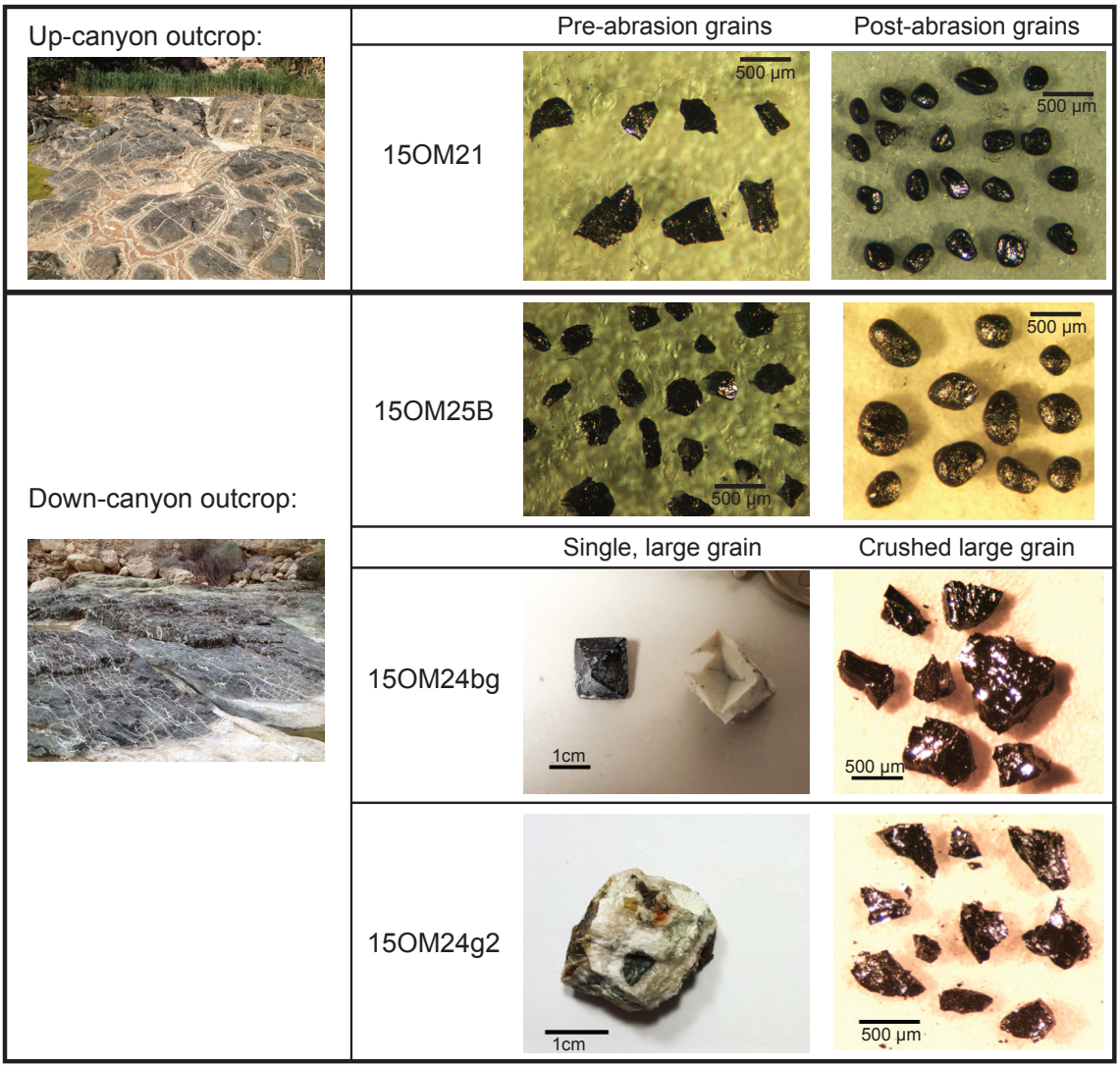

Figure 3.5: Wadi Fins magnetite from four samples. Representative photos of grains from each sample are shown below. The upper-canyon, highly zoned area had only one recoverable magnetite sample (15OM21), while the down-canyon outcrop had several (15OM25B, 15OM24bg, 15OM24g2). Two samples had small enough grains to abrade prior to He analyses (15OM21 and 15OM25B). The other two samples constituted single large grains that were crushed and internal fragments were used for He analysis.

Methods

Sample preparation

Magnetite grains were separated from carbonate vein material with mortar and pestle and subsequently removed by hand magnet. Samples consisting of mm- to cm-size euhedral grains were crushed with mortar and pestle to fragments that measured several 100 μm in diameter. Crushed and separated smaller grains (< mm) were generally anhedral, which is consistent with outcrop observations. Prior to (U-Th)/He analysis, magnetite grains were subjected to a multi-step screening and preparation process that included 1) X-Ray Computed Tomography scanning, 2) the removal of the outer grain boundary, and 3) determination of major element chemistry. The reason for each of these steps and the procedures will be discussed below.

Separated grains and fragments were picked using an optical microscope and loaded onto double-sided sticky tape mounted on thumbtacks for scanning with High-Resolution X-Ray Computed Tomography (CT) at The University of Texas at Austin's NSF-Multi User Facility (Appendix 3). The X-Ray CT procedure is a critical step to reveal the presence of inclusions or internal fractures that can complicate the He diffusion systematics and lead to erroneous He age results. All analyzed grains were CT scanned at a 3-5-μm resolution, and only grains without discernable inclusions or fractures were used for (U-Th)/He dating.

Due to low parent nuclide concentrations, magnetite is highly susceptible to U, Th or Sm contamination from attached matrix material or excess He due to implantation from neighboring phases (Blackburn et al., 2007; Taylor, 2012). Since He atoms can travel ~ 16 μm in magnetite during alpha decay, this requires the physical removal of the outer ~ 20 μm of the magnetite grain before He analysis (e.g., Farley et al., 1996; Blackburn et al., 2007; Ketcham et al., 2012; Cooperdock and Stockli, 2016). Two grain preparation

procedures were employed to remove the outer grain boundary. Large, mm- or cm-sized single grains (15OM24g2, 15OM24bg) were crushed with a mortar and pestle and internal fragments were selected under optical microscope. Fragments were determined to be internal based on shiny luster, visually fractured surfaces and the lack of visible grain boundaries or attached matrix. Grains less than mm-size (15OM21, 15OM25B) were physically air abraded at 6 psi for ~ 4 hours following Blackburn et al. (2007) and Cooperdock and Stockli (2016) (Fig. 3.5).

Cooperdock and Stockli (2016) demonstrated that magnetite trace elements can be a useful complement to (U-Th)/He dating to distinguish between multiple growth episodes, as magnetite can incorporate significant amounts of minor elements (Nadoll et al., 2012). For this purpose, semi-quantitative compositional data was collected on the same magnetite grains and fragments to be analyzed for (U-Th)/He using a Philips/FEI XL30 Environmental Scanning Electron Microscope (ESEM) with an X-ray energy dispersive spectroscopy (EDS) attachment at The University of Texas at Austin. Major element compositional data (≥ 1 wt.%) was then used to combine grains or fragments of similar composition into multi-grain or multi-fragment aliquots.

(U-Th)/He measurements

(U-Th)/He analyses were completed at the UTChron facility at The University of Texas at Austin. Individual aliquots consisted of 1–8 abraded grains, or internal fragments from a single grain, loaded into platinum packets for He degassing. Only grains of similar size and composition were combined into single aliquots. ^{4}He concentrations were measured using a Thermo HelixSFT™ magnetic sector noble gas mass spectrometer. Individual aliquots were heated with a DiodeLaser using a pyrometer calibrated to a temperature of ~900°C. Blanks were run between each unknown to monitor and quantify

the procedural He blank during the analytical run. Aliquots were reheated until ^{4}He gas yields dropped < 1% total gas, or < 2x procedural blank concentrations. Total ^{4}He concentrations (ncc) were blank-corrected and determined against a manometrically calibrated ^{4}He standard of known concentration.

After degassing, magnetite grains and fragments were unpacked from the platinum packets and dissolved in Savillex vials on a hot plate following a two-step HF-HNO_3 and HCl dissolution technique (Appendix 1). Samples were spiked with a ^{235}U, ^{230}Th, and ^{149}Sm tracer in 5% HNO_3, and dissolved using a 5:1 concentrated HF - 7N HNO_3 mixture heated at ~180°C for 12 hours. Samples were dried down to a small bead and 200 μl of concentrated HCl was added to the vial and heated for 12 hours at 180°C. After chloride conversion, the solution was dried down to a small bead and 100 μl of 7N HNO_3 and 500 μl of MilliQ H_2O were added before analysis on the Thermo Element2 HR-ICP-MS. Final U-Th-Sm concentrations were calculated using isotope dilution with a mixed spike calibrated against a 1 ppb U-Th-Sm gravimetric standard solution.

Final (U-Th)/He ages were calculated using blank corrected U, Th, Sm and He measurements by iteratively solving the age equation. The reported analytical error for the (U-Th)/He age was calculated using the maximum and minimum He age based on the analytical error of individual U, Th, Sm and He measurements. Typically, U, Th, and Sm measurement errors were all < 2 %, whereas analytical ^{4}He errors ranged from < 1% up to 8 % depending on ^{4}He concentration and the magnitude and variation of blanks over the analysis time. Mean calculated ages are reported with a two-standard error.

Results

ESEM-EDS semi-quantitative compositional analyses on magnetite grains and fragments confirm that all samples contain Fe and O concentrations consistent with

magnetite (65-75% Fe, 25-35% O). No other major cations were detected above the 1 wt.% detection limit, with the exception of one magnetite sample (15OM21) taken from the highly-oxidized zone near the carbonate contact that contained 1-2 wt.% Si (Table 3.1).

Magnetite (U-Th)/He results exhibit a similar age range for the different samples regardless of grain size or chemistry. Nine aliquots, each composed of 1-5 abraded magnetite grains from 15OM21, produce ages that range from 4.6 ± 0.3 to 21.4 ± 1.4 Ma, with a median age of 12.1 ± 0.5 Ma and a mean age of 13.9 ± 4.0 Ma (2SE). These aliquots consisted of average grain sizes from 182 to 885 μm, with no clear variation with age. Typical U concentrations were lowest in this sample (3-30 ppb). Th and Sm concentrations, similarly, ranged from 1 to 40 ppb.

Nine aliquots from 15OM25B, each composed of 1-8 grains, have an age range from 9.7 ± 0.2 Ma to 25.8 ± 1.3 Ma, with one aliquot resulting in 131.2 ± 6.4 Ma. This older aliquot contained an order of magnitude higher concentration of ^{4}He (pmol/g) compared to other aliquots within the sample (Table 3.1), likely the result of excess He (implanted or inherited). Excluding this outlier, 15OM25B has a median magnetite He age of 15.0 ± 0.2 and a mean age of 17.8 ± 4.4 Ma (2SE). Average aliquot grain sizes ranged from 138 to 659 μm, and have no correlation with age. Magnetite U concentrations in this sample range from 30 to 60 ppb, with Th and Sm concentrations of 1 to 30 ppb.

Five aliquots composed of 1 to 4 internal fragments from a single cm-size grain (15OM24bg) produce He ages ranging from 4.1 ± 0.3 Ma to 27.2 ± 1.1 Ma, with a median age of 9.9 ± 0.4 and a mean age of 12.0 ± 8.0 Ma (2SE). Internal fragments ranged from 228 to 912 μm for the different aliquots. One aliquot, which produced the 4.1 ± 0.3 Ma age, has high U and Th concentrations (> 100 ppb), inconsistent with all other aliquots (~30 ppb). This may point to excess U and Th introduced through contamination for this analysis, or indicate internal sample heterogeneity not captured in other analyses.

Table 3.1: Wadi Fins magnetite (U-Th)/He age data

Sample	Age (Ma)	U (ppb)	Th (ppb)	Sm (ppb)	Th/U	^{4}He (pmol/g)	Si in magnetite	# of grains / fragments	Avg. ESD grain / fragment (µm)
Multi-grain aliquots of individually abraded grains									
Upper canyon outcrop near the limestone contact									
mg15OM21ab-1	9.0 ± 0.6	16	6	19	0.37	0.8		5	221
mg15OM21ab-2	9.1 ± 0.5	9	4	7	0.46	0.5	x	3	330
mg15OM21ab-3	12.1 ± 0.5	7	1	6	0.19	0.5	x	1	516
mg15OM21ab-4	19.1 ± 0.6	3	1	1	0.26	0.3	x	1	885
mg15OM21ab-5	21.4 ± 1.4	3	2	7	0.68	0.5	x	1	480
mg15OM21ab-6	10.9 ± 2.4	5	5	42	0.98	0.4	x	5	182
mg15OM21ab-7	20.3 ± 1.1	30	15	29	0.51	3.7	x	2	207
mg15OM21ab-8	4.6 ± 0.3	19	7	16	0.38	0.5	x	4	273
mg15OM21ab-9	18.3 ± 1.2	4	1	9	0.32	0.4	x	1	488
Mean: 13.9 Ma ± 4.0 (2SE), Median: 12.1 Ma									
Lower canyon outcrop away from the limestone contact									
mg15OM25Bab-1	15.0 ± 0.2	23	1	3	0.05	2.0		1	659
mg15OM25Bab-2	24.1 ± 0.7	23	4	7	0.19	3.1		1	419
mg15OM25Bab-3	15.1 ± 0.5	27	2	5	0.09	2.2		3	329
mg15OM25Bab-4	24.9 ± 0.8	27	5	9	0.19	3.8		3	272
mg15OM25Bab-5	9.7 ± 0.2	67	15	13	0.22	3.7		4	216
mg15OM25Bab-6	*131.2* ± 6.4	21	10	33	0.48	*16.9*		6	138
mg15OM25Bab-7	25.8 ± 1.3	22	6	12	0.26	3.3		6	196
mg15OM25Bab-8	14.0 ± 0.5	56	2	9	0.04	4.3		6	210
mg15OM25Bab-9	13.5 ± 0.4	62	7	14	0.12	4.7		8	168
Mean: 17.8 Ma ± 4.4 (2SE), Median: 15.0 Ma									
Internal fragments from a single grain									
mg15OM24bg-1	11.5 ± 0.1	27	2	3	0.08	1.7		1	912
mg15OM24bg-2	9.9 ± 0.4	39	25	8	0.64	2.4		2	393
mg15OM24bg-3	4.1 ± 0.3	123	102	66	0.83	3.3		4	228
mg15OM24bg-4	27.2 ± 1.1	22	3	2	0.15	3.3		3	355
mg15OM24bg-5	7.4 ± 0.4	30	6	5	0.19	1.3		2	422
Mean: 12.0 Ma ± 8.0 (2SE), Median: 9.9 Ma									
mg15OM24g2-1	15.7 ± 0.4	16	1	3	0.08	1.4		1	629
mg15OM24g2-2	13.8 ± 0.8	20	7	5	0.35	1.6		1	540
mg15OM24g2-3	12.9 ± 0.6	27	6	5	0.21	2.0		2	376
mg15OM24g2-4	12.6 ± 1.3	29	8	11	0.29	2.1		2	287
Mean: 13.8 Ma ± 1.4 (2SE), Median: 13.4 Ma									

Four aliquots composed of 1 or 2 internal fragments from a mm-size grain (15OM24g2) yield ages from 12.6 ± 1.3 Ma to 15.7 ± 0.4 Ma, with a median age of 13.4 ± 0.8 Ma, and a mean age of 13.8 ± 1.4 Ma (2SE). Internal fragments used for analysis ranged from 287 to 629 μm, and show no trend with age. Similar to the other samples, U concentrations varied from 16-30 ppb, while Th and Sm were in lower concentration (1-11 ppb).

U, Th, and Sm concentrations are sub-ppm for aliquots across all samples. 15OM21, the Si-bearing magnetite, has consistently lower U concentrations (3-30 ppb) compared to the other samples (16-123 ppb). Th/U and Sm/U ratios for all samples are all <1, such that U is the dominant contributor for radiogenic ^{4}He production in the magnetite. Magnetite He age results display a negative trend with U concentration in each sample, such that younger aliquots consistently have higher U concentration. This observation holds for individually abraded grains and internal fragments of large grains.

Interpretation

Fe-mobility and magnetite formation in carbonate veins

The first piece of geologic evidence that brackets the timing of carbonate alteration at Wadi Fins is based on the relationship between the carbonate veins in the serpentinized peridotite and the overlying limestone unit. Geochemical and petrological evidence indicate that the carbonate veins within the serpentinite are almost certainly sourced from the overlying limestone. First, calcite is the dominant carbonate mineral in Wadi Fins carbonate veins, in contrast to other ophicarbonate localities in Oman where Mg-carbonates (magnesite or dolomite) are most common (e.g., Kelemen et al., 2011; Streit et al., 2012). Secondly, the carbonate vein ^{87}Sr/^{86}Sr isotope and REE compositions closely mimic the overlying limestone (Schluter et al., 2008; de Obeso and Kelemen, in prep),

indicating an inherited geochemical signature. This suggests that carbonate veining in the mantle rocks likely occurred during or after limestone deposition.

Magnetite formation in these veins can be traced to Fe-mobility associated with alteration of the serpentinite. Extensive major element redistribution during fluid alteration of the serpentinite is evidenced by bulk rock and microprobe elemental analyses (de Obeso and Kelemen, in prep). Specifically, Fe-mobility is traced in the zoned serpentinite near the limestone contact by changes in FeO concentration from the less altered dark green cores (~10 wt% FeO), to the light green inner rims (~7 wt%. FeO), to the red outer rims (up to 14 wt% FeO) (de Obeso and Kelemen, in prep). This observation is supported by changing Fe-bearing mineralogy from Fe-rich serpentine in the core to goethite and hematite in the red rim—consistent with an increasing water-rock ratio and a dramatic increase in fO_2 on short length scales (~15 cm; de Obeso and Kelemen, in prep). These observations can be extrapolated to the less zoned, lower-canyon outcrops further from the limestone contact. Here Fe-mobility at the expense of the dark green serpentinite is evidence by Fe-leached light green cm-thick reaction rims at the contact with carbonate veins. Notably, the calcite veins throughout Wadi Fins have consistently low FeO concentrations (≤ 0.1 wt.% based on microprobe data; de Obeso and Kelemen, in prep), indicating that the carbonate is not a host for mobilized Fe. These observations support the interpretation that magnetite may have formed from Fe leached out of the serpentinite during carbonate vein formation, and thereby dating the magnetite can provide a first order estimate for the timing of carbonate veining.

Timing and duration of magnetite growth

The timing of Fe-mobility and carbonate veining at Wadi Fins is not known. An upper age limit for the initiation of carbonate alteration at Wadi Fins is Maastrichtian (~75-

66 Ma), the age associated with the onset of limestone deposition. However, as will be discussed in this section, clumped isotope thermometry suggests that veining in the peridotite occurred at the end of limestone deposition, which ceased in the Miocene (Wyns et al., 1992; de Obseo and Kelemen, in prep). Given that field and petrographic observations strongly support that magnetite grew with carbonate vein formation, this study employs magnetite growth as a proxy for the timing and duration carbonate alteration.

The ability for magnetite (U-Th)/He to provide formation rather than cooling age constraints is dependent upon the thermal history of the sample. Given the published He diffusion kinetics for magnetite, the (U-Th)/He age will record the timing of magnetite growth for temperature conditions < 250°C (assuming a 10°C/my cooling rate; Blackburn et al., 2007). This constraint can be coupled with previous work on the thermal history for the serpentinites at Wadi Fins to assess whether magnetite He should record formation or cooling. Broadly, apatite and zircon fission track studies across Oman and the U.A.E. produce cooling ages of ~ 40 - 70 Ma, indicating regional cooling to temperatures < 120°C by the late Eocene (Saddiqi et al., 2006; Gunnell et al., 2007).

Locally, the thermal history of Wadi Fins is constrained by geologic observations and isotopic data. First, the complete lack of an igneous crustal section, which is remarkably preserved in other localities in Oman, indicates that the mantle section of this region of the Semail Ophiolite was cooled to surface conditions, and experienced extensive subaerial erosion in the Cretaceous (e.g., Al-Khirbash, 2015). This was followed by ~2 km of limestone deposition over a 50 My period (Wyns et al., 1992; Schuler et al., 2008), which would have reheated the serpentinite to ~60°C assuming an estimated regional geothermal gradient of 30°C/km (Saddiqi et al., 2006; Gunnell et al., 2007). This burial temperature is precisely in agreement with clumped isotope measurements on the carbonate

veins within the serpentinite at Wadi Fins, which record maximum formation temperatures of 60°C (de Obeso and Kelemen, in prep). This indicates that carbonate veining may have occurred in the serpentinite once the bulk of the limestone section was deposited. There is no evidence for significant heating during more recent uplift, and erosion. Therefore, magnetite formation likely occurred as low as <100°C, well below the magnetite He closure temperature.

The oldest magnetite He ages from three of the samples record formation ages as early as the Oligocene-Miocene boundary, consistent with carbonate alteration commencing at the end of limestone deposition (Fig. 3.6). This is supports the notion that magnetite mineralization was coeval with carbonate veining, and may provide a direct time constraint for the onset of carbonate vein formation. Furthermore, the spread in magnetite He ages may suggest protracted growth throughout the Miocene (Fig. 3.6). When all samples are considered together, systematic trends in the range of He ages emerge. First, the full range of He ages is reproduced between multiple samples, with maximum ages of ~ 25 Ma and minimum ages of ~ 4 Ma. The results from internal fragments of the largest grain produce ages that encapsulate the entire growth period recorded by the other samples, which may imply protracted growth over a 23 my period. The remaining sample results from single abraded grains (< 1 mm), and internal fragments of a mm-sized grain, are all contained within this time window, supporting either protracted or episodic growth over this interval. In this scenario, magnetite growth would have commenced in the beginning of the Miocene, concurrent with the end of carbonate deposition, and the beginning of uplift in southeastern Oman. Magnetite formation, and by proxy carbonation and Fe-mobility, continued throughout the Miocene for ~ 20 My and culminated at ~ 4 Ma (Fig. 3.7).

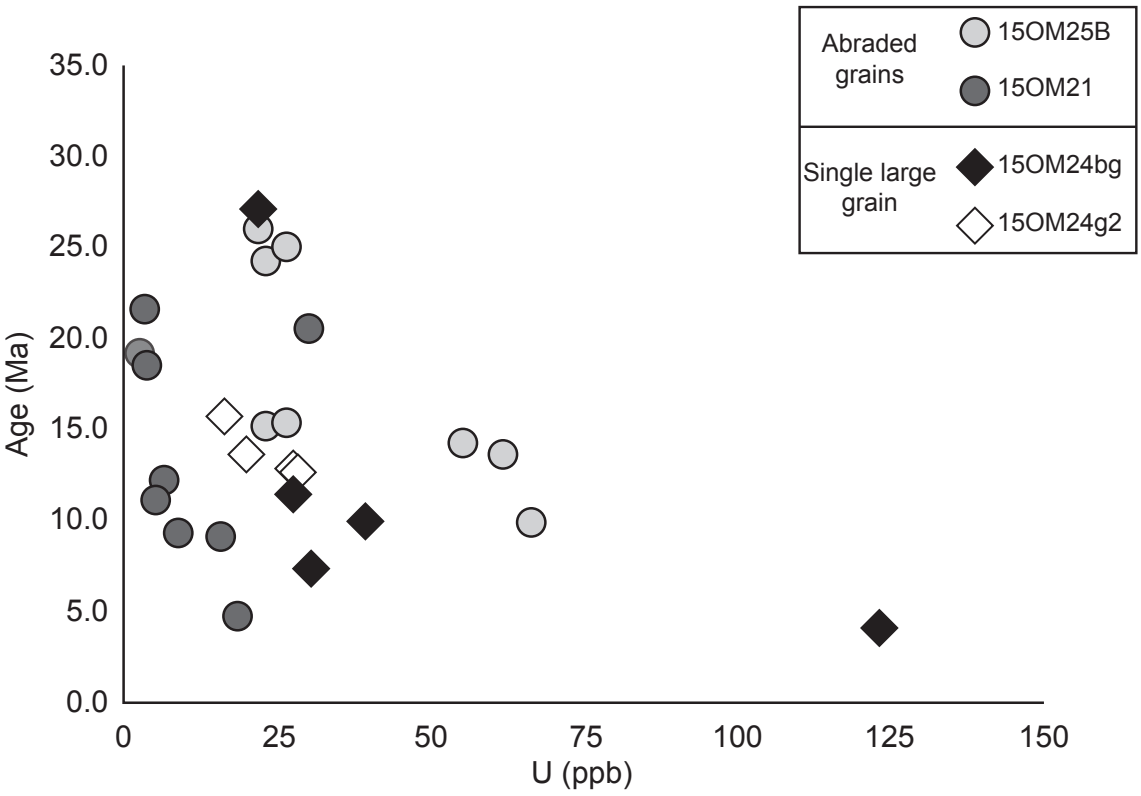

Figure 3.6: Magnetite (U-Th)/He ages from all samples are plotted versus uranium concentration. Aliquots composed of abraded grains (circles) are distinguished from aliquots composed of internal fragments (diamonds) from a single large grain. All samples, regardless of grain size, produce a similar range in He ages, and younger aliquots have higher U concentrations. The oldest magnetite record the onset of growth in the latest Oligocene – early Miocene.

Alternatively, the duration of magnetite growth may be shorter if the concentration of U in the youngest samples (4 Ma) were a result of U contamination. In this case, He ages would appear erroneously young without affecting He concentrations. Plotting He vs. U concentration shows that He increases with effective uranium concentration in most analyses, with the possible exception of one 4 Ma analysis that has similar He concentration to other aliquots and significantly more U (>100 ppb) (Fig. 3.7). If the youngest ages (4

Ma) are unreliable, then the duration of magnetite growth recorded across multiple samples would reduce to ~15 my, from ~ 25 – 10 Ma.

In any case, this age range and increase in U concentration in younger magnetite is reproduced across multiple samples and multiple analytical runs, providing evidence that the increased U concentration through time may be geologically significant. This change in U concentration could indicate changing fluid composition during magnetite growth toward more oxidizing conditions, as the oxidized form U^{6+} is fluid mobile.

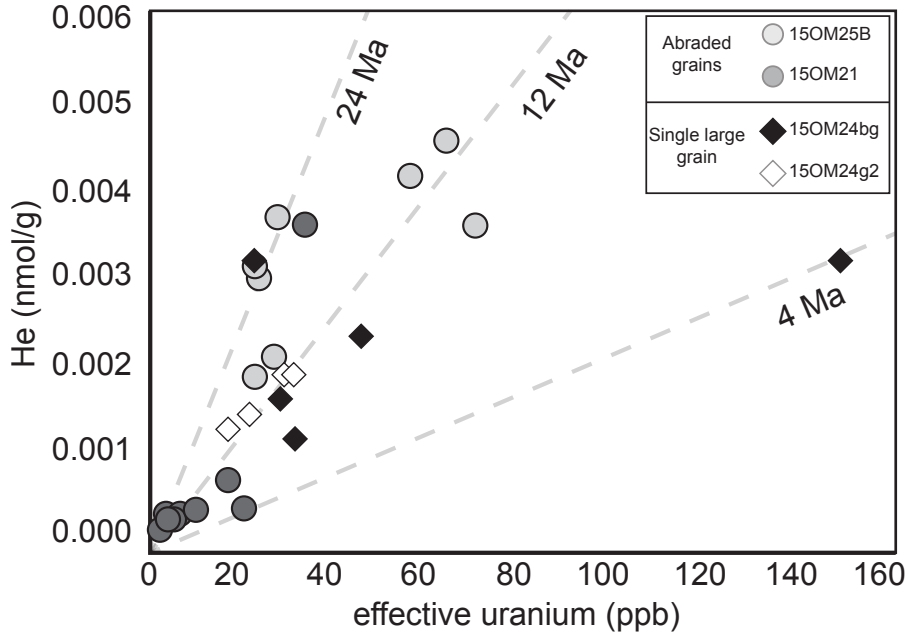

Figure 3.7: Magnetite He concentrations plotted against effective uranium. All samples show a trend in age with U concentration, with youngest aliquots having 2-4x more U than the oldest aliquot. The [He] vs [U] concentration graph demonstrates that the increase in U is compensated by an increase in He, as would be expected.

Comparison to carbonation rates in other Oman peridotites

The extended duration of carbonate veining at Wadi Fins implied by magnetite growth is much longer than estimated carbonation and veining rates from studies on

peridotite samples from other locations in the Semail Ophiolite, Oman. Specifically, Kelemen and Matter (2008) report ^{14}C ages for peridotite hosted travertine and carbonate veins that are < 50,000 years old, with an average age of ~26,000 years. They use their results to infer that these modern veins form mainly as a thin weathering horizon in these samples, which keeps pace with erosion (~ 0.3 mm/yr; Poupeau et al., 2003). Pauckert et al., (2012) model timescales as short as 6,500 years to reach steady-state fluid compositions consistent with natural carbonating springs in Oman. Older carbonated peridotite exists as ^{14}C-dead veins exposed in road cuts (>50,000 BPE) and as lisvanites, which are fully carbonated peridotite along the basal thrust of the ophiolite interpreted to form coincident with ophiolite obduction in the Cretaceous (Mervine et al., 2014; Streit and Kelemen, 2012; Falk and Kelemen, 2016). The Wadi Fins carbonate veins appear to represent a different category of serpentinite hosted carbonate veins, not associated with recent travertine deposits, and not associated with ophiolite obduction.

Several factors, including temperature, fluid availability, fracturing potential and mineral-specific reaction rates may contribute to the extended duration of carbonate alteration at Wadi Fins. First, the low alteration temperature at Wadi Fins certainly has the effect of slowing down reaction rates, but this is unlikely to explain the long carbonation duration because the temperature is not significantly different from other carbonated peridotites in Oman, which range from 30°C surface temperatures in active springs to ≤ 200°C for lisvanites (Kelemen and Matter, 2008; Kelemen et al., 2011; Falk and Kelemen, 2015).

Second, Wadi Fins peridotite surface exposures are limited to the bottom of a narrow canyon, with a thick sequence of carbonate limiting direct access of fluids. Presumably, prior to subaerial erosion and wadi formation, fluids had to percolate through the limestone sequence to reach the serpentinite. This is in contrast to active springs and

other veined peridotite localities in Oman, which have extensive surface exposures available for weathering.

Third, fluids must have space to penetrate the rocks for veining to occur. Volume expansion during serpentinization and carbonation can increase rock volumes by 30-40%, essentially choking out fluids (Kelemen et al., 2011). Therefore, there must be some fracturing mechanism, whether reaction-driven cracking or tectonic fracturing to allow fluids to reach unreacted minerals surfaces (e.g., Rudge et al., 2010; Kelemen and Hirth, 2012). Specifically in Oman, carbonate veins commonly occur in perpendicular vein sets, which Kelemen et al. (2011) interpret as evidence for reaction-driven cracking associated with volume expansion in a diffusive reaction zone parallel to the weathering surface, and not fracturing due to tectonic compression or extension. At Wadi Fins a similar right-angle vein orientation is observed; however, tectonic forcing cannot be completely ruled out as the timing of veining corresponds with changing regional tectonic stresses.

Finally, a fourth confounding factor is mineral reaction rates, as serpentine carbonation is more than 10 times slower than olivine carbonation under similar temperatures and fluid compositions (O'Connor et al., 2004; Gerdemann et al., 2007). Although much of the carbonate in Wadi Fins appears to form from dissolution of the overlying limestone and less so from direct peridotite carbonation reactions, there is evidence that the source of Fe for magnetite growth derives from interactions with the serpentinite. At Wadi Fins the peridotite was already 50-70% serpentinized prior to carbonation, as evidenced by cross cutting relationships. This, along with major element mobility and new serpentine formation suggests that carbonation occurred at the expense of serpentine, not olivine, which may explain the significantly slower rates carbonation at Wadi Fins.

Overall, these results provide evidence for Fe-mobility and carbonate vein formation commencing in the latest Oligocene–early Miocene, and continuing through the end of the Miocene, over a 20 my period. From a tectonic perspective, this is relates to the onset of regional uplift, which brought the carbonate platform and serpentinized mantle to subaerial conditions (e.g., Mann, 1990). Regional uplift may have also provided a means to fracture the rock and to aid fluid infiltration and vein formation through 2 km of limestone to the underlying serpentinite. Low temperature alteration, indirect fluid access, and slow carbonation reaction rates for serpentine could have all contributed to this extended period of carbonation. Importantly, these results indicate that carbonate alteration in this part of the ophiolite is not associated with obduction or subaerial erosion in the Cretaceous, and is not recent (< 50 ky), as in other localities in Oman.

Conclusions

At Wadi Fins, Oman, serpentinized peridotite from the base of the Semail Ophiolite exhibits extensive carbonate alteration. To determine the timing and duration of carbonate alteration, magnetite crystals that grew coincident with carbonate veining were dated with (U-Th)/He chronometry. SEM-EDS measurements found that magnetite from one sample (in a highly-oxidized zone near the limestone contact), contains significant Si impurities. Magnetite (U-Th)/He age results spanned from 27 Ma to 4 Ma, indicating that magnetite growth (and carbonate alteration) began in the late-Oligocene/early-Miocene. This is consistent with carbonate alteration commencing at the end of limestone deposition, and the onset of regional uplift. Magnetite formation continued through the Miocene, with increasing U concentrations recorded in the magnetite possibly indicating the evolution of fluids toward more oxidizing conditions. These results are unique compared to other peridotite and serpentinite carbonation and veining systems in Oman, as they provide

evidence for carbonate alteration on the order of 10's of millions of years, and are not related to ophiolite obduction or Quaternary spring activity. This setting may serve as an end-member for carbonate altered peridotite in Oman and be an appropriate analogue for other serpentinite systems covered with thick limestone sequences in Oman and in modern seafloor environments.

Chapter 4: Dating exhumed peridotite with spinel (U-Th)/He chronometry

Abstract

The low-temperature cooling history of exhumed mantle peridotite in oceanic and continental settings has been challenging to determine by geologic relationships or traditional thermochronology techniques. As a result, the timing of mantle exhumation at mid-ocean ridges, rifted and passive continental margins, and within orogenic systems has remained largely elusive or only loosely constrained by relative age brackets. Magmatic spinel [$(Mg,Fe)(Al,Cr)_2O_4$] is a ubiquitous primary mineral phase in mantle peridotites and is often the only remaining primary phase after surface weathering and serpentinization. This work explores spinel (U-Th)/He thermochronology as a novel tool to directly date the exhumation and cooling history of spinel-bearing mantle peridotite. Samples were chosen for a range of tectonic and petrologic systems, including a mid-ocean ridge abyssal peridotite (IODP Leg 209), an orogenic tectonic sliver of continental mantle (Lherz massif, France), and an erupted mantle xenolith (Green Knobs, NM). These case studies yield spinel He age results that are reproducible and generally in good agreement with independent age constraints. For IODP Leg 209, a spinel He age of 1.1 ± 0.3 Ma (2SE) (n=8) is consistent with independent U-Pb and magnetic anomaly ages for the exhumation of oceanic crust by detachment faulting along this segment of slow-spreading ridge. Spinel He ages from the Lherz massif produce ages of 61-99 Ma, which correspond well with independent thermochronometric constraints for cooling associated with contractional exhumation in the Northern Pyrenean Zone. Spinel from a mantle xenolith within a kimberlite diatreme at Green Knobs, NM generate a reproducible mean He age of 11.7 ± 1.8 Ma (2SE) (n=6), although it is younger than regional ~28-23 Ma K-Ar ages for the timing of volcanic emplacement in neighboring localities. Taken together, the results of

these case studies provide the first empirical evidence for the viability of spinel as a thermochronometer that may be used to resolve previously inaccessible ages and cooling histories of peridotite exhumed through tectonic and volcanic processes.

Introduction

Spinel-bearing peridotite lithologies constitute over 70% of mantle exposures on the earth's surface (Dick et al., 1984), and have been recovered in oceanic settings (amagmatic or slow spreading ridges, tectonic windows, passive margins, subduction zones), and on continents (massifs, orogenic belts, ophiolites, volcanic xenoliths). The presence of these rocks on the Earth's surface requires exhumation through volcanic or tectonic processes at some point in time. Historically, however, the timing of mantle exhumation in these settings has been a challenge to constrain due to obscured field relationships, extensive alteration of primary minerals by weathering at the earth's surface and low radiogenic nuclide concentrations in peridotite phases or high closure temperatures for applicable dating systems. As a result, the timing of mantle exhumation to shallow crustal levels has been relatively unconstrained, or loosely estimated by cross cutting relationships. The present work tests the viability of spinel [$(Mg,Fe)(Al,Cr)_2O_4$], a common primary magmatic mineral in peridotites, to serve as a thermochronometer to directly determine the timing of mantle exhumation through upper crustal levels by employing (U-Th)/He chronometry.

(U-Th)/He chronometry is a widely-applied technique used to resolve the time-temperature history of surface processes such as faulting, erosion, and hydrothermal circulation. The technique measures the radioactive production and retention of ^{4}He during the alpha decay of long-lived isotopes ^{238}U, ^{235}U, ^{232}Th, and ^{147}Sm in whole mineral grains. Requisite for successful He dating, a mineral must have measurable U, Th and Sm, no

inherited ^{4}He at the time of formation, and must quantitatively retain He in its crystal structure over geologic timescales. Since He can be lost through thermally activated diffusion, a (U-Th)/He age may represent either mineral crystallization or cooling, contingent on the thermal history of the sample. Conventionally used to constrain low-temperature cooling ages of crustal rocks, apatite and zircon are the most common minerals used for this technique with closure temperatures < 200°C (e.g., Zeitler et al., 1987; Reiners et al., 2005). Fe-oxide minerals, such as magnetite, hematite, and goethite, have also been successfully dated by (U-Th)/He and typically have closure temperatures from ~200°C to 300°C (Shuster et al., 2005; Blackburn et al., 2007; Farley and Flowers, 2012; Ault et al., 2015; Cooperdock and Stockli, 2016).

Magmatic spinel, targeted in this study, is an attractive mineral to date with He thermochronology because it tends to exhibit large grain sizes (100's μm to mm), is commonly free of inclusions, and is a ubiquitous phase in ultramafic rocks. Additionally, spinel is resistant to low-temperature alteration and is often the only remaining primary peridotite phase in heavily serpentinized peridotite exposures. Despite these appealing qualities, spinel has eluded thermochronometric study due to very low concentrations of U, Th, Sm and He, requiring challenging ultra-high sensitivity measurements, and due to the fact that spinel is extremely difficult to dissolve. This study outlines the analytical procedure for spinel (U-Th)/He dating, including internal screening for homogeneity using X-Ray Computed Tomography (CT), alpha-ejection/implantation correction by physical air abrasion, He extraction/measurement, and spinel dissolution.

Sample description

As the first study to date spinel with (U-Th)/He, three samples were selected from a diversity of sample types (drill cores, field samples), expected ages (1 to ~100 Ma), and

tectonic settings (mid-ocean ridge, orogenic continental massif, volcanic xenolith) to test the accuracy and broad applicability of spinel He dating (Fig. 4.1, Table 4.1).

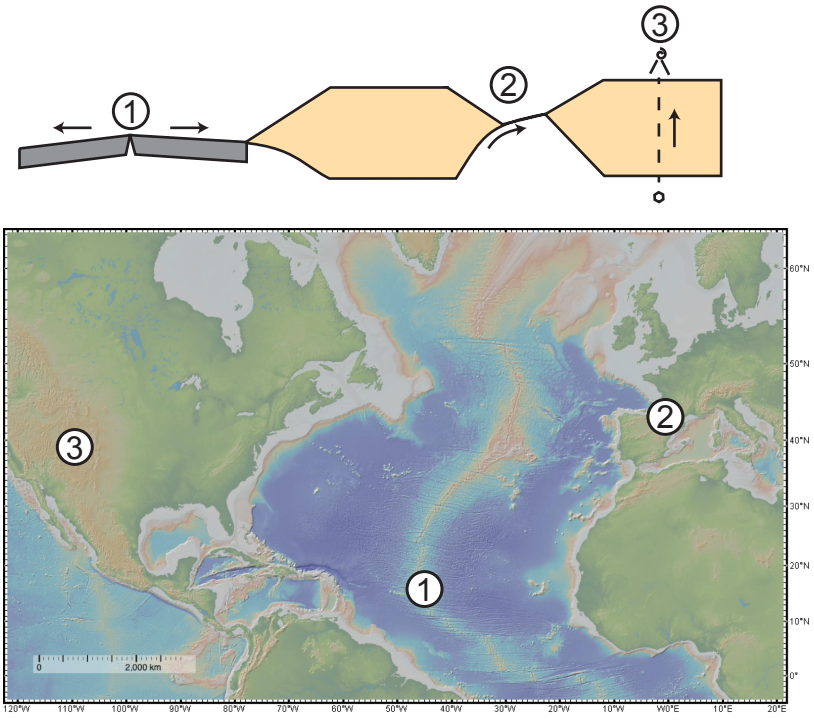

Figure 4.1: Map of spinel sample locations and tectonic settings explored in this study: 1) 15°20' Fracture Zone, mid-ocean ridge; 2) Etang de Lherz, France, continental mantle massif; 3) Green Knobs, NM, mantle xenolith. (Individual sample location maps shown in figures 4.5, 4.6, and 4.7).

IODP Leg 209, Hole 1272 - Mid Atlantic Ridge

IODP Leg 209 recovered abyssal peridotite and igneous samples from the Atlantic slow spreading ridge near the 15°20' Fracture Zone. In this section of the ridge, divergence is accommodated by oceanic detachment faults that exhume lower crustal gabbro and peridotite (Kelemen et al., 2004). The age of oceanic crust is inferred from magnetic anomaly survey (Fujiwara et al., 2003), and constrained in Holes 1275 and 1270 by U-Pb and (U-Th)/He measurements on gabbroic zircon (Grimes et al., 2011). Based on these data

and other thermo-speedometers, the estimated cooling rates at this site range from 1000 to >2000°C/Myr (Grimes et al., 2011; Coogan et al, 2007). Under these rapid cooling rates, spinel He is expected record a cooling age related to exhumation to the seafloor (i.e., the age of the oceanic crust).

Étang de Lherz, France

The Lherz Massif is a km-scale exposure of intermingled, spinel-bearing refertilized harzburgite, lherzolite, and websterite in the central Pyrenees, France (Bodinier et al., 1990; LeRoux et al., 2007). The spinel peridotite was exhumed in a mid-Cretaceous continental rift basin related to transcurrent motion of the Iberian plate relative to the European plate (Lagabrielle et al., 2010; Clerc et al., 2012). The massif is bounded on all sides by Jurassic to Aptian carbonate rocks, and sedimented breccias at the contact containing both carbonate and peridotite clasts provide evidence for tectonic reworking during exhumation (Lagabrielle and Bodinier 2008; Lagabrielle et al., 2010; Clerc et al., 2015). Extreme crustal thinning caused high-temperature, low-pressure (HT-LP) metamorphism that occurred over 25 My (110 to 85 Ma; Lagabrielle et al., 2010 and refs therein), followed by a weaker metamorphic overprint during the Pyrenean Orogeny (~ 50 Ma; Lagabrielle and Bodnier, 2008; Vacherat et al., 2014). If spinel He has a thermal sensitivity similar to magnetite He (~200-300°C), ages are expected to post-date HT-LP metamorphism.

Green Knobs, NM, USA

Green Knobs is a kimberlite diatreme on the southern end of the Colorado Plateau that contains crustal and mantle xenoliths. The diatreme outcrop measures 0.8 km across, and is associated with biotite-pyroxene-alkali feldspar minette intrusions and flows (Smith and Levy, 1976). The spinel peridotite xenoliths experienced some limited overprinting

during transport to the surface within a gas-solid mixture with < 5% hydrous minerals (Smith and Levy, 1976). While no direct age constraints exist for the xenolith vent in this study, apatite fission track ages date kimberlite diatreme emplacement at 31 Ma and K-Ar data of minettes intruding the kimberlite range from 31- 20 Ma for neighboring localities on the Colorado Plateau (Naeser, 1971; Smith and Levy, 1976; Roden et al., 1979; Laughlin et al., 1986). Spinel He ages in this quickly cooled sample should record the age of the eruption that carried the xenoliths to the surface.

Table 4.1: Summary of relevant previous work on spinel sample locations.

Location/Sample	Setting	Thermal History	Age Constraints	References
Leg 209 15°20' FZ 209-1272A-1-1-27-29	Mid-Ocean Ridge	Cooling rates: > 1000 °C/my	Zircon U-Pb: 2.2-1.3 Ma Zircon He: 1.8 – 0.6 Ma Magnetic Anomaly: 1-2 Ma	Fujiwara et al., 2003; Grimes et al., 2011
Lherz, France 12WLB	Continental Massif	Pre-rift crust-mantle boundary: 700-850°C Rift HT metamorphism: 600°C	Ar-Ar, Sm-Nd: 110-105 Ma Zircon FT: 80-65 Ma Zircon He: < 50 Ma	Yelland et al., 1991; Mouthereau et al., 2014; Vacherat et al., 2016
Green Knobs, NM EMNG2	Mantle Xenolith	Cooling rates: >> 1000 °C/my	Biotite, hornblende K-Ar: 31-20 Ma Apatite FT: 35-31 Ma	Naeser 1971; Roden et al., 1979; Laughlin et al., 1986

Methods

Mineral separation and sample screening

Spinel grains were extracted from whole rock samples by a variety of mechanisms. Large sample volumes (> kg) were put through jaw and cone crushers, and the crushed whole rock mineral separate was fed through a Gemini water table for density separation. Smaller samples (~ g's) were either crushed gently by hand using a mortar and pestle, or separated in a SelFrag high-voltage rock fragmenter. In each case, intact spinel grains or

large fragments were readily separated from the whole rock and were picked by hand based on size (> 100 μm) and morphology (euhedral to subhedral) using an optical microscope (Fig. 4.2).

Picked grains were scanned using X-Ray Computed Tomography (CT) at The University of Texas at Austin's NSF Multi-User Facility at a 4-6 μm resolution to eliminate grains with detectable inclusions, which can act as He traps, sources for parentless He, or fast diffusion pathways (Fig. 4.2). Additionally, since sample preparation for (U-Th)/He is destructive to the sample, CT was used to pre-screen the intact core sample from Leg 209 prior to crushing. The CT scan revealed euhedral mineral grains of sufficient size and abundance to warrant mineral separations on this sample (Fig. 4.3). Future work on precious abyssal peridotite core samples can integrate CT screening to gain a quick view within the sample to help avoid needlessly crushing samples that do not have appropriate grains for dating.

Correction for long alpha stopping distances

Due to energy expelled during alpha decay, He atoms can travel ~15-20 μm from the parent atom, which causes He exchange at the grain boundary (e.g., Ketcham et al., 2011). In phases with high U, Th, Sm concentrations, such as zircon and apatite, this results in a net loss of He from the outer grain boundary, and can be corrected mathematically by applying an F_T correction (Farley et al., 1996). In low U, Th, Sm phases, such as Fe-oxides, long alpha stopping distances can lead to net He implantation at the grain boundary from neighboring phases (Blackburn et al., 2007). To correct for He implantation, the outer ~20 μm of the grain boundary must be removed by physical air abrasion, polishing or crushing. Given that the spinel in this study, like Fe-oxides, have very low U, Th, Sm concentrations

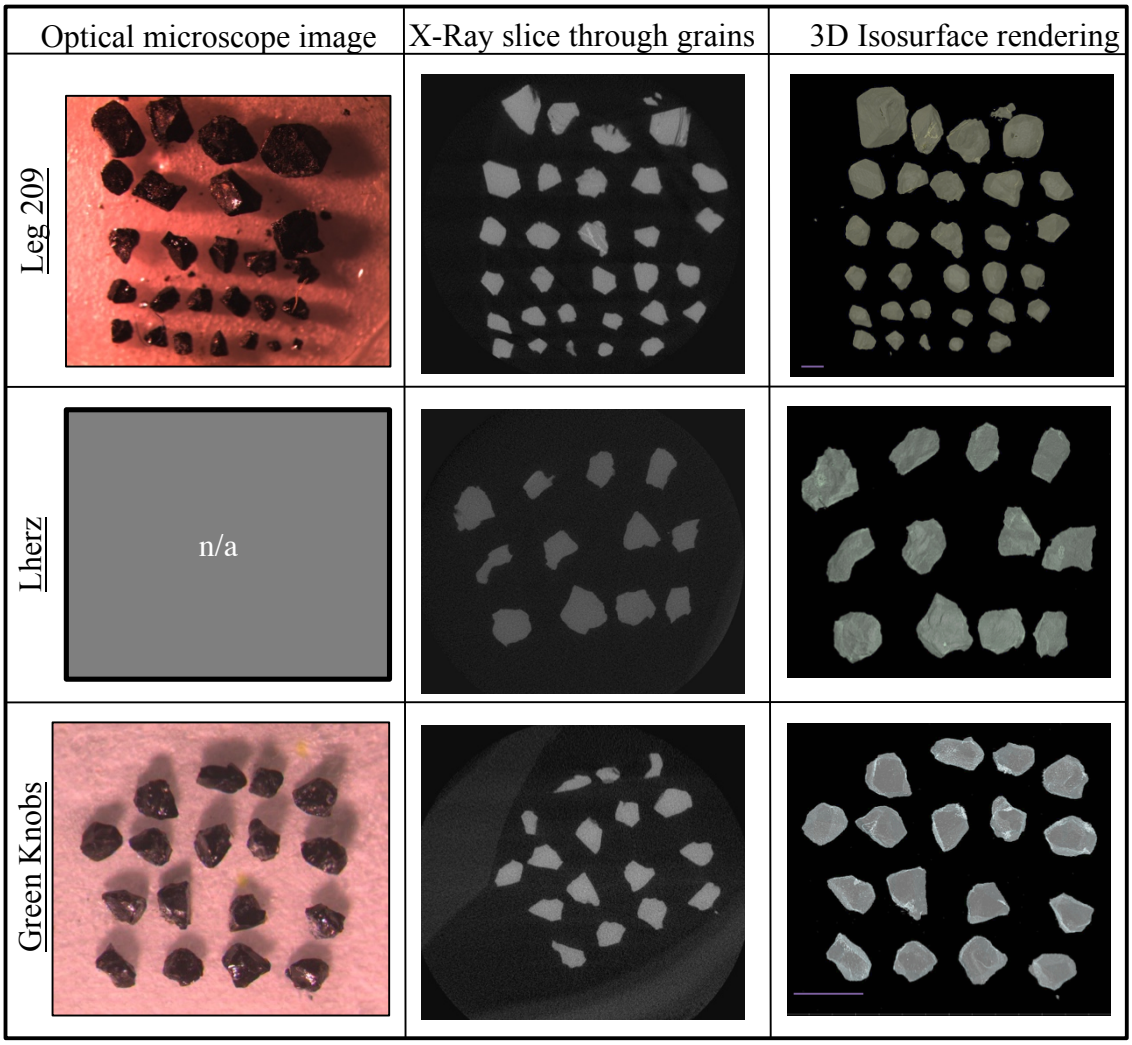

Figure 4.2: Representative spinel grains picked from three samples. On the left are optical microscope photos of grains picked for a CT grain mount. The middle column shows a single "slice" through the CT X-Ray data. Brightness is a function of density and atomic number (z). Variations in brightness may be partly due to the data processing, or a function of Fe, Cr, Al content in the spinel. Very bright veins or rims are likely magnetite. The right column shows a 3D Isosurface rendering of the CT data using Avizo software. Scale bars are all 500 μm.

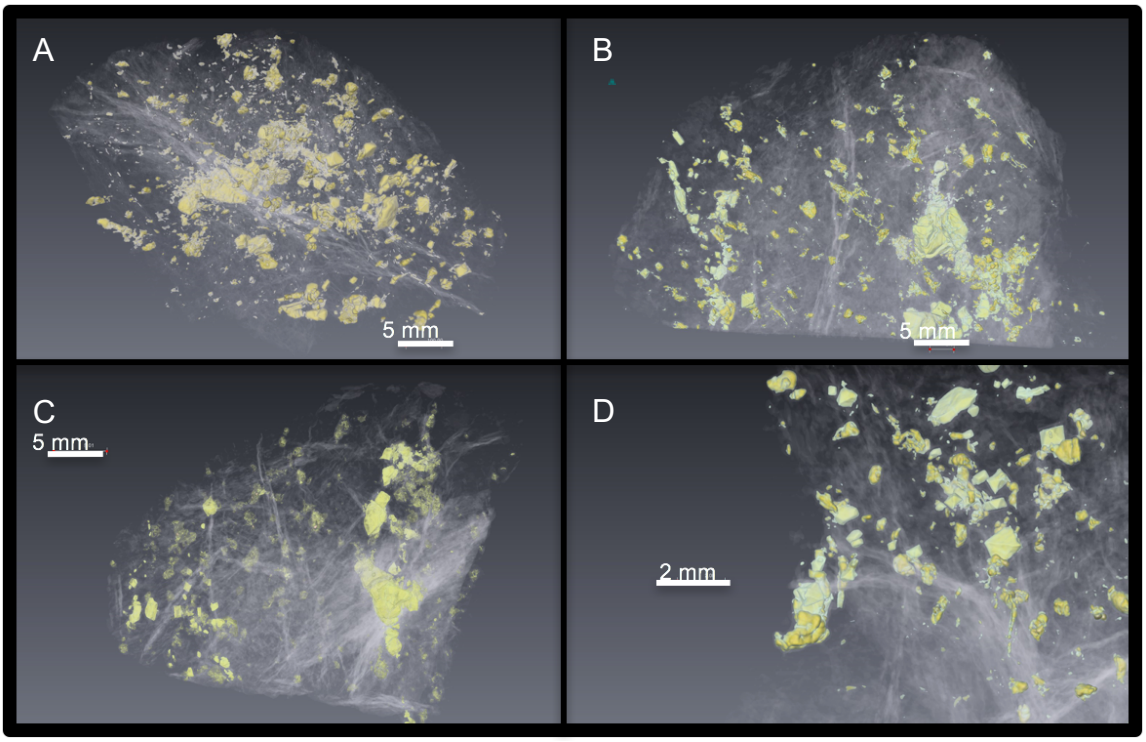

Figure 4.3: Volume renderings of Leg 209 core sample using X-Ray Computed Tomography data. Yellow is used to highlight internal grains with high density. White, partially transparent serpentine veins are also visible. A-C shows the whole core samples from different angles. D shows a zoomed in section of the core where euhedral octahedral spinel are visible.

(< 100 ppb), the grains were air-abraded for 2-4 hours at 6 psi until rounded to remove any grain boundary phases or implanted He, following the protocols outlined in Blackburn et al. (2007) and Cooperdock and Stockli (2016).

(U-Th)/He measurements

(U-Th)/He analyses were completed at the UTChron facility at The University of Texas at Austin. Aliquots were constructed by combining 1–12 similarly sized abraded grains into platinum packets for degassing. ^{4}He concentrations were measured using a Thermo HelixSFT™ split flight tube noble gas mass spectrometer and a Blazers Prisma QMS-200 quadrupole mass spectrometer (QMS). Individual aliquots were heated with a DiodeLaser to a pyrometrically calibrated temperature of ~950°C, with blanks run between each unknown to monitor background and drift. Aliquots were reheated until ^{4}He gas yields became < 1% total gas, or < 2x procedural blank concentrations. The number of degassing steps varied by sample, but the majority of the spinel were fully degassed after two 10-minute heating steps. Final ^{4}He concentrations (ncc) were blank-corrected and calculated against a manometrically calibrated ^{4}He standard of known concentration. Final ^{4}He analytical errors were calculated by propagating uncertainties on each unknown measurement and the deviation of the blanks measured throughout the run. Typical propagated analytical uncertainties range from 2% in the Lherz spinel up to 40% in the extremely low concentration Leg 209 spinel.

After degassing, spinel grains were unpacked from the platinum capsules into 3 mL square body Savillex™ vials and dissolved using HF-HNO_3 and HCl in a Parr™ acid digestion vessel (PDV) (Appendix 2). First, the samples were spiked with a solution of ^{235}U, ^{230}Th, and ^{149}Sm in 5% HNO_3, followed by ~ 200 μl of a 4:1 mixture of concentrated HF - HNO_3. PDVs were heated in an oven at 220°C for 4 days. Once removed, the acid

was dried down on a hotplate and samples were visually inspected. If opaque spinel grains were still visible then the concentrated HF-HNO_3 step was repeated. The number of HF-HNO_3 steps required to fully dissolve the spinel varied by sample from one to four times.

Once the samples contained only traces of a white residue, 200 μl of concentrated HCl were added and samples were heated in the PDVs overnight at 180°C. After chloride conversion, the solution was dried down to a small bead and 100 μl of 7N HNO_3, then 500 μl of MilliQ H_2O were added for ICP-MS analysis.

Sample solutions were run on a Thermo Element2 HR-ICP-MS. Two to three unknowns were selected to be re-analyzed at the end of the run to monitor machine drift and reproducibility on these low-concentration samples.

Final U-Th-Sm concentrations were calculated using isotope dilution with the mixed spike calibrated against a gravimetric 1 ppb U-Th-Sm standard solution. Final concentrations are blank-corrected based on the spike blank associated with each ICP-MS run. Analytical uncertainties varied by isotope with Th uncertainties of < 1%, U < 1 to 11% and Sm < 1 to 3%. The relatively high uncertainty in some measurements is a function of extremely low concentrations (< 10 ppb) of these elements in spinel. Calculated mean ages are reported with a two-standard error.

Results

Spinel He age results from three samples are reported in Fig. 4.3 and Table 4.2. Spinel grains from IODP Leg 209 yielded the lowest He concentrations of all samples (0.3 – 2.3 pmol/g) and, as a result, had the highest He propagated uncertainties (4-40%) despite aliquot masses of 200 – 1000 μg. Final calculated ages on nine aliquots composed of 1 to 4 grains ranged from 0.7 ± 0.1 to 1.8 ± 0.3 Ma, with one anomalously old age of 6.6 ± 0.8 Ma. This older aliquot had an order of magnitude more He (0.23 pmol/g) than aliquots with

similar U concentration (~6 ppb), indicating that it likely suffers from excess He (inherited or implanted) and was discarded. The remaining eight aliquots have a mean age of 1.1 ± 0.3 Ma (2SE).

Lherz aliquots were constructed with 2 – 12 abraded grains and had total aliquot masses of 495 to 1200 μg. Final He results from four aliquots yield ages from 60.7 ± 5.2 to 98.8 ± 6.7 Ma, with a mean age of 75.3 ± 16.4 Ma (2SE).

Aliquots of Green Knobs xenolith spinel were assembled with 5 – 6 abraded grains, and had total aliquots masses of 340 to 575 μg. A total of six aliquots produce He ages ranging from 8.9 ± 0.8 to 14.3 ± 1.3 Ma, with a mean age of 11.7 ± 1.8 Ma (2SE).

All samples have a two-standard error uncertainty about the mean of 20-25%, despite a different number of aliquots run for each sample (n = 4, n = 6, n = 9, respectively). Although the number of observations is limited, this may suggest that propagated analytical error underestimates the true error of the method. A significant number of additional analyses must be done to determine the precise estimate of the error.

Spinel from all samples have consistently very low U, Th and Sm concentrations (< 20 ppb). To measure the uncertainty of such low concentration measurements over a multi-hour analytical run, two to three unknowns were run twice within the same ICP sequence and are reported in Table 4.2. Although some replicated U, Th and Sm concentrations differ greater than the analytical uncertainty of the measurement, the variation is less than the overall uncertainty of the final calculated He age. Spinel He ages do not show systematic trends with U, Th or Sm concentrations, Th/U ratios, or mass/grain size. For this reason, ages are plotted against ^{4}He concentration (pmol/g) and show positive age trends with He for all samples (Fig. 4.3).

Table 4.2: Spinel (U-Th)/He age data

Aliquot	Age (Ma)	U (ppb)	Th (ppb)	Sm (ppb)	Th/U	^{4}He (pmol/g)	mass (µg)	# of grains	mass per grain (µg)
IODP Leg 209 (209-1272A-1-1-27-29)									
209HM-1	1.8 ± 0.3	6.9 ± 0.7	0.9 ± 0.003	1.9 ± 0.02	0.13	0.07	708	3	236
209HM-2	0.7 ± 0.1	7.0 ± 0.1	2.1 ± 0.008	3.2 ± 0.08	0.30	0.03	433	4	108
209HMab-1	6.2 ± 1.0	6.6 ± 0.5	0.7 ± 0.003	2.6 ± 0.03	0.10	0.23	523	1	523
209HMab-1 (rep)		5.8 ± 0.2	2.5 ± 0.009	5.3 ± 0.04					
209HMab-2	0.8 ± 0.3	7.5 ± 0.2	7.0 ± 0.015	1.1 ± 0.03	0.94	0.04	611	1	611
209HMab-3	1.0 ± 0.5	5.7 ± 0.4	0.8 ± 0.003	1.4 ± 0.01	0.15	0.03	1006	3	335
209HMab-3 (rep)		7.3 ± 0.3	0.9 ± 0.003	1.4 ± 0.03					
209HMab-4	1.3 ± 0.6	8.8 ± 0.3	2.7 ± 0.010	3.0 ± 0.02	0.31	0.07	458	4	115
209HMab-5	0.8 ± 0.4	11.8 ± 0.2	1.5 ± 0.008	2.0 ± 0.02	0.13	0.05	683	4	171
209NMab-1	1.8 ± 0.8	18.8 ± 0.6	3.1 ± 0.010	3.5 ± 0.03	0.17	0.19	199	4	50
209NMab-2	1.3 ± 0.6	13.4 ± 0.4	1.5 ± 0.006	6.4 ± 0.15	0.11	0.10	643	3	214
Mean: 1.1 Ma ± 0.3 (2SE)									
Lherz, France (WLB)									
12WLB-2	71.4 ± 4.3	6.7 ± 0.2	3.0 ± 0.0012	4.1 ± 0.04	0.45	2.92	495	12	41
12WLB-4	60.7 ± 5.2	1.6 ± 0.0	0.7 ± 0.0001	2.9 ± 0.02	0.43	0.60	1187	2	594
12WLB-5	98.8 ± 6.7	6.4 ± 0.1	2.1 ± 0.0034	15.0 ± 0.16	0.33	3.83	366	4	91
12WLB-6	70.3 ± 9.2	1.6 ± 0.0	13.0 ± 0.0076	4.0 ± 0.06	7.98	0.86	511	6	85
Green Knobs, NM (EMNG2)									
EMNG2ab-4	14.4 ± 2.1	3.6 ± 0.2	1.8 ± 0.0084	71.4 ± 0.79	0.50	0.35	510	6	85
EMNG2ab-5	14.7 ± 1.4	4.4 ± 0.0	3.3 ± 0.0051	4.3 ± 0.04	0.77	0.40	326	6	54
EMNG2ab-5 (rep)		3.9 ± 0.0	2.9 ± 0.0066	4.3 ± 0.11					
EMNG2ab-6	9.0 ± 0.8	4.5 ± 0.1	5.4 ± 0.0201	2.4 ± 0.03	1.22	0.28	575	6	96
EMNG2ab-6 (rep)		4.7 ± 0.6	5.7 ± 0.0337	3.6 ± 0.04					
EMNG2ab-7	9.6 ± 0.9	5.3 ± 0.0	6.3 ± 0.0142	3.7 ± 0.09	1.20	0.34	378	5	76
EMNG2ab-8	12.4 ± 1.2	4.2 ± 0.1	2.3 ± 0.0088	0	0.55	0.31	541	6	90
EMNG2ab-8 (rep)		3.9 ± 0.1	2.3 ± 0.0070	0					
EMNG2ab-9	9.5 ± 0.6	11.9 ± 0.1	9.9 ± 0.0534	4.4 ± 0.11	0.83	0.73	477	5	95
Mean: 11.6 Ma ± 2.1 (2SE)									

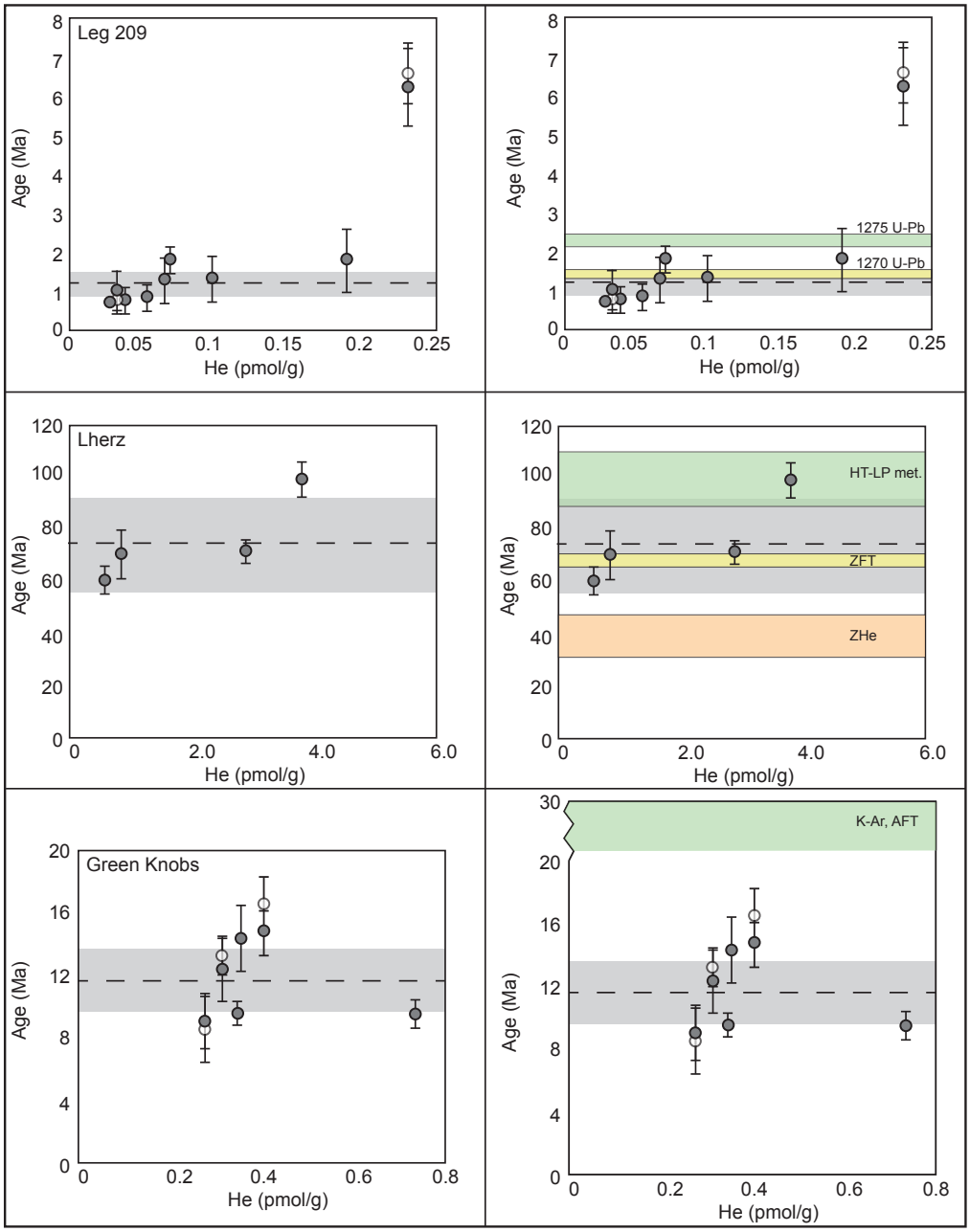

Figure 4.4: Spinel (U-Th)/He ages for the three study locations. On the left individual aliquots are plotted versus He concentration. White circles are replicates, run twice for U, Th, and Sm concentrations on the ICP-MS. Error bars are propagated analytical error. The black dashed line shows the mean sample age, and the gray bar is the two-standard error envelope. On the right the same spinel data is plotted with local thermochronological constraints shown in colorful bars (Laughlin et al., 1986; Yelland, 1991; Henry et al., 1998; Grimes et al., 2011).

Interpretation

To determine the exhumation age of peridotite by magmatic and tectonic processes, spinel (U-Th)/He ages were collected on samples from an array of ages and settings. The spinel He age results are evaluated based on their reproducibility and agreement with expected age outcomes given the thermal history and independent geochronological age constraints for each sample (Table 4.1). Samples from IODP Leg 209 and Lherz localities yield mean ages that are in excellent agreement with independent age constraints, demonstrating that spinel He has the potential to provide accurate peridotite exhumation and cooling ages. The Green Knobs xenolith sample results are reproducible, although younger than the expected eruption age based on previous K-Ar data. The significance of these results will be discussed below. Overall, the method outlined in this study lay the foundation for a promising new mineral dating system with the potential to provide cooling history information on fast cooled and slow cooled peridotite exhumation, as young as 1 Ma.

Spinel He chronometry on oceanic crust

At the Mid-Atlantic Ridge, where exhumed spinel peridotite cools rapidly from magmatic to seafloor temperatures during seafloor spreading, on-axis mid-ocean ridge cooling rates exceed 1000°C/Myr (Grimes et al., 2011). In this setting, the spinel He age is expected to record when the sample is exposed on the seafloor, i.e, the age of the oceanic crust. Therefore, should spinel from Leg 209 Hole 1272 effectively date seafloor spreading at this magma-poor spreading ridge, the He age should agree with independent magnetic anomaly ages estimates and spreading rates. Gabbroic zircon from two other drill holes (1275, 1270) dated via U-Pb and (U-Th)/He show a systematic increase in age (U-Pb 1.28 ± 0.03 to 2.12 ± 0.18 Ma) with distance from the ridge axis (15 to ~28 km), consistent with

a half-spreading rate of ~12-15 mm/yr (Fujiwara et al., 2003; Grimes et al., 2011) (Fig. 4.5).

The 1.1 ± 0.3 Ma (2SE) age of Leg 209 spinel from Hole 1272 is in agreement with the expected age of oceanic crust for this site based on magnetic anomaly data (~ 1 Ma; Fujiwara et al., 2003), and the spreading rate based on the drill hole location ~ 15 km from the ridge axis (Kelemen et al., 2004). These results confirm that spinel He dating may provide a good proxy for the age of the seafloor dominated by exhumed abyssal peridotite. This presents exciting new prospects for future applications in oceanic settings, such as dating the exposure age of abyssal peridotites, determining spreading rates at slow spreading ridges, and placing minimum age constraints on the magmatic crystallization of spinel at mid-ocean ridge settings.

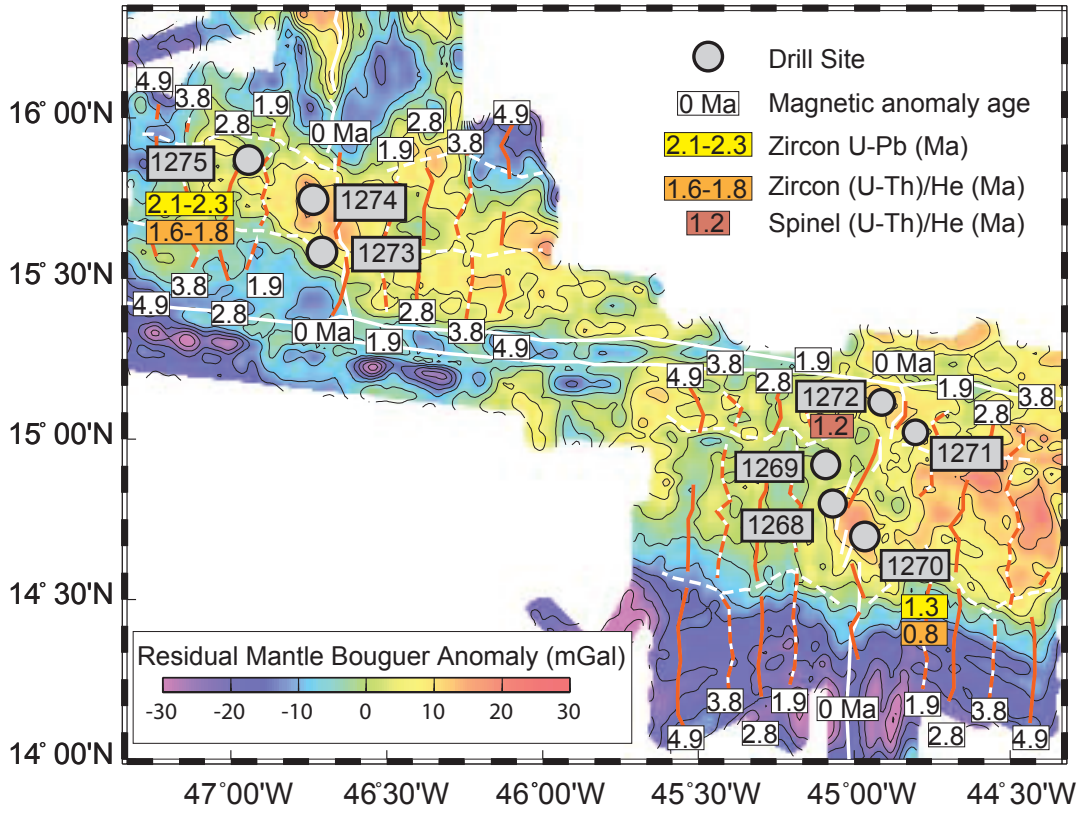

Figure 4.5: Map of IODP Leg 209 drill sites with ages (Modified from Fujiwara et al., 2003). Drill site locations are indicated by gray circles. Inferred oceanic crust age from magnetic anomaly data shown in white boxes. Zircon U-Pb and (U-Th)/He ages for gabbro from Holes 1275 and 1270 shown in yellow and orange (Grimes et al., 2011). Spinel He from Hole 1272 shown in red.

Spinel He chronometry on orogenic peridotite massifs

Results from Lherz also agree well with predicted cooling ages based on the thermal history of the Lherz massif and independent age constraints from the surrounding Northern Pyrenean Zone. Prior to exhumation in the Cretaceous (~110-105 Ma), the massif existed as subcontinental mantle at temperature conditions ranging from ~700 to 800°C (Vielzeuf and Kornprobst, 1983; Henry et al., 1998; Clerc et al., 2016). Concurrent with exhumation, the region experienced extended high temperature metamorphism (~600°C) from 110-85 Ma (Albarede and Michard-Vitrac, 1978; Montigny et al., 1986; Clerc and Lagabrielle, 2014). Although Lherz spinel He age results have a high intrasample variability with results ranging from 61 to 99 Ma, the mean age of 75.3 ± 16.4 Ma (2SE) is in overall agreement with cooling post thermal relaxation below 600°C.

These ages are distinctly younger than those determined by higher-temperature chronometers ($^{40}Ar/^{39}Ar$, Sm/Nd, U-Pb; Henry et al., 1998; Odlum, unpublished data), which date massif exhumation from mantle to crustal levels at 105 Ma during high temperature metamorphism. Regional zircon He and apatite fission track ages associated with the Pyrenean Orogeny all date < 50 Ma, suggesting a spinel He closure temperature > 180°C (Mouthereau et al., 2014; Vacherat et al., 2016) (Fig. 4.6). The Lherz spinel He age range is most consistent with nearby zircon fission track ages (80-65 Ma; Yelland, 1991). This highlights the potential of spinel He to serve as a thermochronometer for reconstructing thermal histories in peridotite massifs through temperatures lower than the Sm/Nd or $^{40}Ar/^{39}Ar$ chronometric systems capture, and may be expanded to constrain low-temperature thermal histories in other continental settings, such as orogenic peridotites.

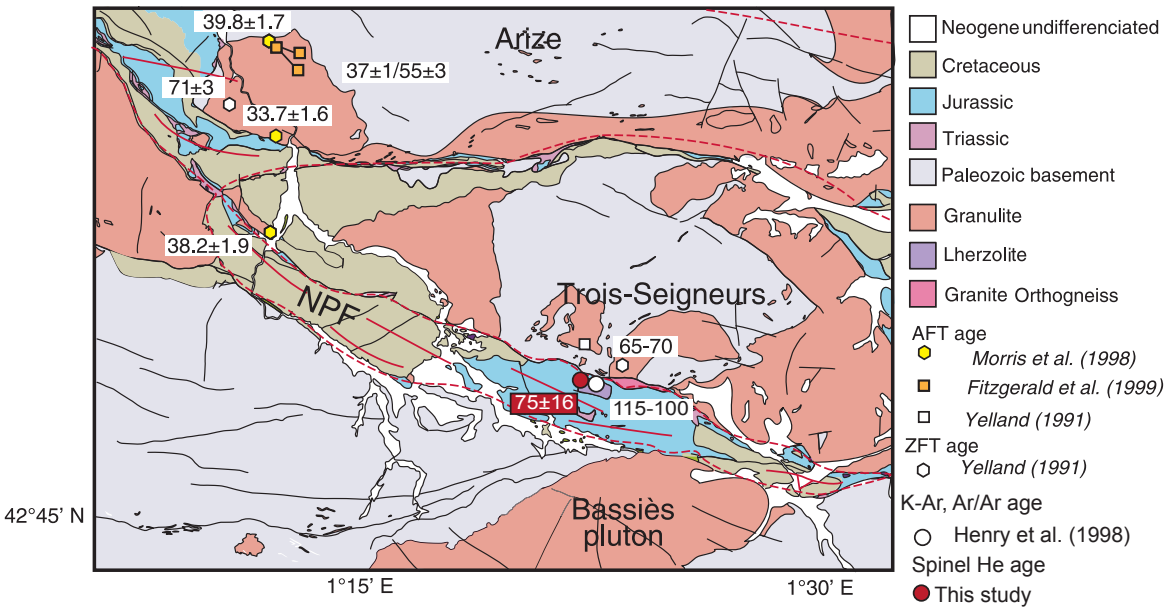

Figure 4.6: Geologic map of Lherz region with ages (modified from Mouthereau et al., 2012). Thermochronological age constraints for apatite fission track, zircon fission track, K-Ar and $^{40}Ar/^{39}Ar$ are differentiated by symbol and color on the map. Spinel He ages from this study are shown with a red circle.

Spinel He chronometry on volcanic xenoliths

Mantle xenoliths sampled from volcanic vents in Green Knobs, NM represent a setting where the peridotite experienced rapid cooling from magmatic to surface temperatures during a volcanic eruption. As such, it is expected that spinel He would provide an eruption age for the volcanism that brought the xenolith to the surface, or a cooling age if the sample were reheated due to post-eruption reheating. Previous geochronology studies are sparse in the Green Knobs area. The few studies that exist are on neighboring localities within the region and report apatite fission track ages of 35-31 Ma (Naeser, 1971), and biotite and hornblende K-Ar ages of 31-20 Ma (Smith and Levy, 1976; Roden et al., 1979; Laughlin et al., 1986) (Fig. 4.7). Given these studies, the significance of the reproducible, but young 11.7 ± 1.8 Ma spinel He age is puzzling.

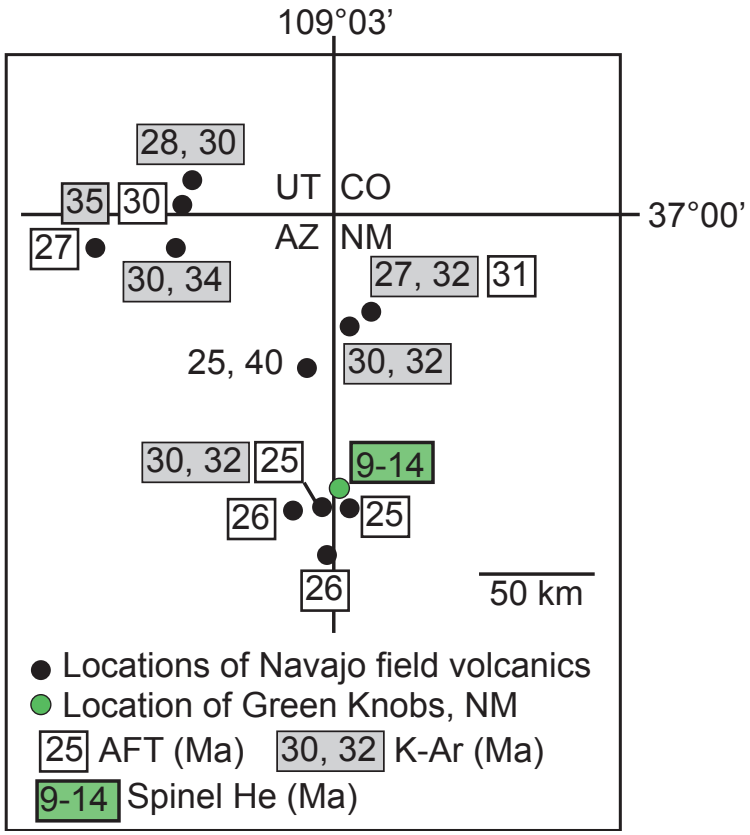

Figure 4.7: Schematic map showing locations of minettes and kimberlite diatremes in the Navajo Volcanic Fields near the Four Corners region, USA. Apatite fission track and K-Ar ages are shown in white and gray boxes. Spinel He ages from this study on Green Knobs, NM are in green.

Several geologic factors may contribute to this age result. This includes the possibility that the spinel age represents 1) an eruption of a much younger volcanic event; 2) reheating by a younger magmatic intrusion that reset the spinel He age; 3) delayed cooling through the spinel He closure temperature; or 4) alteration/recrystallization of the spinel post-eruption that could have partially reset the He. Although similar volcanism younger than 20 Ma has not been previously documented for the CO plateau, as mentioned before, no alternative age constraints exist specifically for the Green Knobs locality.

Additionally, Green Knobs, as the name implies, has experienced aqueous alteration that has caused serpentinization of the xenoliths (Smith and Levy, 1976). Therefore, it is feasible that the spinel He age may record either a younger eruption event, or post-eruption alteration.

An alternative factor to consider is the effect of spinel composition on spinel He closure temperature. Although chemical analyses were not performed on the spinel analyzed in this study, others document aluminous spinel in Green Knobs (Smith and Levy, 1975). Future studies can address this effect by performing He diffusion experiments on spinel samples with different Mg, Al, Cr and Fe contents. In sum, there is insufficient data to draw a conclusion for the significance of this sample age at the present time, however the reproducibility of the results suggests a geologically systematic cause.

Spinel He closure temperature

While these case studies largely explore very rapid tectonic to nearly instantaneous volcanic/magmatic cooling, for spinel to be used as a thermochronometer to resolve more general thermal histories, it will be necessary to measure the He diffusion kinetics to quantify the thermal sensitivity of the system. Although spinel He diffusion kinetics are not yet determined, an esimated He closure temperature can be bracketed. The mantle temperatures at which spinel crystallize (≥ 700°C) (Fabries, 1979) provide an absolute maximum upper temperature bound. Hence, spinel (U-Th)/He is expected to date the cooling of spinel grains rather than crystallization, except in the case of extremely rapid cooling rates, where the crystallization age and cooling age may be indistinguishable.

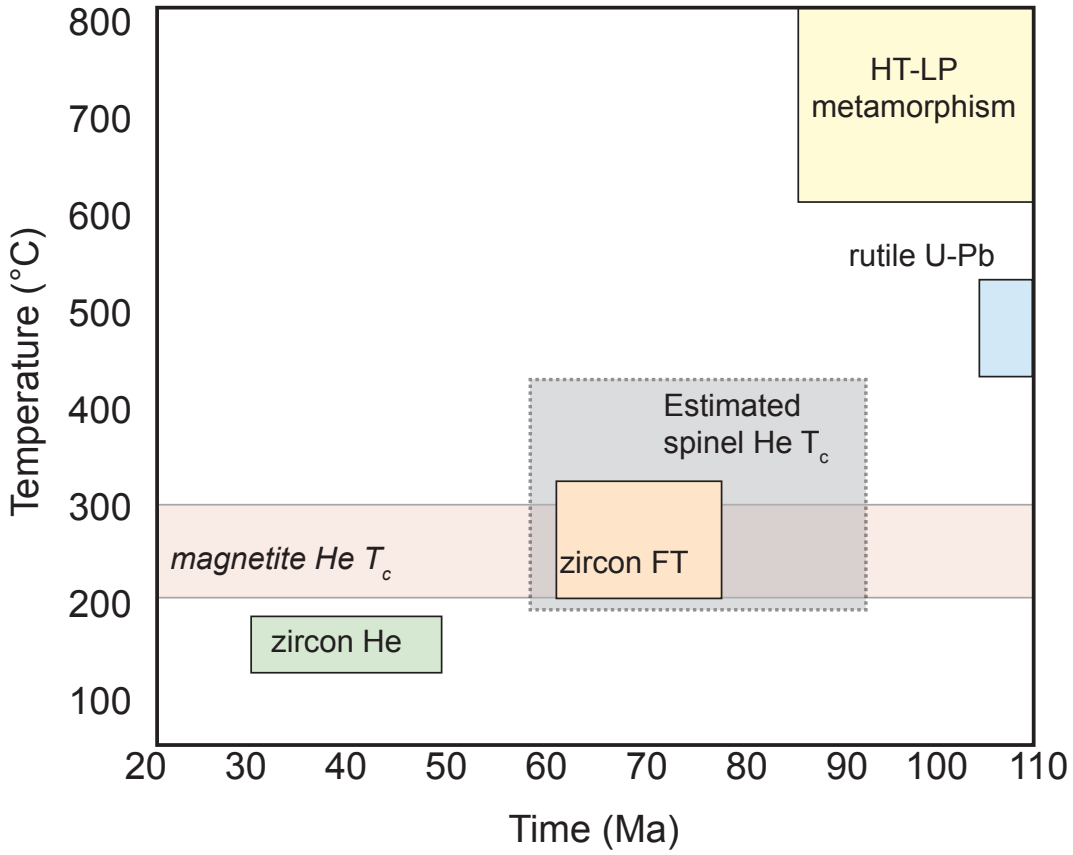

Figure 4.8: Time-temperature diagram of the Lherz massif, France regional thermochronometric constraints. High-temperature chronometers (U-Pb, Sm-Nd, $^{40}Ar/^{39}Ar$) record high-temperature metamorphism (> 500°C) from 110-85 Ma. Zircon fission track ages record cooling through ~ 200-300°C from 75-60 Ma, while zircon He reset by the Pyrenean contraction are ≤ 50 Ma. Based on these independent thermal history constraints, and the spinel He age results, we estimate a closure temperature for the spinel He system between 500 and 200°C, likely similar to the closure temperature of zircon fission track or magnetite (U-Th)/He systems (300-200°C).

Given that spinel has a similar chemical formula and density to magnetite, as well as an identical crystal structure [$(A^{2+}B^{3+}{}_2)O^{2-}{}_4$], it would seem reasonable to postulate that spinel has a similar He closure temperature to magnetite. Magnetite has experimentally determined He diffusion kinetics and is characterized by a He closure temperature of 250 ± 40°C for 500 μm and 10°C/my cooling rate (Blackburn et al., 2007), which is a similar

closure temperature range to zircon fission track (~200-300°C; Zaun and Wagner, 1985; Bernet, 2009) (Fig. 4.8). This predicted spinel closure temperature appears to be consistent with the Lherz spinel He age results, which predominantly coincide zircon fission track cooling ages (Fig. 4.8) (80-65 Ma; Yelland, 1991). Given these estimated constraints, the spinel He system is expected to constrain when the sample cooled through middle to upper crustal temperatures via exhumation, the timing of cooling post metamorphic reheating, or the timing of an eruption.

Conclusions

Peridotite thermochronology by dating spinel with (U-Th)/He was tested on three localities from a variety of tectonic settings and predicted exhumation ages. Spinel (U-Th)/He effectively determined the age of exhumed abyssal peridotite from the Mid-Atlantic Ridge at the 15°20' Fracture Zone, in agreement with the age of seafloor spreading as constrained by magnetic anomalies and U-Pb ages on gabbros. Spinel (U-Th)/He on the Lherz continental mantle massif, France provides cooling ages consistent with the regional cooling history post-HT-LP metamorphism during contractional exhumation. Spinel from a mantle xenolith from Green Knobs, NM yield a reproducible (U-Th)/He age consistent with fast cooling during volcanic eruption. The age, however, is younger than any known volcanism in the area, and requires further dating to resolve this discrepancy. In sum, these case study results demonstrate that (U-Th)/He dating of magmatic spinel may be a suitable and reliable technique to date mantle exhumation for a variety of geologic settings that contain spinel-bearing lithologies.

Appendix 1: Magnetite Dissolution Procedure

Day One:

1. After He extraction grains must be unloaded from Pt jackets.
2. Place unloaded grains into small, clean Savillex vials.
3. Leave a small drop of alcohol to keep grains at the bottom.
4. Note how many grains are present after degassing, and any changes in morphology.
5. Once in clean lab, remove caps and place vials on hot plate at ~120 °C to dry down alcohol.
6. Once dry, quickly place ~3 drops (~100 μl) of concentrated 14N HNO_3 into Savillex vials.
    a. Over drying samples at this step may cause static electricity to eject grains from vials.
7. Add 100 μl of U-Th-Sm spike to the sample.
8. Take care that every drop leaves the pipette tip.
    a. Do not re-use pipette tips that touch the sample or any surface.
9. Prepare Spike Blanks and New Normal solutions in parallel with aliquots.
    a. Spike blanks: 100 μl of U-Th-Sm spike + 500 μl MQ H_2O
    b. New Normals: 100 μl of U-Th-Sm spike + 1000 μl New Normal solution
10. Add ~ 12 drops (~400 μl) of concentrated HF to vials.
11. Tightly cap vials and cook overnight (~12 hrs.) at 180°C.

Day Two:

12. The next morning, unplug the hot plate and allow vials to cool.
13. Inspect the samples.

a. All dark opaque grains should be fully dissolved. Some white material may remain and is likely iron precipitate from the saturation of Fe in the HF solution.

14. Dry down the samples to a small bead at 180°C.
15. Add ~6 drops (~ 200 μl) of concentrated HCl and cook for 12 hours on a hotplate at 180°C.

Day Three:

16. The next morning, unplug the hot plate and allow vials to cool.
17. Once cool, inspect samples for any undissolved material.
    a. After chloride conversion, the sample should appear bright yellow and should be completely free of precipitate or grains.
18. Dry down this solution to as small of bead as possible at 180°C.
19. Add 100 μl 7N HNO_3 to vials and cook for 40 min in apatite oven (90°C).
20. Remove from apatite oven, let cool.
21. Add 500 μl of MQ H_2O and transfer to ICP vials.

Day Four:

22. Allow to equilibrate overnight, then you are ready to run on the ICP-MS.

Appendix 2: Spinel Dissolution Procedure

3. After He extraction grains must be unloaded from Pt jackets.
    a. Place unloaded grains into hexcap Savillex vials
    b. Leave a small drop of alcohol to keep grains at the bottom.
    c. Note how many grains are present after degassing, and any changes in morphology
4. Once in clean lab: remove caps and place beakers on hot plate at ~120 °C to dry down alcohol.
5. Once dry, quickly place ~3 drops (~100 μl) of concentrated 14N HNO_3 into Savillex vials.
    a. Over drying samples at this step may cause static electricity to eject grains from vials.
6. Add 100 μl of U-Th-Sm spike to the sample.
    a. Take care that every drop leaves the pipette tip.
    b. Do not re-use pipette tips that touch the sample or any surface.
7. Prepare Spike Blanks and New Normal solutions in parallel with aliquots.
    a. Spike blanks: 100 μl of U-Th-Sm spike + 500 μl MQ H_2O
    b. New Normals: 100 μl of U-Th-Sm spike + 1000 μl New Normal solution
8. Add ~ 12 drops (~400 μl) of concentrated HF to vials.
9. Loosely screw the caps on vials.
    a. Do not tightly screw on caps to allow acid vapors to move in and out.
10. Add 3 ml of concentrated HNO_3 to PDV inner jackets.
11. Add 10 ml of concentrated HF to PDV inner jackets.
12. Carefully stack Savillex vials in PDV inner jackets (4 fit into one PDV).
    a. Make sure the lid of the inner jacket fits securely.

13. Cook in HF oven at 220°C for 3.5 days.
14. Remove from oven, let cool, and dry down HF to a small bead.
15. IF spinel grains do not look dissolved, repeat steps 3, 6-11.
    a. Often the first HF-HNO_3 step is not sufficient to dissolve the spinel grains.
16. When samples are transformed to white/clear precipitate after the HF-HNO_3 step, add 400 μl of concentrated HCl to each vial.
17. Add 13 ml of concentrated HCl to the PDV inner jacket.
18. Carefully stack savillex vials in PDV inner jackets (4 fit into one PDV).
    a. Make sure the lid of the inner jacket fits securely.
19. Cook in HCl oven 180°C for 12 hours.
20. Remove from oven and let cool, and dry down HCl to a small bead.
21. Add 100 μl 7N HNO_3 to vials and cook for 40 min in apatite oven (90°C).
22. Remove from apatite oven, let cool.
23. Add 500 μl of MQ H_2O and transfer to ICP vials.
24. Allow to equilibrate overnight, then you are ready to run on the ICP-MS.

Appendix 3: How to make a CT mount

This procedure is designed to scan a 5 mm^3 volume. Ideal shape is a 5 mm x 5 mm cylinder.

Materials needed:

- thumb tack
- discarded paper rounds from hole puncher
- double-sided sticky tape
- small scissors
- microscope slide
- tweezers
- parafilm
- (optional) hole puncher rounds of a thin sheet of plastic

I. Prepare your grains; this will vary based on grain size.
   a. For mm-cm size grains: Crush grain with mortar and pestle. Pick individual internal fragments that have no clear crystal faces or attached matrix material. The number of fragments to go into one scan will depend on grain size.
   b. For μm size grains: Pick individual grains from mineral separate. Grain sizes and morphologies will vary by sample. Ideal grains are euhedral, and $\geq 100\ \mu$m.

II. Once grains or fragments are picked prepare a microscope slide.
   a. Place 3 to 4 paper rounds down on the microscope slide. Each of these will be a different layer.

b. Place one, long piece of double sided sticky tape over the paper rounds.

c. Number or name each paper round with a fine pen if multiple samples will be combined into one scan.

III. Carefully place selected grains onto the double sided sticky tape, over the paper rounds.

a. Try to place grains of similar grain size onto a single paper round (i.e., layer).

b. Grains may be closely packed, but should not be touching.

c. Place grains in the center of the paper round, in a grid shape if possible.

IV. Once each paper round (layer) is full, take photos of each layer.

V. Prepare thumb tack.

a. Place a small piece of double-sided sticky tape on the flat surface of the thumb tack.

b. Use the scissors to trim the tape so that it does not overhang the edges of the thumb tack.

c. Use the scissors to carefully cut out each layer of grains from the microscope slide.

d. Lift the tape until one paper round becomes loose from the slide.

e. Use the scissors to carefully cut around the paper.

f. Grains should not move if they are stuck to the sticky tape on the surface of the paper.

VI. Carefully stack each layer on the thumb tack from smallest grains on the bottom to largest grains on the top.

a. The base layer can be placed directly onto the pin head with sticky tape.

b. (optional) Place a thin plastic round on top of each grain layer.

c. Stack the next layer, paper side down and grain side up.

d. Repeat with thin plastic rounds placed on top of each, including the top layer.

VII. Carefully wrap the "tower" of grains with parafilm to hold the layers tightly together.

a. It is important that the grains and layers are not able to move during the scan.

VIII. Label your mount and draw an orientation mark on your pin.

Figure A3.1: Push pin used to mount grains for CT scans. Black line marks the orientation of the scan. Double-sided sticky tape is attached to the top.

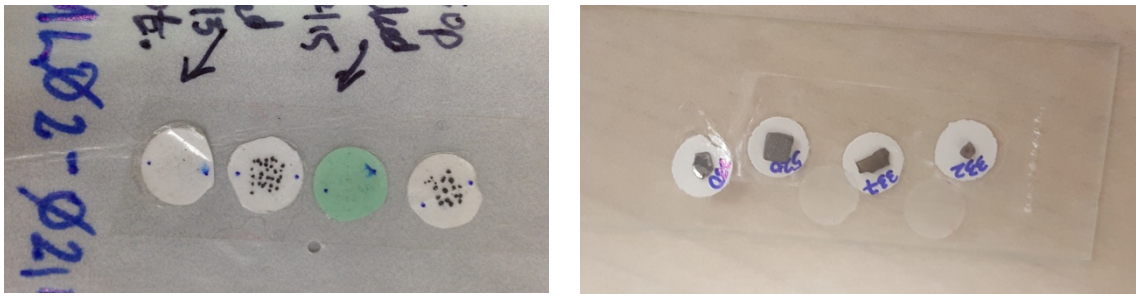

Figure A3.2: Paper rounds are placed onto microscope slide with double sided sticky tape on top. Place picked grains onto the tape, and center them on each paper round. If multiple samples are being combined you can write the name on the tape/paper.

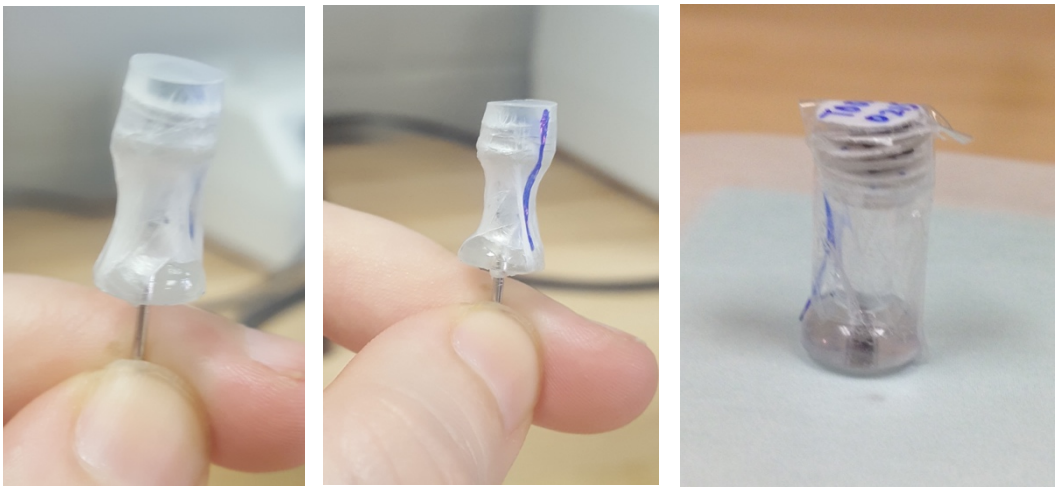

Figure A3.3: Cut out the paper with grains and stack 4-5 on top of each other on the pin. Wrap tightly together with parafilm or tape. Label the top or side and draw orientation mark.

References

Al-Khirbash, S., 2015, Genesis and mineralogical classification of Ni-laterites, Oman Mountains: Ore Geology Reviews, v. 65, p. 199-212.

Albarède, F., and Michard-Vitrac, A., 1978, Age and significance of the North Pyrenean metamorphism: Earth and planetary science letters, v. 40, no. 3, p. 327-332.

Ault, A. K., Reiners, P. W., Evans, J. P., and Thomson, S. N., 2015, Linking hematite (U-Th)/He dating with the microtextural record of seismicity in the Wasatch fault damage zone, Utah, USA: Geology, v. 43, no. 9, p. 771-774.

Auzende, A.-L., Escartin, J., Walte, N. P., Guillot, S., Hirth, G., and Frost, D. J., 2015, Deformation mechanisms of antigorite serpentinite at subduction zone conditions determined from experimentally and naturally deformed rocks: Earth and Planetary Science Letters, v. 411, p. 229-240.

Bach, W., Garrido, C. J., Paulick, H., Harvey, J., and Rosner, M., 2004, Seawater-peridotite interactions: First insights from ODP Leg 209, MAR 15 N: Geochemistry, Geophysics, Geosystems, v. 5, no. 9.

Bach, W., Paulick, H., Garrido, C. J., Ildefonse, B., Meurer, W. P., and Humphris, S. E., 2006, Unraveling the sequence of serpentinization reactions: petrography, mineral chemistry, and petrophysics of serpentinites from MAR 15 N (ODP Leg 209, Site 1274): Geophysical research letters, v. 33, no. 13.

Bedini, R., and Bodinier, J.-L., 1999, Distribution of incompatible trace elements between the constituents of spinel peridotite xenoliths: ICP-MS data from the East African Rift: Geochimica et Cosmochimica Acta, v. 63, no. 22, p. 3883-3900.

Bernet, M., 2009, A field-based estimate of the zircon fission-track closure temperature: Chemical Geology, v. 259, no. 3, p. 181-189.

Bill, M., O'Dogherty, L., Guex, J., Baumgartner, P. O., and Masson, H., 2001, Radiolarite ages in Alpine-Mediterranean ophiolites: Constraints on the oceanic spreading and the Tethys-Atlantic connection: Geological Society of America Bulletin, v. 113, no. 1, p. 129-143.

Bissig, T., and Hermann, J., 1999, From pre-Alpine extension to Alpine convergence: the example of the southwestern margin of the Margna nappe (Val Malenco, N-Italy): Schweizerische Mineralogische und Petrographische Mitteilungen, v. 79, no. 3, p. 363-380.

Blackburn, T. J., Stockli, D. F., and Walker, J. D., 2007, Magnetite (U–Th)/He dating and its application to the geochronology of intermediate to mafic volcanic rocks: Earth and Planetary Science Letters, v. 259, no. 3, p. 360-371.

Bodinier, J., Vasseur, G., Vernieres, J., Dupuy, C., and Fabries, J., 1990, Mechanisms of mantle metasomatism: geochemical evidence from the Lherz orogenic peridotite: Journal of Petrology, v. 31, no. 3, p. 597-628.

Bodinier, J.-I., Merlet, C., Bedini, R., Simien, F., Remaidi, M., and Garrido, C., 1996, Distribution of niobium, tantalum, and other highly incompatible trace elements in

the lithospheric mantle: the spinel paradox: Geochimica et Cosmochimica Acta, v. 60, no. 3, p. 545-550.

Boudier, F., and Coleman, R., 1981, Cross section through the peridotite in the Samail ophiolite, southeastern Oman Mountains: Journal of Geophysical Research: Solid Earth, v. 86, no. B4, p. 2573-2592.

Boudier, F., and Nicolas, A., 1995, Nature of the Moho transition zone in the Oman ophiolite: Journal of Petrology, v. 36, no. 3, p. 777-796.

Braun, M. G., and Kelemen, P. B., 2002, Dunite distribution in the Oman ophiolite: Implications for melt flux through porous dunite conduits: Geochemistry, Geophysics, Geosystems, v. 3, no. 11, p. 1-21.

Breeding, C. M., Ague, J. J., and Bröcker, M., 2004, Fluid–metasedimentary rock interactions in subduction-zone mélange: implications for the chemical composition of arc magmas: Geology, v. 32, no. 12, p. 1041-1044.

Bröcker, M., Baldwin, S., and Arkudas, R., 2013, The geological significance of 40Ar/39Ar and Rb–Sr white mica ages from Syros and Sifnos, Greece: a record of continuous (re) crystallization during exhumation?: Journal of Metamorphic Geology, v. 31, no. 6, p. 629-646.

Bröcker, M., and Enders, M., 2001, Unusual bulk-rock compositions in eclogite-facies rocks from Syros and Tinos (Cyclades, Greece): implications for U–Pb zircon geochronology: Chemical Geology, v. 175, no. 3, p. 581-603.

Burkhard, D. J., 1993, Accessory chromium spinels: their coexistence and alteration in serpentinites: Geochimica et Cosmochimica Acta, v. 57, no. 6, p. 1297-1306.

Burkhard, D. J., and O'Neil, J. R., 1988, Contrasting serpentinization processes in the eastern Central Alps: Contributions to Mineralogy and Petrology, v. 99, no. 4, p. 498-506.

Callen, R., Wasson, R., and Gillespie, R., 1983, Reliability of radiocarbon dating of pedogenic carbonate in the Australian arid zone: Sedimentary Geology, v. 35, no. 1, p. 1-14.

Clerc, C., and Lagabrielle, Y., 2014, Thermal control on the modes of crustal thinning leading to mantle exhumation: Insights from the Cretaceous Pyrenean hot paleomargins: Tectonics, v. 33, no. 7, p. 1340-1359.

Clerc, C., Lagabrielle, Y., Neumaier, M., Reynaud, J.-Y., and de Saint Blanquat, M., 2012, Exhumation of subcontinental mantle rocks: evidence from ultramafic-bearing clastic deposits nearby the Lherz peridotite body, French Pyrenees: Bulletin de la Société géologique de France, v. 183, no. 5, p. 443-459.

Clerc, C., Lahfid, A., Monié, P., Lagabrielle, Y., Chopin, C., Poujol, M., Boulvais, P., Ringenbach, J., Masini, E., and de St Blanquat, M., 2015, High-temperature metamorphism during extreme thinning of the continental crust: a reappraisal of the North Pyrenean passive paleomargin: Solid Earth, v. 6, no. 2, p. 643.

Coleman, R. G., 1971, Petrologic and geophysical nature of serpentinites: Geological Society of America Bulletin, v. 82, no. 4, p. 897-918.

Coogan, L., Jenkin, G., and Wilson, R., 2007, Contrasting cooling rates in the lower oceanic crust at fast-and slow-spreading ridges revealed by geospeedometry: Journal of Petrology, v. 48, no. 11, p. 2211-2231.

Cooperdock, E. H., and Stockli, D. F., 2016a, Unraveling alteration histories in serpentinites and associated ultramafic rocks with magnetite (U-Th)/He geochronology: Geology, v. 44, no. 11, p. 967-970.

-, 2016b, Unraveling alteration histories in serpentinites and associated ultramafic rocks with magnetite (U-Th)/He geochronology: Geology, p. G38587. 38581.

Debret, B., Andreani, M., Godard, M., Nicollet, C., Schwartz, S., and Lafay, R., 2013, Trace element behavior during serpentinization/de-serpentinization of an eclogitized oceanic lithosphere: A LA-ICPMS study of the Lanzo ultramafic massif (Western Alps): Chemical Geology, v. 357, p. 117-133.

Desmurs, L., Müntener, O., and Manatschal, G., 2002, Onset of magmatic accretion within a magma-poor rifted margin: a case study from the Platta ocean-continent transition, eastern Switzerland: Contributions to Mineralogy and Petrology, v. 144, no. 3, p. 365-382.

Dick, H. J., Fisher, R. L., and Bryan, W. B., 1984, Mineralogic variability of the uppermost mantle along mid-ocean ridges: Earth and Planetary Science Letters, v. 69, no. 1, p. 88-106.

Djimbi, D. M., Gautheron, C., Roques, J., Tassan-Got, L., Gerin, C., and Simoni, E., 2015, Impact of apatite chemical composition on (U-Th)/He thermochronometry: An atomistic point of view: Geochimica et Cosmochimica Acta, v. 167, p. 162-176.

Dorale, J. A., Edwards, R. L., Alexander Jr, E. C., Shen, C.-C., Richards, D. A., and Cheng, H., 2004, Uranium-series dating of speleothems: current techniques, limits, & applications, Studies of Cave Sediments, Springer, p. 177-197.

Dubińska, E., Bylina, P., Kozłowski, A., Dörr, W., Nejbert, K., Schastok, J., and Kulicki, C., 2004, U–Pb dating of serpentinization: hydrothermal zircon from a metasomatic rodingite shell (Sudetic ophiolite, SW Poland): Chemical Geology, v. 203, no. 3, p. 183-203.

Edwards, R., Gallup, C., and Cheng, H., 2003, Uranium-series dating of marine and lacustrine carbonates: Reviews in Mineralogy and Geochemistry, v. 52, no. 1, p. 363-405.

Evans, B. W., 1977, Metamorphism of alpine peridotite and serpentinite: Annual Review of Earth and Planetary Sciences, v. 5, no. 1, p. 397-447.

-, 2004, The serpentinite multisystem revisited: chrysotile is metastable: International Geology Review, v. 46, no. 6, p. 479-506.

-, 2008, Control of the products of serpentinization by the Fe2+ Mg− 1 exchange potential of olivine and orthopyroxene: Journal of Petrology, v. 49, no. 10, p. 1873-1887.

-, 2010, Lizardite versus antigorite serpentinite: Magnetite, hydrogen, and life (?): Geology, v. 38, no. 10, p. 879-882.

Evans, B. W., and Frost, B. R., 1975, Chrome-spinel in progressive metamorphism—a preliminary analysis: Geochimica et Cosmochimica Acta, v. 39, no. 6, p. 959-972.

Evans, S. L., 2011, Timing of exhumation of the eastern Central Alps from zircon and apatite (U-Th)/He thermochronology (Graubünden, Switzerland): University of Kansas.

Fabriès, J., 1979, Spinel-olivine geothermometry in peridotites from ultramafic complexes: Contributions to Mineralogy and Petrology, v. 69, no. 4, p. 329-336.

Falk, E. S., and Kelemen, P. B., 2015, Geochemistry and petrology of listvenite in the Samail ophiolite, Sultanate of Oman: Complete carbonation of peridotite during ophiolite emplacement: Geochimica et Cosmochimica Acta, v. 160, p. 70-90.

Fanale, F., and Kulp, J. L., 1962, The helium method and the age of the Cornwall, Pennsylvania magnetite ore: Economic Geology, v. 57, no. 5, p. 735-746.

Farley, K., and Flowers, R., 2012, (U–Th)/Ne and multidomain (U–Th)/He systematics of a hydrothermal hematite from eastern Grand Canyon: Earth and Planetary Science Letters, v. 359, p. 131-140.

Farley, K., Wolf, R., and Silver, L., 1996, The effects of long alpha-stopping distances on (U Th)/He ages: Geochimica et cosmochimica acta, v. 60, no. 21, p. 4223-4229.

Farley, K. A., 2002, (U-Th)/He dating: Techniques, calibrations, and applications: Reviews in Mineralogy and Geochemistry, v. 47, no. 1, p. 819-844.

Froitzheim, N., and Manatschal, G., 1996, Kinematics of Jurassic rifting, mantle exhumation, and passive-margin formation in the Austroalpine and Penninic nappes (eastern Switzerland): Geological Society of America Bulletin, v. 108, no. 9, p. 1120-1133.

Froitzheim, N., and Rubatto, D., 1998, Continental breakup by detachment faulting: field evidence and geochronological constraints (Tasna nappe, Switzerland): Terra Nova, v. 10, no. 4, p. 171-176.

Früh-Green, G. L., Weissert, H., and Bernoulli, D., 1990, A multiple fluid history recorded in Alpine ophiolites: Journal of the Geological Society, v. 147, no. 6, p. 959-970.

Fujiwara, T., Lin, J., Matsumoto, T., Kelemen, P. B., Tucholke, B. E., and Casey, J. F., 2003, Crustal Evolution of the Mid-Atlantic Ridge near the Fifteen-Twenty Fracture Zone in the last 5 Ma: Geochemistry, Geophysics, Geosystems, v. 4, no. 3.

Gautier, P., Brun, J.-P., Moriceau, R., Sokoutis, D., Martinod, J., and Jolivet, L., 1999, Timing, kinematics and cause of Aegean extension: a scenario based on a comparison with simple analogue experiments: Tectonophysics, v. 315, no. 1, p. 31-72.

Godard, M., Jousselin, D., and Bodinier, J.-L., 2000, Relationships between geochemistry and structure beneath a palaeo-spreading centre: a study of the mantle section in the Oman ophiolite: Earth and Planetary Science Letters, v. 180, no. 1, p. 133-148.

Grimes, C. B., Cheadle, M. J., John, B. E., Reiners, P. W., and Wooden, J. L., 2011, Cooling rates and the depth of detachment faulting at oceanic core complexes: Evidence from zircon Pb/U and (U-Th)/He ages: Geochemistry, Geophysics, Geosystems, v. 12, no. 3.

Gunnell, Y., Carter, A., Petit, C., and Fournier, M., 2007, Post-rift seaward downwarping at passive margins: new insights from southern Oman using stratigraphy to constrain apatite fission-track and (U-Th)/He dating: Geology, v. 35, no. 7, p. 647-650.

Hacker, B. R., 1994, Rapid emplacement of young oceanic lithosphere: argon geochronology of the Oman ophiolite: SCIENCE-NEW YORK THEN WASHINGTON-, p. 1563-1563.

Handy, M. R., Schmid, S. M., Bousquet, R., Kissling, E., and Bernoulli, D., 2010, Reconciling plate-tectonic reconstructions of Alpine Tethys with the geological–geophysical record of spreading and subduction in the Alps: Earth-Science Reviews, v. 102, no. 3, p. 121-158.

Hanghøj, K., Kelemen, P. B., Hassler, D., and Godard, M., 2010, Composition and genesis of depleted mantle peridotites from the Wadi Tayin Massif, Oman Ophiolite; major and trace element geochemistry, and Os isotope and PGE systematics: Journal of Petrology, v. 51, no. 1-2, p. 201-227.

Hanna, S. S., 1990, The Alpine deformation of the central Oman Mountains: Geological Society, London, Special Publications, v. 49, no. 1, p. 341-359.

Hansmann, W., Müntener, O., and Hermann, J., 2001, U-Pb zircon geochronology of a tholeiitic intrusion and associated migmatits at a continental crust-mantle transition, Val Malenco, Italy: Schweizerische Mineralogische und Petrographische Mitteilungen, v. 81, no. 2, p. 239-255.

Harrison, T. M., Duncan, I., and McDougall, I., 1985, Diffusion of 40Ar in biotite: temperature, pressure and compositional effects: Geochimica et Cosmochimica Acta, v. 49, no. 11, p. 2461-2468.

Hauri, E. H., Wagner, T. P., and Grove, T. L., 1994, Experimental and natural partitioning of Th, U, Pb and other trace elements between garnet, clinopyroxene and basaltic melts: Chemical Geology, v. 117, no. 1-4, p. 149-166.

Henry, P., Azambre, B., Montigny, R., Rossy, M., and Stevenson, R., 1998, Late mantle evolution of the Pyrenean sub-continental lithospheric mantle in the light of new

40 Ar–39 Ar and Sm–Nd ages on pyroxenites and peridotites (Pyrenees, France): Tectonophysics, v. 296, no. 1, p. 103-123.

Hermann, J., Müntener, O., Trommsdorff, V., Hansmann, W., and Piccardo, G. B., 1997, Fossil crust-to-mantle transition, Val Malenco (Italian Alps): Journal of Geophysical Research: Solid Earth, v. 102, no. B9, p. 20123-20132.

Jacobs, J., Thomas, R. J., Ksienzyk, A. K., and Dunkl, I., 2015, Tracking the Oman Ophiolite to the surface—New fission track and (U–Th)/He data from the Aswad and Khor Fakkan Blocks, United Arab Emirates: Tectonophysics, v. 644, p. 68-80.

Jagoutz, O., Müntener, O., Manatschal, G., Rubatto, D., Péron-Pinvidic, G., Turrin, B. D., and Villa, I. M., 2007, The rift-to-drift transition in the North Atlantic: A stuttering start of the MORB machine?: Geology, v. 35, no. 12, p. 1087-1090.

Jahn, B.-m., and Cuvellier, H., 1994, Pb Pb and U Pb geochronology of carbonate rocks: an assessment: Chemical Geology, v. 115, no. 1-2, p. 125-151.

Keiter, M., Ballhaus, C., and Tomaschek, F., 2011, A new geological map of the Island of Syros (Aegean Sea, Greece): implications for lithostratigraphy and structural history of the Cycladic Blueschist Unit: Geological Society of America Special Papers, v. 481, p. 1-43.

Keiter, M., Piepjohn, K., Ballhaus, C., Lagos, M., and Bode, M., 2004, Structural development of high-pressure metamorphic rocks on Syros island (Cyclades, Greece): Journal of Structural Geology, v. 26, no. 8, p. 1433-1445.

Kelemen, P., Kikawa, E., and Jay Miller, D., 2004, ODP Leg 209 drills into mantle peridotite along the Mid-Atlantic Ridge from 14 N to 16 N: JOIDES J, v. 30, p. 14-20.

Kelemen, P. B., and Matter, J., 2008, In situ carbonation of peridotite for CO2 storage: Proceedings of the National Academy of Sciences.

Kelemen, P. B., Shimizu, N., and Salters, V. J., 1995, Extraction of mid-ocean-ridge basalt from the upwelling mantle by focused flow of melt in dunite channels: Nature, v. 375, no. 6534, p. 747.

Kerrick, D., and Connolly, J., 1998, Subduction of ophicarbonates and recycling of CO2 and H2O: Geology, v. 26, no. 4, p. 375-378.

Ketcham, R. A., Gautheron, C., and Tassan-Got, L., 2011, Accounting for long alpha-particle stopping distances in (U–Th–Sm)/He geochronology: refinement of the baseline case: Geochimica et Cosmochimica Acta, v. 75, no. 24, p. 7779-7791.

Kodolányi, J., Pettke, T., Spandler, C., Kamber, B. S., and Gméling, K., 2011, Geochemistry of ocean floor and fore-arc serpentinites: constraints on the ultramafic input to subduction zones: Journal of Petrology, p. egr058.

Lackner, K. S., Wendt, C. H., Butt, D. P., Joyce, E. L., and Sharp, D. H., 1995, Carbon dioxide disposal in carbonate minerals: Energy, v. 20, no. 11, p. 1153-1170.

Lagabrielle, Y., and Bodinier, J. L., 2008, Submarine reworking of exhumed subcontinental mantle rocks: field evidence from the Lherz peridotites, French Pyrenees: Terra Nova, v. 20, no. 1, p. 11-21.

Lagabrielle, Y., Labaume, P., and de Saint Blanquat, M., 2010, Mantle exhumation, crustal denudation, and gravity tectonics during Cretaceous rifting in the Pyrenean realm (SW Europe): Insights from the geological setting of the lherzolite bodies: Tectonics, v. 29, no. 4.

Lagos, M., Scherer, E. E., Tomaschek, F., Münker, C., Keiter, M., Berndt, J., and Ballhaus, C., 2007, High precision Lu–Hf geochronology of Eocene eclogite-facies rocks from Syros, Cyclades, Greece: Chemical Geology, v. 243, no. 1, p. 16-35.

Laughlin, A., Aldrich, M., Shafiqullah, M., and Husler, J., 1986, Tectonic implications of the age, composition, and orientation of lamprophyre dikes, Navajo volcanic field, Arizona: Earth and Planetary Science Letters, v. 76, no. 3-4, p. 361-374.

Le Roux, V., Bodinier, J.-L., Tommasi, A., Alard, O., Dautria, J.-M., Vauchez, A., and Riches, A., 2007, The Lherz spinel lherzolite: refertilized rather than pristine mantle: Earth and Planetary Science Letters, v. 259, no. 3, p. 599-612.

Maheo, G., Gautheron, C., Leloup, P. H., Fox, M., Tassant-Got, L., and Douville, E., 2013, Neogene exhumation history of the Bergell massif (southeast Central Alps): Terra Nova, v. 25, no. 2, p. 110-118.

Maluski, H., Bonneau, M., and Kienast, J.-R., 1987, Dating the metamorphic events in the Cycladic area: 39Ar/40Ar data from metamorphic rocks of the island of Syros (Greece): Bulletin de la Société géologique de France, v. 8, p. 833-842.

Manatschal, G., and Müntener, O., 2009, A type sequence across an ancient magma-poor ocean–continent transition: the example of the western Alpine Tethys ophiolites: Tectonophysics, v. 473, no. 1, p. 4-19.

Manatschal, G., Müntener, O., Lavier, L., Minshull, T., and Péron-Pinvidic, G., 2007, Observations from the Alpine Tethys and Iberia–Newfoundland margins pertinent to the interpretation of continental breakup: Geological Society, London, Special Publications, v. 282, no. 1, p. 291-324.

Mann, A., and Hanna, S., 1990, The tectonic evolution of pre-Permian rocks, Central and Southeastern Oman Mountains: Geological Society, London, Special Publications, v. 49, no. 1, p. 307-325.

Marschall, H. R., Altherr, R., Gméling, K., and Kasztovszky, Z., 2009, Lithium, boron and chlorine as tracers for metasomatism in high-pressure metamorphic rocks: a case study from Syros (Greece): Mineralogy and Petrology, v. 95, no. 3-4, p. 291-302.

Marschall, H. R., Ludwig, T., Altherr, R., Kalt, A., and Tonarini, S., 2006, Syros metasomatic tourmaline: evidence for very high-δ11B fluids in subduction zones: Journal of Petrology, v. 47, no. 10, p. 1915-1942.

McCollom, T. M., and Seewald, J. S., 2013, Serpentinites, hydrogen, and life: Elements, v. 9, no. 2, p. 129-134.

McQuarrie, N., and van Hinsbergen, D. J., 2013, Retrodeforming the Arabia-Eurasia collision zone: Age of collision versus magnitude of continental subduction: Geology, v. 41, no. 3, p. 315-318.

Mellini, M., Trommsdorff, V., and Compagnoni, R., 1987, Antigorite polysomatism: behaviour during progressive metamorphism: Contributions to Mineralogy and Petrology, v. 97, no. 2, p. 147-155.

Mervine, E. M., Humphris, S. E., Sims, K. W., Kelemen, P. B., and Jenkins, W. J., 2014, Carbonation rates of peridotite in the Samail Ophiolite, Sultanate of Oman, constrained through 14 C dating and stable isotopes: Geochimica et Cosmochimica Acta, v. 126, p. 371-397.

Mével, C., 2003, Serpentinization of abyssal peridotites at mid-ocean ridges: Comptes Rendus Geoscience, v. 335, no. 10, p. 825-852.

Miller, D. P., Marschall, H. R., and Schumacher, J. C., 2009, Metasomatic formation and petrology of blueschist-facies hybrid rocks from Syros (Greece): Implications for reactions at the slab–mantle interface: Lithos, v. 107, no. 1, p. 53-67.

Miller, H. M., Matter, J. M., Kelemen, P., Ellison, E. T., Conrad, M. E., Fierer, N., Ruchala, T., Tominaga, M., and Templeton, A. S., 2016, Modern water/rock reactions in Oman hyperalkaline peridotite aquifers and implications for microbial habitability: Geochimica et Cosmochimica Acta, v. 179, p. 217-241.

Min, K., Reiners, P. W., Wolff, J. A., Mundil, R., and Winters, R. L., 2006, (U–Th)/He dating of volcanic phenocrysts with high-U–Th inclusions, Jemez volcanic field, New Mexico: Chemical geology, v. 227, no. 3, p. 223-235.

Montigny, R., Azambre, B., Rossy, M., and Thuizat, R., 1986, K-Ar study of cretaceous magmatism and metamorphism in the pyrenees: Age and length of rotation of the Iiberian Peninsula: Tectonophysics, v. 129, no. 1-4, p. 257-273.

Mouthereau, F., Filleaudeau, P. Y., Vacherat, A., Pik, R., Lacombe, O., Fellin, M. G., Castelltort, S., Christophoul, F., and Masini, E., 2014, Placing limits to shortening

evolution in the Pyrenees: Role of margin architecture and implications for the Iberia/Europe convergence: Tectonics, v. 33, no. 12, p. 2283-2314.

Müntener, O., Hermann, J., and Trommsdorff, V., 2000, Cooling history and exhumation of lower-crustal granulite and upper mantle (Malenco, Eastern Central Alps): Journal of Petrology, v. 41, no. 2, p. 175-200.

Müntener, O., Manatschal, G., Desmurs, L., and Pettke, T., 2010, Plagioclase peridotites in ocean–continent transitions: refertilized mantle domains generated by melt stagnation in the shallow mantle lithosphere: Journal of Petrology, v. 51, no. 1-2, p. 255-294.

Nadoll, P., Angerer, T., Mauk, J. L., French, D., and Walshe, J., 2014, The chemistry of hydrothermal magnetite: a review: Ore Geology Reviews, v. 61, p. 1-32.

Naeser, C., 1971, Geochronology of the Navajo-Hopi Diatremes, Four Corners Area: Journal of Geophysical Research, v. 76, no. 20, p. 4978-4985.

Nasir, S., Al Sayigh, A. R., Al Harthy, A., Al-Khirbash, S., Al-Jaaidi, O., Musllam, A., Al-Mishwat, A., and Al-Bu'saidi, S., 2007, Mineralogical and geochemical characterization of listwaenite from the Semail Ophiolite, Oman: Chemie der Erde-Geochemistry, v. 67, no. 3, p. 213-228.

Neal, C., and Stanger, G., 1984, Calcium and magnesium hydroxide precipitation from alkaline groundwaters in Oman, and their significance to the process of serpentinization: Mineral. Mag, v. 48, no. 347, p. 237-241.

Nolan, S., Skelton, P., Clissold, B., and Smewing, J., 1990, Maastrichtian to early Tertiary stratigraphy and palaeogeography of the central and northern Oman Mountains: Geological Society, London, Special Publications, v. 49, no. 1, p. 495-519.

O'Neil, J. R., and Barnes, I., 1971, C 13 and O 18 compositions in some fresh-water carbonates associated with ultramafic rocks and serpentinites: western United States: Geochimica et Cosmochimica Acta, v. 35, no. 7, p. 687-697.

Oberli, F., Meier, M., Berger, A., Rosenberg, C. L., and GierÉ, R., 2004, U-Th-Pb and 230 Th/238 U disequilibrium isotope systematics: Precise accessory mineral chronology and melt evolution tracing in the Alpine Bergell intrusion: Geochimica et cosmochimica Acta, v. 68, no. 11, p. 2543-2560.

Okrusch, M., and Bröcker, M., 1990, Eclogites associated with high-grade blueschists in the Cyclades archipelago, Greece: a review: European Journal of Mineralogy, p. 451-478.

Oufi, O., Cannat, M., and Horen, H., 2002, Magnetic properties of variably serpentinized abyssal peridotites: Journal of Geophysical Research: Solid Earth, v. 107, no. B5.

Paukert, A. N., Matter, J. M., Kelemen, P. B., Shock, E. L., and Havig, J. R., 2012, Reaction path modeling of enhanced in situ CO 2 mineralization for carbon sequestration in the peridotite of the Samail Ophiolite, Sultanate of Oman: Chemical geology, v. 330, p. 86-100.

Peretti, A., and Köppel, V., 1986, Geochemical and lead isotope evidence for a mid-ocean ridge type mineralization within a polymetamorphic ophiolite complex (Monte del

Forno, North Italy/Switzerland): Earth and planetary science letters, v. 80, no. 3-4, p. 252-264.

Pinto, V. H. G., Manatschal, G., Karpoff, A. M., and Viana, A., 2015, Tracing mantle-reacted fluids in magma-poor rifted margins: The example of Alpine Tethyan rifted margins: Geochemistry, Geophysics, Geosystems, v. 16, no. 9, p. 3271-3308.

Power, I. M., Wilson, S. A., and Dipple, G. M., 2013, Serpentinite Carbonation for CO₂ Sequestration: Elements, v. 9, no. 2, p. 115-121.

Pozzorini, D., 1996, Stable isotope investigations of ophicarbonate rocks, Bergell Aureole, Valmalenco: Constraints on fluid-rock interaction.

Putlitz, B., Matthews, A., and Valley, J. W., 2000, Oxygen and hydrogen isotope study of high-pressure metagabbros and metabasalts (Cyclades, Greece): implications for the subduction of oceanic crust: Contributions to Mineralogy and Petrology, v. 138, no. 2, p. 114-126.

Python, M., and Ceuleneer, G., 2003, Nature and distribution of dykes and related melt migration structures in the mantle section of the Oman ophiolite: Geochemistry, Geophysics, Geosystems, v. 4, no. 7.

Reiners, P. W., 2005, Zircon (U-Th)/He thermochronometry: Reviews in Mineralogy and Geochemistry, v. 58, no. 1, p. 151-179.

Reiners, P. W., Brady, R., Farley, K. A., Fryxell, J. E., Wernicke, B., and Lux, D., 2000, Helium and argon thermochronometry of the Gold Butte block, south Virgin Mountains, Nevada: Earth and Planetary Science Letters, v. 178, no. 3, p. 315-326.

Reiners, P. W., and Brandon, M. T., 2006, Using thermochronology to understand orogenic erosion: Annu. Rev. Earth Planet. Sci., v. 34, p. 419-466.

Reiners, P. W., and Farley, K. A., 2001, Influence of crystal size on apatite (U–Th)/He thermochronology: an example from the Bighorn Mountains, Wyoming: Earth and Planetary Science Letters, v. 188, no. 3, p. 413-420.

Reiners, P. W., Farley, K. A., and Hickes, H. J., 2002, He diffusion and (U–Th)/He thermochronometry of zircon: initial results from Fish Canyon Tuff and Gold Butte: Tectonophysics, v. 349, no. 1, p. 297-308.

Ridley, J., 1984, The significance of deformation associated with blueschist facies metamorphism on the Aegean island of Syros: Geological Society, London, Special Publications, v. 17, no. 1, p. 545-550.

Ring, U., Thomson, S. N., and Bröcker, M., 2003, Fast extension but little exhumation: the Vari detachment in the Cyclades, Greece: Geological Magazine, v. 140, no. 03, p. 245-252.

Robertson, A., Searle, M., and Ries, A., 1990, The geology and tectonics of the Oman region: Geological Society of London special publication, v. 49, p. 845.

Roden, M. F., Smith, D., and McDowell, F. W., 1979, Age and extent of potassic volcanism on the Colorado Plateau: Earth and Planetary Science Letters, v. 43, no. 2, p. 279-284.

Saddiqi, O., Michard, A., Goffe, B., Poupeau, G., and Oberhänsli, R., 2006, Fission-track thermochronology of the Oman Mountains continental windows, and current

problems of tectonic interpretation: Bulletin de la Société Géologique de France, v. 177, no. 3, p. 127-134.

Scambelluri, M., Bebout, G. E., Belmonte, D., Gilio, M., Campomenosi, N., Collins, N., and Crispini, L., 2016, Carbonation of subduction-zone serpentinite (high-pressure ophicarbonate; Ligurian Western Alps) and implications for the deep carbon cycling: Earth and Planetary Science Letters, v. 441, p. 155-166.

Scambelluri, M., Pettke, T., Rampone, E., Godard, M., and Reusser, E., 2014, Petrology and trace element budgets of high-pressure peridotites indicate subduction dehydration of serpentinized mantle (Cima di Gagnone, Central Alps, Switzerland): Journal of petrology, p. egt068.

Schaltegger, U., Desmurs, L., Manatschal, G., Müntener, O., Meier, M., Frank, M., and Bernoulli, D., 2002, The transition from rifting to sea-floor spreading within a magma-poor rifted margin: field and isotopic constraints: Terra Nova, v. 14, no. 3, p. 156-162.

Schmid, S., and Froitzheim, N., 1993, Oblique slip and block rotation along the Engadine line: Eclogae Geologicae Helvetiae, v. 86, no. 2, p. 569-593.

Schroeder, T., John, B., and Frost, B. R., 2002, Geologic implications of seawater circulation through peridotite exposed at slow-spreading mid-ocean ridges: Geology, v. 30, no. 4, p. 367-370.

Schuiling, R., and De Boer, P., 2011, Rolling stones; fast weathering of olivine in shallow seas for cost-effective CO 2 capture and mitigation of global warming and ocean acidification: Earth System Dynamics Discussions, v. 2, no. 2, p. 551-568.

Schwarzenbach, E. M., Caddick, M. J., Beard, J. S., and Bodnar, R. J., 2016, Serpentinization, element transfer, and the progressive development of zoning in veins: evidence from a partially serpentinized harzburgite: Contributions to Mineralogy and Petrology, v. 171, no. 1, p. 1-22.

Searle, M., and Cox, J., 1999, Tectonic setting, origin, and obduction of the Oman ophiolite: Geological Society of America Bulletin, v. 111, no. 1, p. 104-122.

SEARLE, M. P., and COX, J., 2002, Subduction zone metamorphism during formation and emplacement of the Semail ophiolite in the Oman Mountains: Geological Magazine, v. 139, no. 03, p. 241-255.

Seck, H. A., Kötz, J., Okrusch, M., Seidel, E., and Stosch, H.-G., 1996, Geochemistry of a meta-ophiolite suite: an association of metagabbros, eclogites and glaucophanites on the island of Syros, Greece: European Journal of Mineralogy, p. 607-624.

Seitz, M., and Hart, S., 1973, Uranium and boron distributions in some oceanic ultramafic rocks: Earth and Planetary Science Letters, v. 21, no. 1, p. 97-107.

Shuster, D. L., Vasconcelos, P. M., Heim, J. A., and Farley, K. A., 2005, Weathering geochronology by (U-Th)/He dating of goethite: Geochimica et Cosmochimica Acta, v. 69, no. 3, p. 659-673.

Skelton, A. D., and Valley, J. W., 2000, The relative timing of serpentinisation and mantle exhumation at the ocean–continent transition, Iberia: constraints from oxygen isotopes: Earth and Planetary Science Letters, v. 178, no. 3, p. 327-338.

Skelton, P., Nolan, S., and Scott, R., 1990, The Maastrichtian transgression onto the northwestern flank of the Proto-Oman Mountains: sequences of rudist-bearing

beach to open shelf facies: Geological Society, London, Special Publications, v. 49, no. 1, p. 521-547.

Sleep, N. H., Bird, D. K., and Pope, E. C., 2011, Serpentinite and the dawn of life: Philosophical Transactions of the Royal Society B: Biological Sciences, v. 366, no. 1580, p. 2857-2869.

Smith, D., and Levy, S., 1976, Petrology of the Green Knobs diatreme and implications for the upper mantle below the Colorado Plateau: Earth and Planetary Science Letters, v. 29, no. 1, p. 107-125.

Smith, P., Farquhar, R., and Hancock, R., 1991, Direct radiometric age determination of carbonate diagenesis using U-Pb in secondary calcite: Earth and Planetary science letters, v. 105, no. 4, p. 474-491.

Soukis, K., and Stockli, D. F., 2013, Structural and thermochronometric evidence for multi-stage exhumation of southern Syros, Cycladic islands, Greece: Tectonophysics, v. 595, p. 148-164.

Spotila, J. A., 2005, Applications of low-temperature thermochronometry to quantification of recent exhumation in mountain belts: Reviews in mineralogy and geochemistry, v. 58, no. 1, p. 449-466.

Stanger, G., 1985, Silicified serpentinite in the Semail nappe of Oman: Lithos, v. 18, p. 13-22.

Staudigel, H., and Hart, S. R., 1983, Alteration of basaltic glass: Mechanisms and significance for the oceanic crust-seawater budget: Geochimica et Cosmochimica Acta, v. 47, no. 3, p. 337-350.

Stockli, D. F., 2005, Application of low-temperature thermochronometry to extensional tectonic settings: Reviews in Mineralogy and Geochemistry, v. 58, no. 1, p. 411-448.

Stockli, D. F., Farley, K. A., and Dumitru, T. A., 2000, Calibration of the apatite (U-Th)/He thermochronometer on an exhumed fault block, White Mountains, California: Geology, v. 28, no. 11, p. 983-986.

Streit, E., Kelemen, P., and Eiler, J., 2012, Coexisting serpentine and quartz from carbonate-bearing serpentinized peridotite in the Samail Ophiolite, Oman: Contributions to Mineralogy and Petrology, v. 164, no. 5, p. 821-837.

Taylor, J. L., 2012, Practical guide to improved magnetite (U-Th)/He geochronometry - A case study from the Columbia River Basalt Group: University of Kansas.

Toft, P. B., Arkani-Hamed, J., and Haggerty, S. E., 1990, The effects of serpentinization on density and magnetic susceptibility: a petrophysical model: Physics of the Earth and Planetary Interiors, v. 65, no. 1-2, p. 137-157.

Tomaschek, F., Kennedy, A. K., Villa, I. M., Lagos, M., and Ballhaus, C., 2003, Zircons from Syros, Cyclades, Greece—recrystallization and mobilization of zircon during high-pressure metamorphism: Journal of Petrology, v. 44, no. 11, p. 1977-2002.

Trommsdorff, V., and Connolly, J. A., 1996, The ultramafic contact aureole about the Bregaglia (Bergell) tonalite: isograds and a thermal model: Schweizerische Mineralogische und Petrographische Mitteilungen, v. 76, p. 537-547.

Trommsdorff, V., and Evans, B. W., 1972, Progressive metamorphism of antigorite schist in the Bergell tonalite aureole (Italy): American Journal of Science, v. 272, no. 5, p. 423-437.

-, 1977, Antigorite-ophicarbonates: contact metamorphism in Valmalenco, Italy: Contributions to Mineralogy and Petrology, v. 62, no. 3, p. 301-312.

-, 1980, Titanian hydroxyl-clinohumite: formation and breakdown in antigorite rocks (Malenco, Italy): Contributions to Mineralogy and Petrology, v. 72, no. 3, p. 229-242.

Trommsdorff, V., Piccardo, G., and Montrasio, A., 1993, From magmatism through metamorphism to sea floor emplacement of subcontinental Adria lithosphere during pre-Alpine rifting (Malenco, Italy): Schweizerische Mineralogische und Petrographische Mitteilungen, v. 73, no. 2, p. 191-203.

Vacherat, A., Mouthereau, F., Pik, R., Bernet, M., Gautheron, C., Masini, E., Le Pourhiet, L., Tibari, B., and Lahfid, A., 2014, Thermal imprint of rift-related processes in orogens as recorded in the Pyrenees: Earth and Planetary Science Letters, v. 408, p. 296-306.

Vielzeuf, D., and Kornprobst, J., 1984, Crustal splitting and the emplacement of Pyrenean lherzolites and granulites: Earth and Planetary Science Letters, v. 67, no. 1, p. 87-96.

Villa, I. M., Hermann, J., Müntener, O., and Trommsdorff, V., 2000, 39Ar− 40Ar dating of multiply zoned amphibole generations (Malenco, Italian Alps): Contributions to Mineralogy and Petrology, v. 140, no. 3, p. 363-381.

von Blackenburg, F., 1992, Combined high-precision chronometry and geochemical tracing using accessory minerals: applied to the Central-Alpine Bergell intrusion (central Europe): Chemical Geology, v. 100, no. 1, p. 19-40.

von Strandmann, P. A. P., Dohmen, R., Marschall, H. R., Schumacher, J. C., and Elliott, T., 2015, Extreme magnesium isotope fractionation at outcrop scale records the mechanism and rate at which reaction fronts advance: Journal of Petrology, v. 56, no. 1, p. 33-58.

Wagner, G. A., Miller, D. S., and Jäger, E., 1979, Fission track ages on apatite of Bergell rocks from central Alps and Bergell boulders in Oligocene sediments: Earth and Planetary Science Letters, v. 45, no. 2, p. 355-360.

Workman, R. K., and Hart, S. R., 2005, Major and trace element composition of the depleted MORB mantle (DMM): Earth and Planetary Science Letters, v. 231, no. 1, p. 53-72.

Yelland, A., 1991, Thermo-tectonics of the Pyrenees and Provence from fission track studies: Unpublished PhD, thesis, Birkbeck College, University of London.

Zaun, P., and Wagner, G., 1985, Fission-track stability in zircons under geological conditions: Nuclear Tracks and Radiation Measurements (1982), v. 10, no. 3, p. 303-307.

Zeitler, P., Herczeg, A., McDougall, I., and Honda, M., 1987, U-Th-He dating of apatite: A potential thermochronometer: Geochimica et Cosmochimica Acta, v. 51, no. 10, p. 2865-2868.